Growth of graphene/hexagonal boron nitride heterostructures using molecular beam epitaxy

D I S S E R T A T I O N

zur Erlangung des akademischen Grades

Dr. rer. nat.
im Fach Physik

eingereicht an der
Mathematisch-Naturwissenschaftlichen Fakultät
Humboldt-Universität zu Berlin

von
M.Sc. Siamak Nakhaie

Präsidentin der Humboldt-Universität zu Berlin:
Prof. Dr.-Ing. Dr. Sabine Kunst

Dekan der Mathematisch-Naturwissenschaftlichen Fakultät:
Prof. Dr. Elmar Kulke

Gutachter:
(i) Prof. Dr. Henning Riechert
(ii) Prof. Dr. Ted W. Masselink
(iii) Prof. Dr. Sergei Novikov

eingereicht am: 09. November 2017
Tag der mündlichen Prüfung: 11. April 2018

Abstract

Two-dimensional (2D) materials offer a variety of novel properties and have shown great promise to be used in a wide range of applications. Recently, hexagonal boron nitride (h-BN) has attracted significant attention due to its suitability for integration into heterostructures with other 2D materials. In particular, van der Waals heterostructures combining h-BN and graphene offer many potential advantages, but remain difficult to produce as continuous films over large areas.

This thesis presents an investigation regarding the growth of h-BN and vertical heterostructures of graphene and h-BN on Ni substrates using molecular beam epitaxy (MBE). Various techniques such as Raman spectroscopy, atomic force microscopy, scanning electron microscopy, and X-ray photoelectron spectroscopy were used to characterize the grown films and gain insight into their growth behavior.

The growth of h-BN from elemental sources of B and N was investigated initially by using Ni foils as the growth substrate. The presence of crystalline h-BN was confirmed using Raman spectroscopy. Growth parameters resulting in continuous and atomically thin h-BN films were obtained. The morphology of h-BN islands has been found to evolve upon increasing the growth temperature. These investigations were complemented by growth experiments in which Ni films, deposited on MgO(111) substrates, were used as growth template. It was found that h-BN films grown on these templates are compressively strained. Decreasing the growth temperature led to formation of a h-BN film with lower structural quality. Nucleation and growth behavior of h-BN were studied by systematically varying the growth temperature and time. Corresponding observations such as changes in preferred nucleation site, crystallite size, and coverage of h-BN were discussed.

Growth of h-BN/graphene vertical heterostructures (h-BN on graphene) over large areas was demonstrated by employing a novel MBE-based technique, which allows both h-BN and graphene to form in the favorable growth environment provided by Ni. In this technique, graphene forms at the interface of h-BN/Ni via the precipitation of C atoms previously dissolved in the thin Ni film. The experimental results show that h-BN film in the heterostructure is strain-free, consistent with it being decoupled from the Ni substrate due to the interfacial graphene growth, while the graphene's lattice is contracted, most likely due to the incorporation of N in its structure. No evidence for the formation of BCN alloy could be found. Additionally, the suitability of ultraviolet Raman spectroscopy for characterization of h-BN/graphene heterostructures was demonstrated.

Finally, growth of large-area graphene/h-BN heterostructures (graphene on h-BN) was demonstrated via the direct deposition of C on top of MBE-grown h-BN. The lateral continuity of the constituents was examined using Raman spectroscopy. Furthermore, the surface morphology of the heterostructures and the structural quality of the overlying graphene were investigated and discussed.

Keywords: hexagonal boron nitride, h-BN, graphene, heterostructures, synthesis, molecular beam epitaxy, MBE

Zusammenfassung

Zweidimensionale (2D) Materialien bieten eine Vielzahl von neuartigen Eigenschaften und sind aussichtsreich Kandidaten für ein breites Spektrum an Anwendungen. Da hexagonales Bornitrid (h-BN) für eine Integration in Heterostrukturen mit anderen 2D Materialien geeignet ist, erweckte dieses in letzter Zeit großes Interesse. Insbesondere van-der-Waals-Heterostrukturen, welche h-BN und Graphen verbinden, weisen viele potenzielle Vorteile auf, verbleiben in ihrer großflächigen Herstellung von kontinuierlichen Filmen allerdings problematisch.

Diese Dissertation stellt eine Untersuchung betreffend des Wachstums von h-BN und vertikalen Heterostrukturen von Graphen und h-BN auf Ni-Substraten durch Molekularstrahlepitaxie (MBE) vor. Unterschiedliche Techniken wie Raman-Spektroskopie, Rasterkraftmikroskopie, Rasterelektronenmikroskopie und Röntgenphotoelektronenspektroskopie wurden eingesetzt um die gewachsenen Schichten zu untersuchen und einen Einblick in deren Wachstumsverhalten zu erlangen.

Zuerst wurde das Wachstum von h-BN mittels elementarer B- und N-Quellen auf Ni-Folien als Wachstumssubstrat untersucht. Kristalline h-BN-Schichten konnten durch Ramanspektroskopie nachgewiesen werden. Wachstumsparameter für kontinuierliche und atomar dünne Schichten wurden erlangt und eine sich mit der Temperatur entwickelnde Morphologie der h-BN Inseln konnte festgestellt werden. Diese Untersuchungen wurde durch Wachstumsexperimente ergänzt, in welchen Ni-Schichten auf MgO(111)-Substraten als Wachstumssubstrat verwendet wurden. Eine kompressive Verspannung konnte in den h-BN-Schichten auf diesen Substraten ermittelt werden. Eine Verringerung der Wachstumstemperatur führte zur Bildung einer h-BN-Schicht mit reduzierter struktureller Güte. Das Keimbildungs- und Wachstumsverhalten von h-BN wurde mittels einer systemischen Veränderung der Wachstumstemperatur und -dauer untersucht. Die entsprechenden Beobachtungen wie der Änderungen der bevorzugten Keimbildungszentren, der Kristallgröße und der Bedeckung des h-BN wurden diskutiert.

Ein Wachstum von großflächigen vertikalen h-BN/Graphene-Heterostrukturen (h-BN auf Graphen) konnte mittels einem neuartigen, MBE-basierenden Verfahren demonstriert werden, welche es h-BN und Graphen jeweils erlaubt sich in der vorteilhaften Wachstumsumgebung, welche von Ni bereitgestellt wird, zu formen. In diesem Verfahren formt sich Graphen an der Schnittstelle von h-BN und Ni durch Präzipitation von zuvor in der Ni-Schicht eingebrachtem C-Atomen. Passend dazu, dass die h-BN-Schicht in der Heterostruktur durch die Zwischenschichtbildung von Graphen von dem Ni-Substrat entkoppelt ist, zeigen die experimentellen Ergebnisse das sie spannungfrei ist, während Graphens Kristallgitter verspannt ist, was am wahrscheinlichsten auf einen Einbau von N in die Struktur zurückzuführen ist. Kein Nachweis für die Bildung einer BCN-Legierung konnte gefunden werden. Zusätzlich konnte die Eignung von ultravioletter Raman-Spektroskopie zur Charakterisierung von h-BN/Graphen-Heterostrukuren nachgewiesen werden.

Schließlich konnte noch ein großflächiges Wachstum von Graphen/h-BN-Heterostrukturen (Graphen auf h-BN) durch das direkte abscheiden von C auf MBE-gewachsenen h-BN gezeigt werden. Die laterale Kontinuität der Bestandteile wurde mittels Raman-Spektroskopie untersucht. Des Weiteren wurde die Oberflächenmorphologie der Heterostruktur und die strukturelle Qualität des aufliegenden Graphens untersucht und diskutiert.

Stichwörter: Bornitrid, h-BN, Graphen, Heterostrukturen, Graphen-Bornitrid-Heterostrukturen, Synthese, Wachstum, Molekularstrahlepitaxie, MBE

Publications

Publications of parts of this work

S. Nakhaie, J. M. Wofford, T. Schumann, U. Jahn, M. Ramsteiner, M. Hanke, J. M. J. Lopes, and H. Riechert, *Synthesis of atomically thin hexagonal boron nitride films on nickel foils by molecular beam epitaxy*, Appl. Phys. Lett. **106**, 213108 (2015).

J. M. Wofford*, S. Nakhaie*, T. Krause, X. Liu, M. Ramsteiner, M. Hanke, H. Riechert, and J. M. J. Lopes, *A hybrid MBE-based growth method for large-area synthesis of stacked hexagonal boron nitride/graphene heterostructures*, Sci. Rep. **7**, 43644 (2017).
* equal contribution

Talks and conference presentations

S. Nakhaie, J. M. Wofford, U. Jahn, T. Krause, X. Liu, M. Ramsteiner, M. Hanke, J. M. J. Lopes, and H. Riechert, *Growth of h-BN and h-BN/graphene heterostructures using molecular beam epitaxy* (contributed talk), Compound Semiconductor Week 2017 (CSW2017), Berlin, Germany, May 2017.

S. Nakhaie, J. M. Wofford, T. Krause, X. Liu, M. Ramsteiner, M. Hanke, H. Riechert, and J. M. J. Lopes, *A hybrid MBE-based growth method for large-area synthesis of stacked hexagonal boron nitride/graphene heterostructures* (contributed talk), Frühjahrstagung der Deutschen Physikalischen Gesellschaft (DPG), Dresden, Germany, March 2017.

S. Nakhaie, J. M. Wofford, M. Ramsteiner, T. Krause, M. Hanke, H. Riechert, and J. M. J. Lopes, *Growth of large-area hexagonal boron nitride/graphene heterostructures on nickel films using molecular beam epitaxy* (contributed talk), Graphene Week, Warsaw, Poland, June 2016.

S. Nakhaie, J. M. Wofford, M. Ramsteiner, C. Pfüller, H. Riechert, and J. M. J. Lopes, *Growth of continuous hexagonal boron nitride on smooth Ni films* (poster presentation), Frühjahrstagung der Deutschen Physikalischen Gesellschaft (DPG), Regensburg, March 2016.

S. Nakhaie, J. M. Wofford, T. Schumann, U. Jahn, M. Ramsteiner, Thilo Krause, M. Hanke, J. M. J. Lopes, and H. Riechert, *Growth of atomically thin h-BN films by MBE* (seminar talk), Scientific Advisory Board Meeting of the Paul-Drude-Institut für Festkörperelektronik, Berlin, Germany, October 2015.

S. Nakhaie, J. M. Wofford, T. Schumann, U. Jahn, M. Ramsteiner, J. M. J. Lopes, and H. Riechert, *Synthesis of atomically thin hexagonal boron nitride films on nickel foils by MBE* (poster presentation), GraphIta, Bologna, Italy, September 2015.

S. Nakhaie, J. M. Wofford, T. Schumann, U. Jahn, J. M. J. Lopes, and H. Riechert, *Synthesis of atomically thin hexagonal boron nitride films on nickel foils by MBE* (contributed talk), Graphene Week, Manchester, UK, June 2015.

S. Nakhaie, J. M. Wofford, T. Schumann, U. Jahn, J. M. J. Lopes, and H. Riechert, *Synthesis of atomically thin hexagonal boron nitride films on nickel foils by MBE* (contributed talk), Frühjahrstagung der Deutschen Physikalischen Gesellschaft (DPG), Berlin, Germany, March 2015.

Other conference contributions

J. M. J. Lopes, S. Nakhaie, J. M. Wofford, G. V. Soares, H. Riechert, *MBE growth of atomically thin graphene and hexagonal boron nitride films* (invited talk), Deutscher MBE-Workshop 2016, Garching, Germany, October 2016.

J. M. J. Lopes, S. Nakhaie, J. M. Wofford, M. Ramsteiner, T. Krause, M. Hanke, and H. Riechert, *MBE growth of large-area hexagonal boron nitride/graphene heterostructures on Ni/MgO(111) substrates* (contributed talk), 19th International Conference on Molecular-Beam Epitaxy (MBE2016), Montpelier, France, September 2016.

S. Nakhaie, J. M. Wofford (presenter), T. Schumann, U. Jahn, J. M. J. Lopes, and H. Riechert, *MBE growth of atomically thin h-BN on polycrystalline Ni foils* (poster presentation), MRS spring meeting, San Francisco, US, April 2015.

J. M. J. Lopes, J. M. Wofford, M. H. Oliveira J., T. Schumann, S. Nakhaie, R. Gargallo-Caballero, M. Ramsteiner, M. Hanke, U. Jahn, S. Fölsch, B. Jenichen, A. Trampert, L. Geelhaar, and H. Riechert, *Growth of graphene layers on different substrates by molecular beam epitaxy* (invited talk), 18th International Conference on Molecular-Beam Epitaxy (MBE2014), Arizona, US, September 2014.

Abbreviations

2D	two-dimensional
3D	three-dimensional
AFM	atomic force microscope / -microscopy
arb. u.	arbitrary units
BSE	backscattered electrons
CVD	chemical vapor deposition
ET	Everhart-Thornley
FWHM	full width at half maximum
GID	grazing incidence diffraction
h-BN	hexagonal boron nitride
HOPG	highly oriented pyrolytic graphite
MBE	molecular beam epitaxy
ML	monolayers
PVD	physical vapor deposition
QMS	quadrapole mass spectrometer
RHEED	reflection high energy electron diffraction
RMS	root-mean-square
sccm	standard cubic centimeter
SE	secondary electrons
SEM	scanning electron microscope / -microscopy
STM	scanning tunneling microscope / -microscopy
UHV	ultra-high vacuum
UV	ultraviolet
XPS	X-ray photoelectron spectroscopy
XRR	X-ray reflectivity

Contents

1 Introduction

1.1 Graphene

Graphene is the name attributed to a single layer of carbon atoms, bonded in a two-dimensional (2D) hexagonal crystal lattice, with sp^2-hybridized covalent bonds.[1]

The discovery of graphene has ignited a firestorm of activities across the scientific community and the corporate research world. Andre Geim and Konstantin Novoselov, physicists of the university of Manchester, were awarded the Nobel Prize in Physics in 2010 "for groundbreaking experiments regarding the 2D material graphene".

The history of research on 2D materials has its roots in the 20^{th} century. As noted by Geim and Novoselov[2], the earliest theoretical investigation on graphene dates back to 1947, when the band structure of one-atom-thick graphite was calculated by Philip Wallace.[3] In 1962, Boehm et al.[4] for the first time reported the synthesis of graphene flakes, which were obtained through reduction of graphene oxide dispersions. Since then, there were some successful reports for the production of graphene.[5–7] However, it was only in 2004, that physicists in Manchester were able to exfoliate graphene flakes from highly oriented pyrolytic graphite (HOPG) using adhesive tape and report some of its unique electronic properties.[8] This discovery motivated the researchers to investigate the peculiar properties of graphene and its synthesis techniques.

This one-atom-thick sheet of carbon possesses remarkable properties, which have made it exceptionally attractive for various fields of research in physics, materials science, chemistry, and biology. Excellent electronic properties such as charge carrier mobility as high as 200000 $cm^2V^{-1}s^{-1}$,[9,10] and sustainability of high current densities, orders of magnitude better than copper (assuming the same thickness),[11] superior mechanical properties even comparable to those of diamond[12,13], excellent thermal conductivity[14,15], and its high optical transparency in a broad range of wavelengths from near infrared to ultraviolet (UV),[16] give graphene the potential to compete with conventional materials in several research and industrial branches. However, it should be noted that, in addition to one-atom-thick perfect single crystals of hexagonally sp^2-bonded C atoms, the term graphene is also frequently used for the C materials composed of few or multiple graphene layers stacked on top of each other, as well as graphene layer(s) with diverse range of crystalline perfection. For more detailed information on advances in graphene research, one can refer to several studies, in which the properties of graphene and the latest improvements in its synthesis techniques are reviewed (for example References [2,17,18]). Following a brief summary of graphene properties and its synthesis techniques are provided.

1.1.1 Properties

As previously noted, graphene is a planar arrangement of carbon atoms in a hexagonal lattice. Each C atom in the graphene lattice makes three σ bonds to its three nearest neighbors using its three valance electrons occupying the sp^2-hybridized orbitals. These strong σ bonds are responsible for the planar structure and the unique mechanical properties

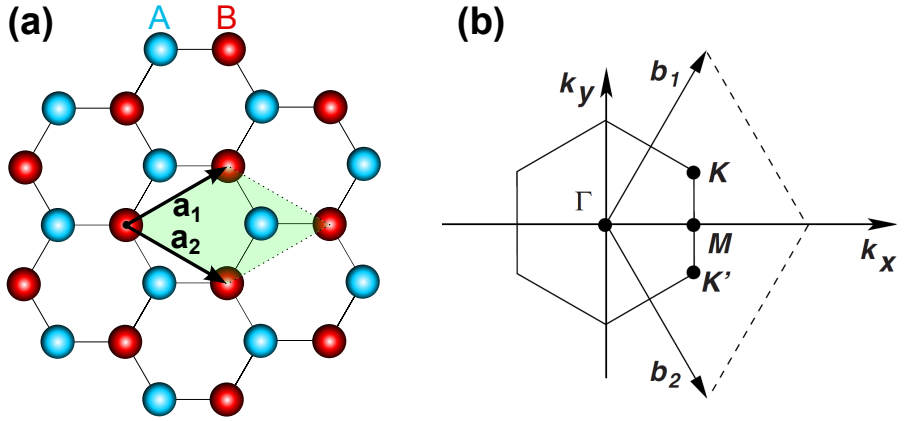

Figure 1.1: (a) Schematic of the graphene lattice structure. The unit cell (green area) is composed of two equal C atoms (sublattice A and B). (b) Brillouin zone of graphene. The reciprocal lattice vectors $\boldsymbol{b_1}$ and $\boldsymbol{b_2}$ and the high symmetry points Γ, M, K and K'are shown (adapted from [19]).

of graphene, such as excellent elasticity and high Young's modulus.[12] The forth valence electron occupies the half-filled $2p_z$ atomic orbital, which is orthogonal to the plane of graphene and forms the delocalized weak π orbitals with the adjacent $2p_z$ orbitals. These delocalized π electrons are responsible for the extraordinary transport properties of graphene.[19]

The unit cell of graphene is composed of two identical C atoms, sublattice A and sublattice B. The two lattice vectors, $\boldsymbol{a_1}$ and $\boldsymbol{a_2}$ can be written as:

$$\boldsymbol{a_1} = \frac{a}{2}(3, \sqrt{3}), \quad \boldsymbol{a_2} = \frac{a}{2}(3, -\sqrt{3}), \tag{1.1}$$

where $a \approx 1.42$ Å is the length of the C–C bond.[19] Accordingly, the lattice parameter can be calculated as $a = |\boldsymbol{a_1}| = |\boldsymbol{a_2}| = 1.42\sqrt{3} = 2.46$ Å, which is consistent with theoretical calculations for graphene and the one of bulk graphite.[20]

The primitive unit cell of graphene in the reciprocal space (i.e. Brillouin zone) are presented in Figure 1.1. The reciprocal lattice vectors $\boldsymbol{b_1}$ and $\boldsymbol{b_2}$ are:

$$\boldsymbol{b_1} = \frac{2\pi}{3a}(1, \sqrt{3}), \quad \boldsymbol{b_2} = \frac{2\pi}{3a}(1, -\sqrt{3}). \tag{1.2}$$

The two points K and K′ in the corners of the Brillouin zone are called Dirac points and are significant for specific properties observed in graphene. Their position in the reciprocal space are:

$$\boldsymbol{K} = \left(\frac{2\pi}{3a}, \frac{2\pi}{3a\sqrt{3}}\right), \quad \boldsymbol{K'} = \left(\frac{2\pi}{3a}, -\frac{2\pi}{3a\sqrt{3}}\right) \tag{1.3}$$

The band structure of single layer graphene calculated based on tight binding model, where only hoping of the electrons to the first and second nearest-neighbors are taken into account, can be written as:[19]

$$E_{\pm}(\boldsymbol{k}) = \pm\hbar t\sqrt{3 + f(\boldsymbol{k})} - \hbar t' f(\boldsymbol{k}), \tag{1.4}$$

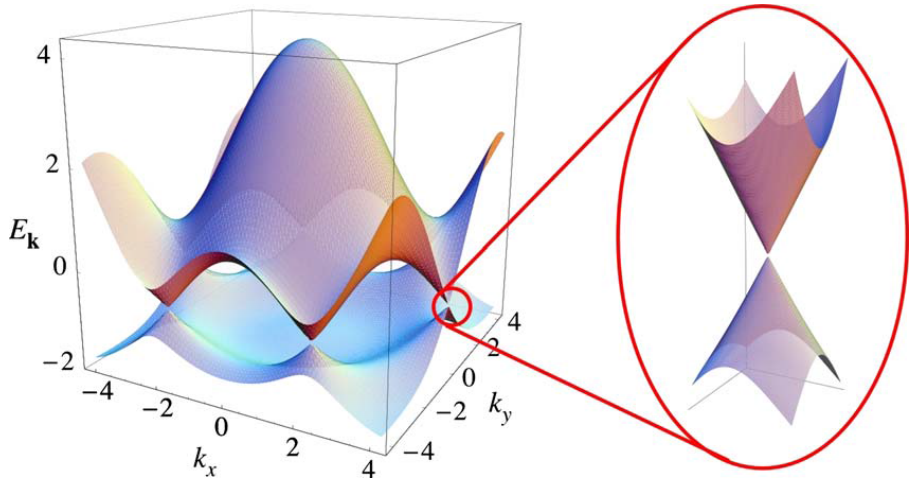

Figure 1.2: Left: an illustration of the π (upper) and π^* (lower) bands in graphene. Right: a zoom-in of the energy band around a Dirac point. Figure is adapted from [19].

with

$$f(\boldsymbol{k}) = 2\cos(\sqrt{3}k_y a) + 4\cos\left(\frac{\sqrt{3}}{2}k_y a\right)\cos\left(\frac{3}{2}K_x a\right), \tag{1.5}$$

where t and t' are the hopping energy of an electron to the nearest-neighbor and next-nearest-neighbor C atom, respectively.[19] The positive and negative signs correspond to upper band (π) and the lower band (π^*), respectively. From Equation 1.4 it can be seen that the band structure is symmetric around zero energy, if $t' = 0$.[a] Near the corners of the Brillouin zone, K (or K') point, the dispersion relation can be simplified by expanding the Equation 1.4 using $\boldsymbol{k} = \boldsymbol{K} + \boldsymbol{q}$, where $\boldsymbol{q}$ is the momentum measured near the Dirac point ($|\boldsymbol{q}| \ll |\boldsymbol{K}|$), and considering only the first term in expansion, as following:

$$E_{\pm}(\boldsymbol{q}) = \pm\hbar v_F |\boldsymbol{q}|, \tag{1.6}$$

where v_F is the *Fermi velocity* which is about 10^6 ms^{-1}.[22] The dispersion relation given by Equation 1.6 obtained for the K (and K') point mimics the one which describes the relativistic massless Dirac particles (i.e. photons), except for the fact that electrons move with a speed v_F, which is about 300 times smaller that the speed of the light.[19] This is the origin of unusual electronic properties of graphene. More detailed explanations on fundamental electronic properties of graphene can be found in References [3,19,20].

1.1.2 Synthesis techniques

High-quality single crystalline flakes of graphene can be obtained by mechanical exfoliation of HOPG using an adhesive tape. This technique which was developed by Novoselov et al.[8] in 2004, is the basis of most of the pioneering as well as recent fundamental studies on graphene. However, besides being very time consuming, mechanical exfoliation is inherently not scalable; the size of the graphene flakes are typically in the range of several tens of microns and not attractive for technological applications.

[a] The value of t' is not quite known, and its estimation depends on the tight binding parametrization. Values of $t' \approx 0.1\ eV$ have been suggested in literature.[19–21]

Therefore, various other techniques have been developed for the scalable production of graphene. In this Subsection, the major methods for the synthesis of *large-area* graphene are briefly presented. The advantages and drawbacks of each technique are explained.

Chemical vapor deposition

Chemical vapor deposition (CVD) is perhaps the most thoroughly explored technique for the synthesis of large-area graphene. Although some early studies report the formation of "monolayer graphite" on the surface of metal single crystals,[5,23] the successful synthesis of few-layer graphene on polycrystalline Ni foils has been reported for the first time in 2006.[24] Since then CVD has emerged as a promising method for the large-area synthesis of graphene.

Generally in this method, a precursor gas (typically a hydrocarbon such as CH_4) flows over the catalytic surface of a metal at high temperatures. The precursor undergoes a pyrolysis reaction and leaves C ad-atoms on the surface for graphene formation. Despite many reports on successful synthesis of graphene on various metals (such as Ni[23,25,26], Cu[27,28], Co[29], Ir[30], Pt[29,31], Pd[29,32]), Ni and Cu continue to be the most common and well understood substrates for this purpose. However, the graphene growth mechanism on Ni and Cu are not similar. This difference stems from the different solubility of C atoms in the metal. In the case of Ni, C ad-atoms can diffuse on the surface as well as into the bulk of the metal, as C has a relatively large solubility in Ni at high temperatures (~ 0.55 at% at 727 °C,[33] and ~ 0.9 at% at 900 °C).[34] Upon cooling the solubility of C in Ni decreases, and the C atoms near the surface regions diffuse out of the bulk and segregate on the surface to form graphene. The graphene film thickness in this method depends on various parameters such as growth temperature, thickness of the Ni and cooling rate.[33,35] Although the possibility to grow few-layer graphene is considered as an advantage of this technique, the weak control over the thickness and the uniformity of the graphene are counted as a drawback. On the other hand, the growth of uniform monolayer graphene on Cu substrates is more straightforward because of the negligible solubility of C in Cu (<0.001 at% at ~ 1000 °C).[36] Therefore, formation of graphene on Cu is a surface catalyst-assisted adsorption rather than segregation or precipitation of C atoms upon cooling of a metastable solid solution of carbon-metal, as in the case of Ni. However, growth of few-layer graphene film on Cu is not possible as the catalytic effect of the substrate is no more available to the precursor, once the surface of Cu is covered with a monolayer of graphene. Apart from thickness control, the CVD grown graphene typically needs to be transferred onto an insulating substrate for application purposes such as device preparation. The post-synthesis transfer process is considered as a drawback to this method, as it might lead to degradation of the structural quality and introducing contamination to graphene.

Graphitization of of SiC

Epitaxial graphene with high structural quality can also be produced by annealing single-crystal SiC(0001) wafers at high temperatures (1000 °C to 1500 °C), in vacuum[37] or in an Ar atmosphere.[38] Upon heating, the Si atoms sublimate from the surface of SiC(0001) (the Si-face) and leave a C-rich surface behind. These C atoms rearrange to form a hexagonal lattice, which is called a *buffer layer*. The buffer layer has one third of its C atoms covalently bonded to the substrate. By further heating the SiC, more Si atoms sublimate and a new buffer layer forms under the first one. This results in decoupling of the first

buffer layer from the substrate, which is the graphene layer. This method of graphene production has been attractive specially for semiconductor industry as the graphene layers already lie on a substrate (SiC) and requires no additional transfer procedure for device processing. However, due to high synthesis temperatures (>1000 °C), this growth technique is not directly compatible with the silicon electronics technology. Also the high cost of SiC wafer production is considered as a major drawback for this growth method.

Molecular beam epitaxy

Large-area graphene can be grown using molecular beam epitaxy (MBE). MBE has been a well know technique for the wafer-scale synthesis of different materials (i.e. III-V semiconductors) with high reproducibility. This technique provides high control over various growth conditions (i.e. precursor fluxes, temperature, pressure) allowing precise control over the thickness and composition. Also a variety of in-situ characterization techniques can be available, thanks to the ultra-high vacuum (UHV) growth conditions. There are several reports of successful growth of graphene on a wide variety of substrates including metals,[39] semiconductors[40,41], insulators[42] indicating suitability of MBE for large-area synthesis of graphene. For instance, MBE growth of graphene with homogeneous and controlled thickness on sapphire substrates has already been shown.[42] Also the possibility to use elemental C source, in principle, provides more flexibility for the choice of substrate, as the catalytic effect of the substrate is not needed for decomposition of a C-containing compound. These properties make MBE a promising method for growth of graphene films. However, although MBE does not meet several constraints of the other techniques, it is comparatively more expensive than other conventional growth methods such as CVD.

In this thesis, MBE is used as the technique to grow graphene under and on top of h-BN films. The former is accomplished by dissolution and precipitation of a precise amount of C atoms from the bulk of metal through a proper modulation of temperature (Chapter 5), while the latter is achieved by direct deposition of C atoms on top of h-BN films (Chapter 6).

1.2 Hexagonal boron nitride (h-BN)

Boron nitride is a III-V compound that exist in various crystalline structures such as cubic, hexagonal, rhombohedral, and wurzite as well as amorphous,[43] with the cubic and hexagonal phases being the equilibrium ones.[43–45] Cubic boron nitride (c-BN) is composed of sp^3-hybridized B and N atoms in a zinc-blende structure (analogous to that of diamond). The bulk hexagonal phase, h-BN, has a layered crystal structure which is similar to graphite. The interaction between the layers are of the weak van der Waals type. Within each layer, B and N atoms are connected with strong sp^2-hybridized covalent bonds in a hexagonal lattice.

1.2.1 Properties

The structure of monolayer h-BN is very similar to the one of graphene shown in Figure 1.1a, with B and N atoms taking the place of the two sublattices. The B–N bond in bulk h-BN has length of about 1.446 Å, which is translated to a lattice parameter of ~ 2.504

Å.[46]. The inter-layer distance in bulk h-BN is 3.33 Å. The typically reported stacking sequence of layers in bulk h-BN is described as AA' stacking; the N atoms in one plane are on top of the N atoms in the bottom plane and vice versa.[44,45] However, other stacking orders have also been reported for few-layer h-BN.[47,48]

H-BN possesses unique properties such as excellent thermal and chemical stability.[49,50] Few-layer h-BN has been reported to be stable in air up to 850 °C.[50] The 2D layers of h-BN can also be used as oxidation protecting coatings which can withstand very high temperatures (i.e. up to 1100 °C for the case of stainless steel and Ni).[51] It is also one of the best thermally conductive materials; the in-plane room temperature thermal conductivity of h-BN has been measured to be as high as 400 $Wm^{-1}K^{-1}$ and up to 250 $Wm^{-1}K^{-1}$ for few-layer h-BN),[52] which makes h-BN an attractive dielectric material also to function as a heat-spreading layer in electronic devices. Furthermore, h-BN's high breakdown field (~8 $MVcm^{-1}$ [53] being comparable to that of SiO_2)[54] make it a promising candidate to be used as high-quality gate dielectric layer in electronic devices.[53,55] H-BN is an insulator with a wide bandgap of ~5.97 eV, making it a promising material for several applications such as ultraviolet lasing.[56] The surface of h-BN is very smooth and relatively free of dangling bonds and trapped charges, which makes it a suitable substrate to support other 2D materials such as graphene.[57]

1.2.2 Synthesis techniques

Until a few years ago, when its natural occurrence was reported,[58] boron nitride was considered to be a synthetic material. For the first time, in 1842 Balmain reported the synthesis of boron nitride, which was obtained from the reaction of molten boric acid (H_3BO_3) and potassium cyanide (KCN).[59] However, commercial h-BN powders used for nowadays standard applications are typically obtained with other techniques and reactants (e.g. Reference [60]). Bulk millimeter-sized single crystals of h-BN can also be obtained with the "high temperature high pressure" method.[61]. Two-dimensional sheets of h-BN can be obtained by a variety of techniques. Similar to graphene, mechanical exfoliation using an adhesive tape can be used to obtain atomic layers of h-BN from its bulk crystal.[62] Following, the major methods for the large-area synthesis of h-BN will introduced.

Chemical vapor deposition

CVD is the most thoroughly explored method for the growth of h-BN films. As early as 1990, CVD was used to grow monolayer h-BN, which was achieved by the decomposition of borazine ($B_3N_3H_6$) on the surface of Pt(111) and Ru(0001).[63] Since then, much research effort has been assigned to develop the CVD growth of h-BN by testing various growth conditions and parameters; successful growth of h-BN has been reported by applying the CVD method at UHV,[64] low pressures,[65] and atmospheric pressure conditions.[66] Various single precursor molecules such as borazine ($B_3N_3H_6$),[63] or trichloroborazine ($B_3N_3H_3Cl_3$),[67] as well as mixtures of two precursor molecules to provide B and N atoms separately, such as ammonia and diborane (NH_3/B_2H_6),[68] have been tested. Also the surface of different metals such as Cu,[65] Ni,[64,69] Pt,[70] Ru,[63,71] Fe[72] have been examined. The CVD method has shown to be promising for the synthesis of large-area h-BN, and all these ongoing studies exhibit the progress being made. However, there are still challenges to be overcome. Getting control over the thickness and homogeneity of the grown films over large areas is a major challenge of this technique. Also the use

of unconventional, unstable, and highly toxic precursors is considered as a drawback of this method. Furthermore, the growth of few-layer h-BN using CVD can meet additional complications, as the catalytic surface of the substrate is no more available for the decomposition of the precursors after covered with the first layer, which affects the growth rate dramatically.[71] Therefore, other techniques for the wafer-scale synthesis of h-BN have also attracted attention recently.

Physical deposition methods

The drawbacks and challenges of the CVD method motivated the research community to develop several physical deposition techniques for the large-area synthesis of 2D h-BN. Examples are the successful reports on the synthesis of 2D h-BN by employing methods such as pulsed laser deposition,[73] deposition via the direct sputtering of a h-BN target with Ar ions,[74] and reactive magnetron sputtering of a B target in high purity Ar/N atmosphere.[75] Besides the traditional physical vapor deposition methods, some novel techniques were also developed for this purpose. For example, formation of atomically thin h-BN films by segregation of B and N atoms on the surface of Co from annealing of a Co/amorphous BN/SiO_2 stack has been reported by Suzuki et al..[76] In general, physical deposition techniques can also be employed to grow h-BN on a variety of substrates such as dielectrics.[75]

As mentioned previously, MBE has been widely used to grow wafer-scale high-quality epitaxial layers of different materials, in particular the III-V compounds. However, despite the advantages it offers (in general accuracy and controllability), this method has not been explored for the synthesis of 2D h-BN, by the time of starting this thesis. The few existing reports of the growth of boron nitride by MBE, focused on the growth of the cubic phase (c-BN) or thick h-BN films for optoelectronic applications.[77,78] In this thesis MBE technique was employed to investigate the growth of atomically thin 2D films of h-BN on Ni foils (Chapter 3), and Ni thin films deposited on MgO(111) substrates (Chapter 4).

1.3 Heterostructures of graphene and h-BN

The perpetual goal of the research world is to replace conventional materials and methods with better, cheaper and more efficient ones. This has been done either by testing various alternative materials for a desired application, or by further developing existing solutions to get the desired properties. Observation of ambipolar field effect in graphene in 2004,[8] manifested how magnificent can be the difference between the properties of a 2D material (graphene) and its bulk counterpart (graphite). This discovery together with its straightforward fabrication method (mechanical exfoliation), motivated researchers to investigate the 2D scheme of several other layered materials such as h-BN, molybdenum disulfide (MoS_2), etc.[62] While the research on the isolated 2D materials has remained intense, recently a significant attention has been attracted towards the engineering of the properties of these materials by combining them into vertical stacks or the so-called van der Waals heterostructures.[79] The heterostructures of the 2D materials, can be considered as new artificial materials exhibiting new physical phenomena, which may enable novel applications.

Among these heterostructures, research on vertical stacks of graphene and h-BN has particularly been extensive. Devices based on the graphene/h-BN material system offer

a host of potential advantages, including high speeds, extremely low power consumption, and various novel functionalities.[80] Much of this promise arises from the intrinsic properties of graphene, although h-BN plays a crucial role in facilitating their effective utilization. Whereas many conventional dielectrics, such as SiO_2, partially mask the useful properties of graphene, the atomically smooth surface and homogeneous charge potential offered by h-BN allow their fullest expression.[57,81] For instance, one order of magnitude higher charge carrier mobility was measured in graphene supported by h-BN as compared to those supported by SiO_2.[57,82] H-BN can also serve purposes beyond that of simple passive mechanical support such as tunneling barriers.[53,83] Britnell et al.[83] demonstrated the feasibility of using a monolayer h-BN (separating two graphene electrodes) as a good tunnel barrier for electrons, which can withstand bias voltages as large as 1 V without breakdown. This enables an even wider variety of device architectures such as tunneling transistors[55] and tunneling diodes.[84] These considerations have drawn the focus of researchers towards the exploration and effective production of heterostructures containing graphene and h-BN.

Graphene and h-BN share the same layered crystal structure and in-plane hexagonal symmetry, with a lattice mismatch of only ~1.7%. Despite this inherent structural compatibility, most successful demonstration heterostructures have relied on stacked flakes which have been mechanically exfoliated from bulk samples of the two materials.[53,55,57,83–85] However, this method is inherently unscalable, and any interface contamination introduced during the transfer process would adversely impact the properties of final devices. Therefore, the direct synthesis of large-area graphene and h-BN through additive growth will ultimately be required. Several attempts aiming at the preparation of vertical heterostructures combining graphene and h-BN by employing different methods have been reported.[86–95] Despite the considerable progress that has been achieved, the realization of heterostructure films (graphene on h-BN or h-BN on graphene) which offer high crystalline quality and are continuous over large areas remains a central challenge. In particular, these results suggest that the synthesis of continuous h-BN on top of graphene poses additional difficulties when compared to growing graphene on h-BN.[94,95]

Among the various approaches to synthesizing heterostructures of h-BN and graphene, MBE offers precise control over growth conditions. Whereas CVD growth relies on the decomposition of a molecular precursor, the rate of which may change dramatically with the exposed surface area of the catalytic substrate,[71] MBE faces no such constraints. The absence of catalytic processes in MBE growth is crucial for vertically stacked heterostructures, where the non-catalytic surfaces of graphene, h-BN, or other dielectrics will serve as substrates for growth. Furthermore, similar considerations such as precise control over fluxes and resulting growth rates, the flexibility to chose elemental as well as compound sources, accurate control over doping, and the possibility of in-situ characterization methods make MBE ideal for fundamental studies regarding the synthesis of heterostructures of h-BN and graphene, the results from which may also benefit synthesis by other methods.

In this thesis, the growth of large-area 2D vertical heterostructures of h-BN/graphene (h-BN on top of graphene – Chapter 5) and graphene/h-BN (graphene on top of h-BN – Chapter 6) by means of MBE has been studied.

2 Methods and Background

2.1 Molecular beam epitaxy

MBE is a widely used technique for growing thin epitaxial films of semiconductors, insulators, or metals.[96] In principle, the crystallization of a thin film occurs from the thermal-energy atomic- or molecular-beams of the constituents on the surface in UHV. The substrate is maintained at elevated temperatures in order to enhance the diffusion of the atoms on its surface. Due to the extremely low pressures, the constituents do not interact with each other until they reach the surface of the substrate, which means the absence of parasitic growth. This is one of the most important aspects of the growth using MBE. Thanks to the UHV growth conditions, a number of in-situ characterization techniques such as reflection high energy electron diffraction (RHEED), mass spectroscopy using quadrupole mass spectrometer (QMS), and Auger spectroscopy can in principle be available. The good control over the growth rate offered by the MBE technique allows the production of abrupt heterojunctions and precise doping profiles, required for a variety of device applications. More information about this growth technique can be found in References [96,97].

Figure 2.1 depicts a simplified schematic of the MBE machine used in this work. The MBE machine is composed of three vacuum chambers, namely the load chamber, the preparation chamber, and the growth chamber. After loading, the sample is kept in the load chamber until a pressure in the range of 10^{-8} mbar is reached. This pressure is achieved by subsequent pumping of the chamber with a roughing pump (down to ~ 10^{-3} mbar), and a cryogenic pump, by which a lowest pressure in the range of 10^{-9} mbar can be reached. The substrate is then transferred into the preparation chamber with a base pressure of 10^{-9} to 10^{-10} mbar, which is achieved by an ion pump. The preparation chamber has a rotating block, which contains three unheated sample holders (typically used for storing samples in UHV), and a heated holder which can reach temperatures as high as 600 °C, as measured by a thermocouple at the back side of the heater. It is further equipped with an Ar sputtering gun (IQE 11, SPECS GmbH). In the preparation chamber, the substrates are degassed and bombarded with Ar ions at elevated temperatures for removing the adsorbed humidity and further cleaning of the surface, respectively. Details of substrate preparation treatment vary for the two kinds of substrates used in this work, and are individually given in the related chapters.

The main components in the growth chamber are labeled in the simplified schematic presented in Figure 2.1. In this work, a radio-frequency (RF) plasma source (manufactured by ADDON) was used to generate active N-species. A high-temperature effusion cell (TUBO cell, CreaTec Fischer & Co. GmbH) was used to provide the beam of elemental B. An electron beam (e-beam) evaporator (EBVV series, MBE-Komponenten GmbH) loaded with a HOPG target was employed to provide elemental C beam. A pyrometer (IS 5, LumaSense Technologies) is used to measure the temperature of the substrate during the growth. The substrate manipulator in the growth chamber (CreaTec Fischer & Co. GmbH) is equipped with a non-contact radiative heating system, which is able to

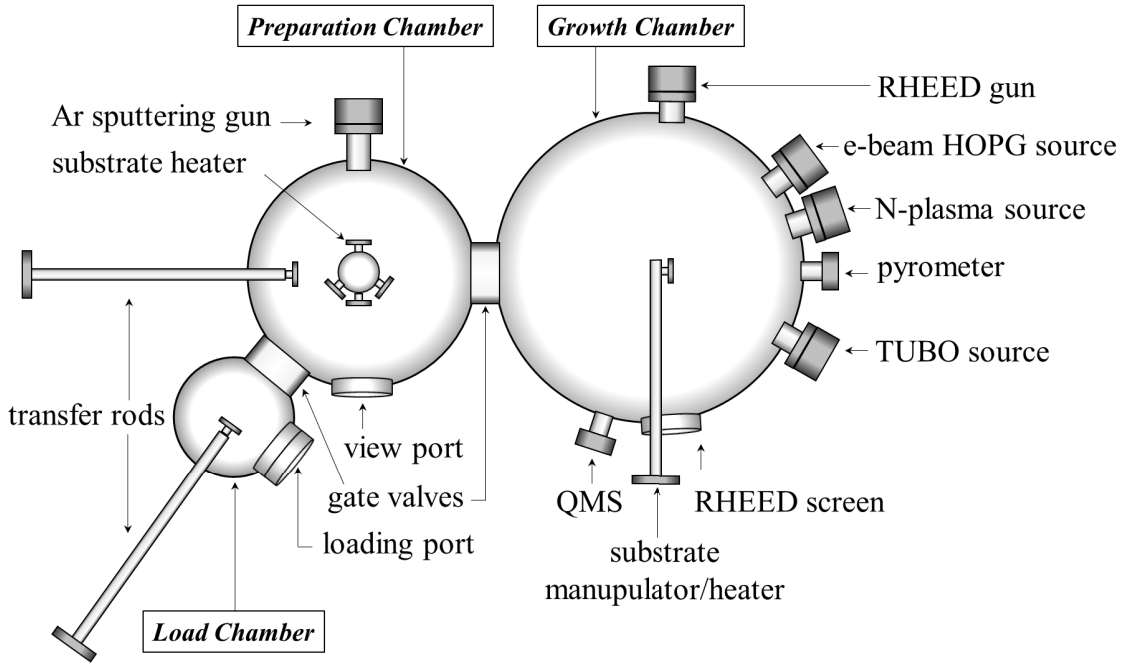

Figure 2.1: Simplified schematic of the MBE used for the growth of samples in this thesis.

heat substrates to temperatures exceeding 1100 °C. Unfortunately the RHEED system appeared to be not suitable for monitoring the growth of the samples studied in this work. The QMS was used to monitor the species present in the growth chamber. A base pressure of 10^{-10} mbar is achieved via a turbo molecular and an ion pump that are installed to the growth chamber. The pressure in the growth chamber during the growth of h-BN increased to ~ 1.2×10^{-5} mbar as a result of introducing N-species [obtained from 0.2 standard cubic centimeter (sccm) of N_2 gas] into the chamber. Also during the growth of graphene, the pressure increased to the order of 10^{-8} mbar. According to QMS data, N-species (mostly N_2) were responsible for a high portion of this pressure. The desorption of N-species (which are introduced during h-BN growth) from the heated surfaces around the e-beam evaporator is most likely the reason for this.

2.2 Raman spectroscopy

Raman spectroscopy is powerful, fast, and non-destructive method for characterization and analysis of various materials. This technique is widely used for studying the properties of carbon materials, in particular graphene. In this section, after a short introduction to the fundamentals of Raman spectroscopy, the background knowledge necessary for understanding the results of this work will be provided. More general information about Raman spectroscopy can be found in Reference [98].

Upon interaction of light (photons) with matter, a portion of light undergoes scattering. Most of the scattered photons experience *elastic scattering* (or *Rayleigh scattering*). In elastic scattering, the energy (frequency) of the scattered (emitted) photon remains the same as that of the incident photon, yet its propagation direction might be different than the incident photon. However, a small portion of the photons experience *inelastic* or *Raman scattering*. In Raman scattering, the incident photon may lose part of its energy after

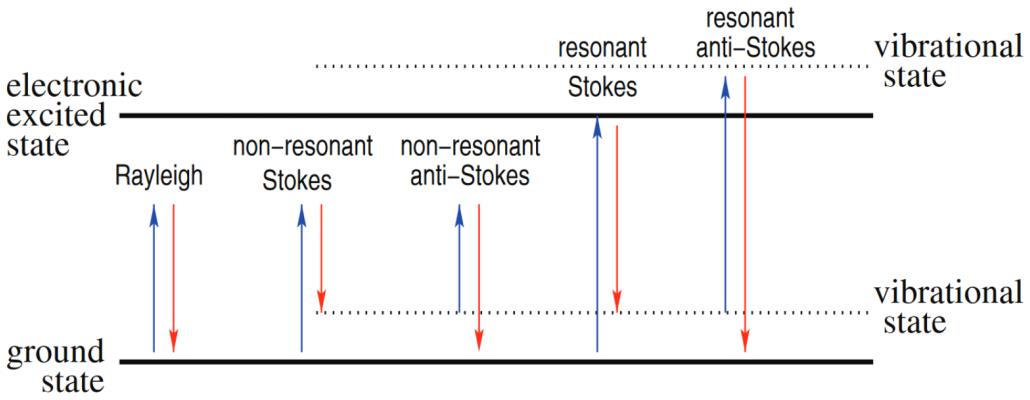

Figure 2.2: Rayleigh and Raman scattering processes in resonant and non resonant conditions (adapted from [99]).

interacting with the material. In a *Stokes* process, the energy of the incident photon is higher than the scattered photon. The energy difference is compensated by a lattice vibration (phonon), which is induced in the material and brings it to an excited vibrational state. An incident photon may also interact with an excited vibrational state of the material, and after this interaction, the material returns back to its ground state. Thus, the scattered photon leaves the material with an increase in its energy, which corresponds to the energy of the excited vibrational state of the material. This is called the *anti-Stokes* process. In general, the probability of a material being it its ground state is much higher than being in its excited vibrational state. Thus, the Stokes process occurs more frequent than the anti-Stokes process.

Raman spectroscopy is based on the inelastic scattering of monochromatic light (photons with a certain energy provided by a laser) with a material. In a Raman spectrum, the intensity of the scattered light is plotted as a function of the difference between its energy and that of the incident photons. Traditionally, this energy difference, which is called Raman shift, is shown in the units of wavenumber "cm^{-1}", and can be converted to the more conventional energy unit eV with the relation 1 eV= 8065.54 cm^{-1}. When the energy of the excitation laser is close to the energy needed for an electronic transition in the sample, the Raman scattering is strongly enhanced and is regarded as resonant Raman scattering. Figure 2.2 presents a schematic of different possible resonant and non resonant Raman scattering processes in a sample. Unlike conventional semiconductors, graphene has a linear gapless electronic dispersion relation (see Figure 1.2 in Chapter 1). This implies that Raman scattering in graphene is resonant using any excitation laser in the visible range, therefore, the Raman spectrum of graphene allows investigations of its the atomic structure, as well as the electronic properties.

In this work, the Raman spectra were recorded using a LabRAM HR Evolution from Horiba Scientific equipped with a solid state laser with an excitation wavelength of $\lambda = 473$ nm. For the UV Raman measurements an excitation wavelength of $\lambda = 244$ nm was generated using a frequency doubled Ar laser made by Coherent.

Raman spectroscopy on graphene

In recent years, Raman spectroscopy of carbon materials in particular graphene has been the subject of many studies. This technique has been used to probe several proper-

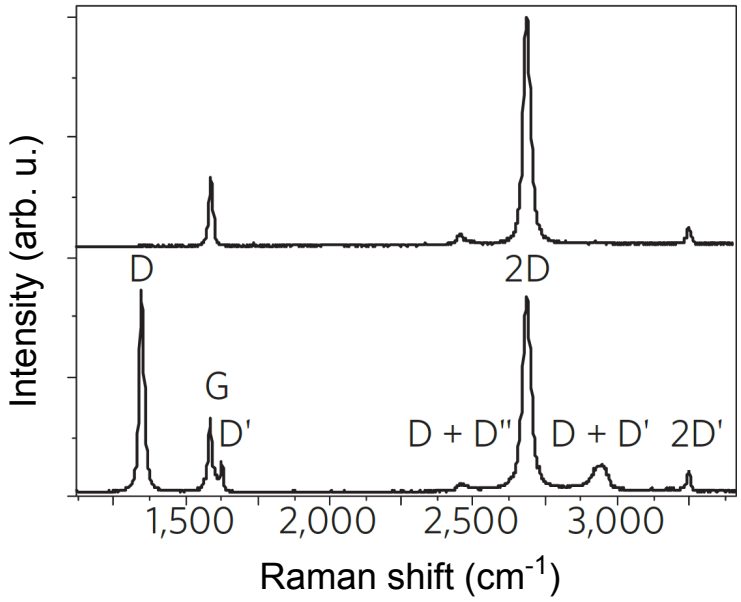

Figure 2.3: Raman spectra of pristine (top) and defective graphene (bottom). The main peaks are labeled (adapted from [99]).

ties of graphene layers such as thermal conductivity,[15] doping,[100] defects and disorder,[101–103] strain,[104] and more. The basics of Raman spectroscopy on graphene will be presented in this section, which helps understanding the results obtained in this work.

Figure 2.3 shows the Raman spectra typical of a pristine and a defected graphene sample. The most prominent Raman peaks of graphene are the G mode appearing at ~1580 cm^{-1} and the 2D mode at ~2700 cm^{-1}. As it can be seen from Figure 2.3, the Raman spectrum of defected graphene additionally contains two defect-induced D (at ~1350 cm^{-1}) and (D' ~1620 cm^{-1}) peaks and their combined modes. Figure 2.4 shows a schematic illustration of some possible Raman processes in graphene. The G peak is associated to doubly degenerate in-plane optical phonon mode, E_{2g}, near the center of the Brillouin zone, Γ point. In real-space, it corresponds to the vibrations of sublattice A against sublattice B in graphene (Figure 2.4b). The D peak related to the transverse optical phonons around the corner of the Brillouin zone, K (or K') point. This peak is due to the breathing mode of the six-atom rings, which requires a defect for its activation. The D peak is a result of resonant transition between two Dirac cones K and K' (intervalley process – see Figure 2.4c).[105] The other defect-induced peak, D', has similar origin as the D peak with the difference that the resonant transition occurs within the same Dirac cone (intravalley process – see Figure 2.4f). The 2D peak is the overtone of the D peak. As it can be seen from the schematic presented in Figure 2.4e, the 2D peak originates from a process which involves two phonons with opposite directions. Therefore, the momentum conservation is satisfied without a defect being required for its activation. Same is true for the 2D' peak. The 2D peak is a result of scattering between two Dirac cones, while for the 2D' the scattering occurs within the same Dirac cone (see Figure 2.4e and g). As a result, these two peaks are also observed in the Raman spectrum of pristine graphene (see Figure 2.3).

As previously noted, the activation of the defect-induced peaks, D and D', as well as their overtones, 2D and 2D' is result of a resonant electronic transition. Therefore,

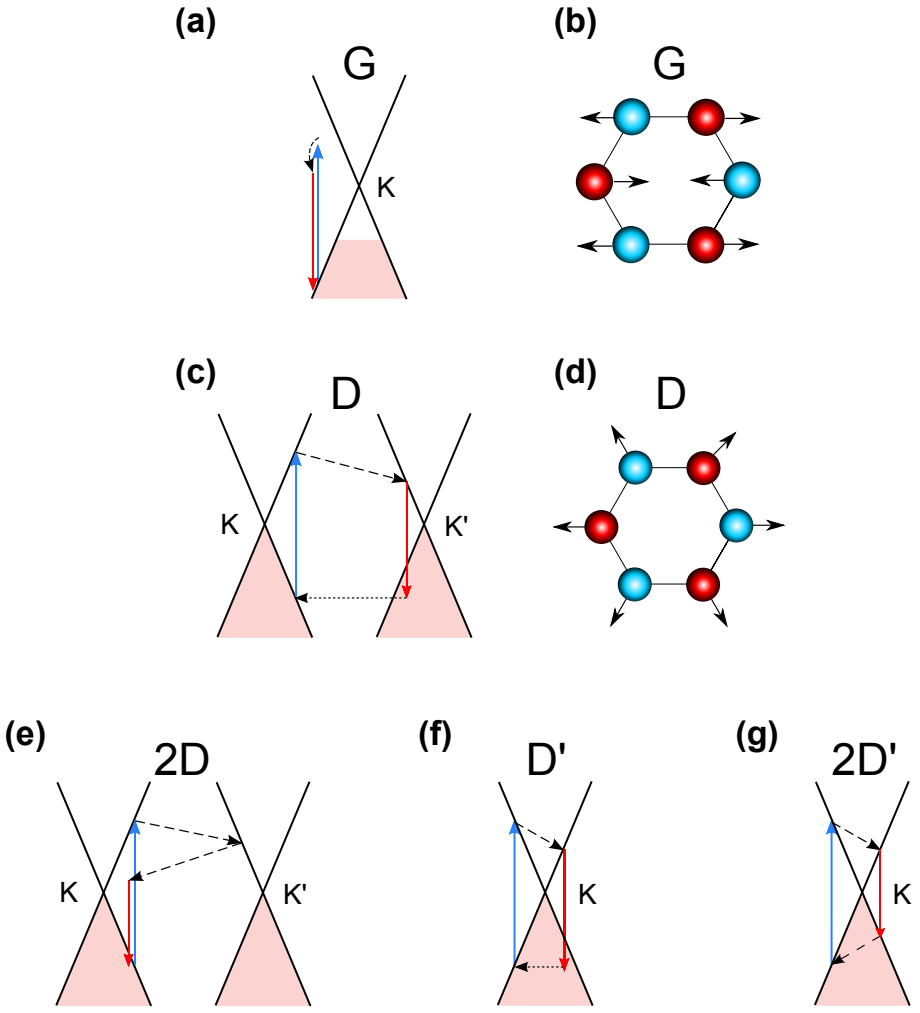

Figure 2.4: Schematic illustration of some Raman processes in graphene. In k-space schematics presented in (a, c, e-g), photon absorption processes are shown by blue arrows, photon emission by red arrows, phonon related interactions by dashed black arrows, and defect related interactions by horizontal dotted arrows. The real space depiction of lattice vibrations causing the G peak and the D peak are shown in (b) and (d), respectively, in which the two identical C atoms, sublattice A and B, are shown by different colors. Pleas note that for the D, D' and 2D peaks, combinations of photon, phonon, and defect scattering can also occur in a different order than depicted here. The D and 2D peaks result from scattering processes occurring between different valleys (intervalley process), while the D' and 2D' peaks result from scattering within the same valley (intravalley process). All possible combinations can be found in Reference [99].

their frequencies are correlated to the electronic band structure and consequently strongly dispersive with the excitation energy.[105,106] Figure 2.5 shows the position of the D peak using different excitation wavelengths. According to the experimental data, the blue-shift of the D peak with excitation energy has a linear rate of ~ 50 $cm^{-1}eV^{-1}$.[99,106] In Chapters 5 and 6, this linear dispersion is used to estimate the expected position of the D peak, when an excitation energy of 5.08 eV instead of 2.62 eV is used in Raman measurements. For more detailed information of the various aspects of Raman spectroscopy on graphene, the

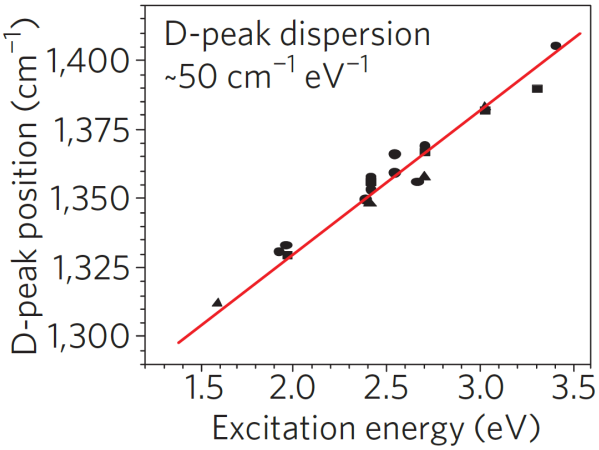

Figure 2.5: Position of the D peak as function of excitation energy (adapted from [99]).

reader is referred to several insightful reviews on the topic such as References [99,107].

2.3 Scanning electron microscopy

Scanning electron microscope (SEM) is a type of electron microscope, which is used in various fields of research. A beam of electrons (primary electron beam) is accelerated and focused on a specimen. Upon impingement of electrons to the sample's surface, they undergo several scattering processes before leaving the sample. The inelastic scattering of primary electron by the specimen, ejects electrons from the atoms of the sample, which are called secondary electrons (SE) and commonly used for imaging the surface. Elastically backscattered primary electrons (BSE) can also be used for certain imaging purposes as they provide useful information on material contrast. The replacement of ejected electrons of an atom by the ones from outer shells produces X-rays, which can be used for identifying the elements present on the surface.

In this project, a Zeiss-Ultra 55 system equipped with two secondary electron detectors – namely the Everhart-Thornley (ET) and the In-Lens detector – was used to obtain images from the samples. Following, a review of the working principles of the two SE detectors will be presented, which will help understanding the images and the corresponding interpretations in the thesis.

In order to explain the working principles of the two detectors, it is necessary to understand the three different types of secondary electrons produced in SEM imaging. The primary electron beam undergoes numerous inelastic scattering processes and generates a large number of secondary electrons. The secondary electrons which are produced from the first scattering process, namely SE1, provide most useful information about the surface. After the first scattering, the primary beam undergoes further scattering processes producing more secondary electrons in the specimen, which are called SE2. The secondary electrons being produced from the interaction of backscattered electrons with other materials (than the specimen) in the SEM chamber are called SE3.

The traditional SE detector – also called Everhart-Thornley (ET) detector – is placed outside the lens system and has an inclined angle relative to the primary beam (or lens system). A positive bias is applied to the detector, which due to its position attracts the secondary electrons of both types, SE1 and SE2, as well as backscattered electrons

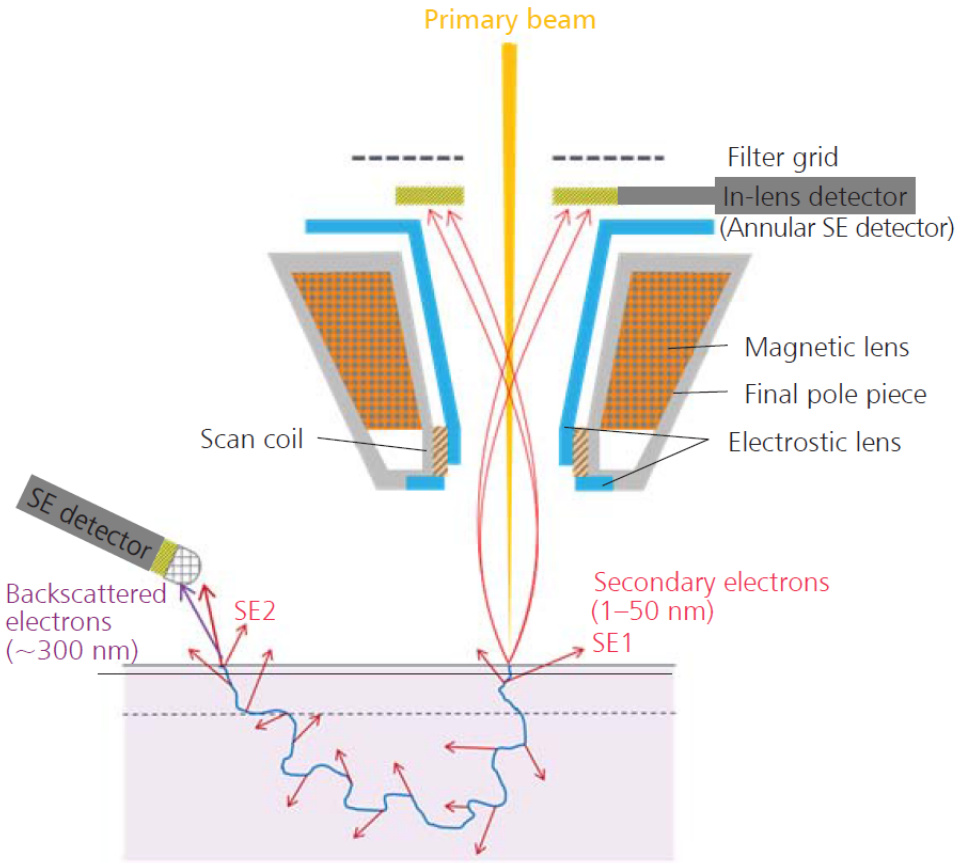

Figure 2.6: Schematic depiction of the detection of secondary electrons using ET and In-Lens detectors in SEM. The In-Lens detector favors the secondary electrons generated in upper regions of the surface (SE1). Figure is adapted from [108].

(BSE). Thus, the inclined angle and the applied bias voltage of the ET detector makes it sensitive to a mixture of electrons which contain information about the depth as well as the topography of the specimen. This can make imaging of extra-thin materials with low atomic number (e.g. graphene or h-BN) more challenging; due to the higher penetration depth of the primary beam in low Z materials (larger volume of interaction), electrons (SE1, SE2 as well as BSE) scape the surface from a larger area, leading to a blurry image recorded by the ET detector.

The relatively newer design enables placing a detector inside the lens column, the so-called In-Lens (or In-Column) detector. This detector is located perpendicular to the primary electron beam (and the specimens surface normal) inside the lens system. In this way, together with the very small working distance, the In-Lens detector exclusively favors the secondary electrons generated in the upper range of the interaction between the primary beam and the specimen surface (SE1 electrons). In other words, the SE1 electrons made at the incidence spot of the primary electron beam and the specimen are attracted, re-accelerated and focused to the In-Lens detector. The SE1 electrons are very efficiently detected by the In-Lens detector due to the position of the detector and the fact that SE1 electrons are directed with the help of electrostatic/electromagnetic lenses toward the detector. Figure 2.6 illustrates a schematic of an SEM system and the position of the In-Lens

and the traditional SE detector (ET detector). Imaging using In-Lens detector is typically done at low voltages.[109] This technique of SE1 detection combined with the low acceleration voltages of the primary beam is markedly important and favorable for the imaging of extra-thin layers. Low acceleration voltage for the primary electron beam means less depth of penetration (lower volume of interaction) resulting in higher surface sensitivity, which is desired for imaging of 2D materials.

2.4 Atomic force microscopy

Atomic force microscopy (AFM) is a widely used method to characterize the topography of surfaces. In this type of microscopy, an atomically sharp tip which is attached to the free end of a cantilever scans over the sample surface. At very small distances between the tip and the surface, the atomic forces between the tip and the surface become considerable and cause a noticeable deflection or bending of the cantilever. The amount of this deflection, is amplified and precisely measured by a laser beam being reflected at the reflective backside of the cantilever and guided to a photodiode detector. This technique allows imaging of the surface with a very high *height* resolution (sub nanometer range), However the *lateral* imaging resolution is in principle limited by the radius of the utilized tip (> 1 nm). Figure 2.7a presents a schematic of main components of an AFM system.

In general, there are two main operational modes of an AFM:

Contact mode: in this mode the tip is brought to an actual physical contact and pushed with a constant force toward the surface (Figure 2.7b). Therefore, the tip feels the repulsive forces from the surface, which can be measured by amount of the cantilever's deflection and its spring constant using the Hooke's law. During the lateral scan of a surface, the deflection of the cantilever is kept constant with the help of a feedback loop, which controls the vertical movements of the scanner. The height information at each measurement point is the distance that the scanner moves in vertical direction, which is used to produce topographic images of the surface. This mode of operation can provide high-resolution topographic images in a short time. However, due to the permanent physical contact of the tip and the surface, a frequent replacement of the tip is needed. Furthermore, the physical contact might also lead to modifications of the surface.

Tapping mode: in this mode, the cantilever is driven to oscillate near its resonance frequency using the piezoelectric components of the scanner. The tip to sample distance is adjusted in a way that the tip slightly "taps" the surface at the bottom of its oscillation. The amplitude of the oscillation is kept constant using a feedback loop, which adjusts the mean distance of the tip to the surface (oscillation amplitude) through vertical movement of the scanner, providing height information of each measurement point.

In this work, a Veeco Digital Instruments - Dimension 3100 AFM system, operating at tapping mode, was employed to obtain topographic images of the samples. In addition to the standard height imaging of the surface, this system allows phase imaging. In this type of imaging, the phase lag of the cantilever oscillation, with respect to the drive signal is simultaneously recorded with the height data, and plotted similarly. As suggested by the manufacturer (Reference [112]) this phase lag is sensitive to variations in different material properties such as composition, adhesion, hardness, friction, viscoelasticity, and more. Furthermore, the edges (sudden changes of the height) become highlighted in phase imaging, while large-scale height changes are not pronounced. In this thesis, phase imaging is only used as a guide to study the topographic (height) images (in Chapters 4 and 6), and no direct conclusion has been drawn based on phase imaging

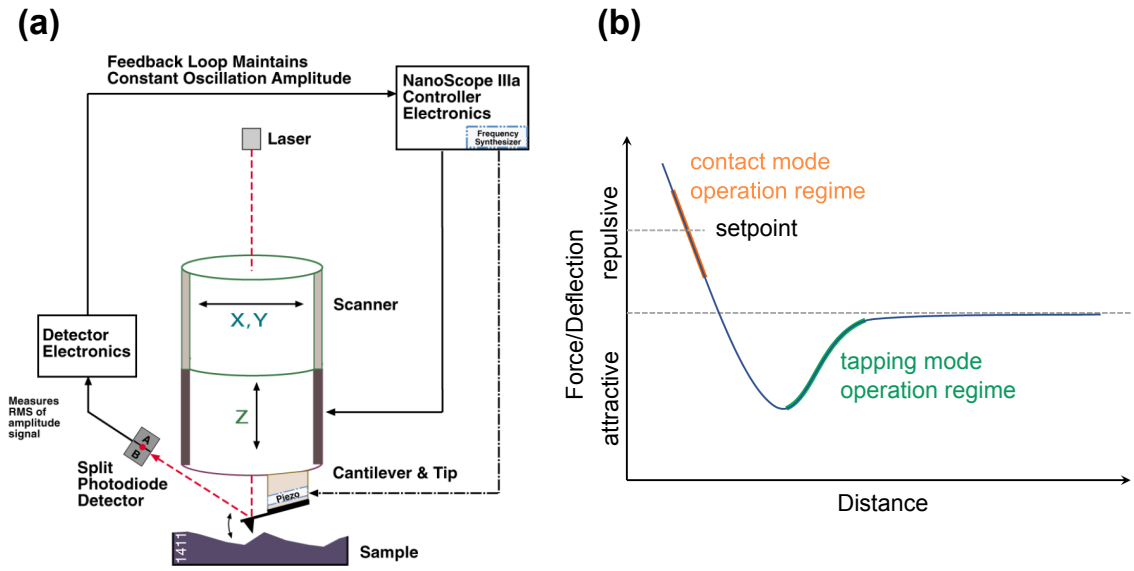

Figure 2.7: (a) Schematic of the AFM system used in this work (tapping mode). Nanoscope is the name of the operating software. Figure adapted from [110]. (b) Simplified schematic of force-distance curve. In contact mode the cantilever is pushed toward the surface (repulsive regime) with a constant force (setpoint). In tapping mode, the tip taps the surface and feels the attractive (van der Waals type) forces from the surface (based on [111]).

technique alone. The reason is that, a reproducible quantitative correlation between the value of the phase lag and the absence/presence or the thickness of the grown material could not be found. For instance, the sign or the amount of the phase lag or both can change, when a single line on the surface is scanned in two directions (left to right or right to left). Additionally, phase images were often prone to high noise. More often than rare, the optimization of scanning parameters for minimum noise in topographic imaging could only be obtained at the expense of increased noise in phase imaging and vice versa. However, the general comparison of the phase map with the height map could sometimes give insight into some surface properties such as material contrast. Although a systematic study of the phase imaging and a clear understanding of contrast mechanism can be quite insightful for development of surface scanning probe techniques, it lies out of the scope of this thesis.

Further general information about AFM can be found in Reference [111].

2.5 Grazing incidence X-ray diffraction

Grazing incidence X-ray diffraction (GID) is a technique which is used for characterization of thin films. Similar to conventional X-ray diffraction (XRD) techniques, its principle is based on the diffraction of X-rays by lattice planes of a crystalline sample according to Bragg's law. However, conventional XRD measurements with large incident angles on thin film (i.e. 2D layers) produces extremely weak signals from the thin film itself as compared to the substrate, due to high penetration depth of X-rays. In GID technique, X-rays are irradiated to the sample's surface at a grazing incident angle near or below the critical angle of total reflection. Therefore, the incident beam is evanescent within the

surface layers (~10 nm),[113] which makes this technique sensitive to the surface structure of the sample.

Figure 2.8 presents a schematic of the beam scattering geometry in a GID experiment. The direction of the incident X-ray beam as well as its grazing angle α_i are fixed. The sample and the detector rotate with a 1:2 ratio to perform "$\theta/2\theta$" scan. Furthermore, ω scans with the detector stationary at a fixed 2θ angle can provide information about the in-plane rotation of crystallites in a thin film.

More information about this technique can be found in Reference [113].

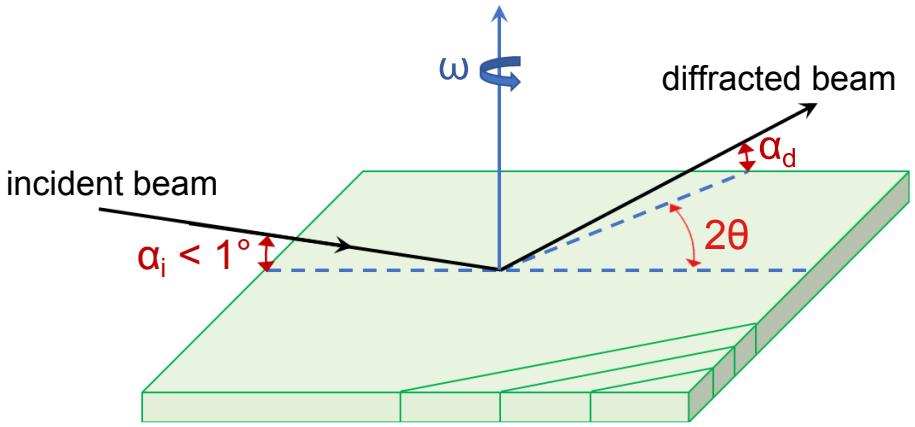

Figure 2.8: Schematic of the beam scattering geometry in a GID measurement. α_i and α_d are the angle of incidence and diffraction, respectively. Figure based on [113].

2.6 X-ray reflectivity

X-ray reflectivity (XRR) is a non-destructive surface sensitive technique to characterize thin films or multilayer of materials irrespective of being crystalline or amorphous. In general, electromagnetic waves (including X-rays) passing the interface of two materials with different refractive indices, are partly transmitted and partly reflected. If they irradiate the surface of a sample at a grazing angle θ smaller than a critical angle θ_c total reflection occurs. Thus, X-ray reflectivity is related to the refractive index of the materials being probed, as well as the X-ray wavelength. If the sample is composed of different layers of materials, X-rays reflected from the surface and the interfaces of layers with different refractive indices undergo constructive and destructive interference, which appear as intensity oscillations at the detector. These oscillations which were observed for the first time by Heinz Kiessig,[114] can be employed to determine the thickness of the layers.[115]

Generally, the experimental curve is compared with the one obtained from simulations based on theoretical models in which, in addition to the refractive indices the roughness at the interfaces, as well as multiple reflections at the interfaces are also considered,[116] allowing precise analysis of deposited thin films. Further information about this technique can be found in Reference [115].

2.7 X-ray photoelectron spectroscopy

X-ray photoelectron spectroscopy (XPS) is a widely used analysis technique in surface science. This technique has played an essential role in development of thin films research due to its high surface sensitivity, the precise and quantitative information it provide, as well as its flexibility to be applied to a broad range of samples. XPS can be employed to obtain various information about the surface of the materials such as composition, chemical state of elements, and chemical bond strengths.

This technique is based on the emission of electrons from a material upon interaction with photons – the photoelectric effect. High energy photons are able to eject electrons from inner electronic shells of an atom. The principle of XPS relies on analyzing the kinetic energy of an electron ejected from a core level of an element upon interaction with X-rays. The energy conservation in this process can be expressed as:[117]

$$BE = h\nu - KE - \phi, \tag{2.1}$$

where BE is the binding energy of the electron, $h\nu$ is the energy of the X-ray photon, KE is the kinetic energy of the ejected electron (photoelectron) which is measured by the spectrometer, and ϕ is the work function (related to the spectrometer and sample), which is commonly considered as an adjustable correction factor of a spectrometer. X-rays can be generated by standard laboratory sources (i.e. Al K-alpha radiation) or by synchrotron sources. A monochromator may be used for reducing the line width of X-rays. An electron energy analyzer counts the number of photoelectrons over a range of kinetic energies. The obtained intensity is typically plotted as a function of electron binding energies in a reverse order. The binding energy of the photoelectron peaks allow identification of elements and their chemical state on the surface, while the intensity of the peaks can be used for quantification analyses such as composition ratio of surface elements.

Further general information about this technique can be found in References [117,118].

3 Growth of h-BN on Ni foils

In this chapter, growth of h-BN on polycrystalline Ni Foils is investigated. The focus of this study is primarily the realization of the growth of continuous and atomically-thin (2D) h-BN on Ni substrates using MBE, which may be considered as a pioneering work in the field.[119] The growth parameters which yield a continuous film are included. The presence of crystalline h-BN was confirmed by Raman spectroscopy. AFM was used to examine the surface morphology as well as the continuity of the films. Synchrotron-based X-ray reflectivity (XRR) has been employed to estimate the thickness of the continuous films. The XRR measurements have been performed at the U125/2-KMC beamline (BESSYII Helmholtz-Zentrum Berlin) by collaboration with Michael Hanke from the department of microstructure, Paul-Drude-Institut für Festkörperelektronik, Berlin. Moreover, samples with shorter growth durations were studied using SEM, which allowed gaining insight into the nucleation and growth behavior of the h-BN on Ni foils.

The material Ni is chosen as the growth template because a number of studies show its suitability for synthesis of large area h-BN,[64,68,120] as well as being a relatively well-known environment for the growth of graphene (and graphite).[33,121,122] For the beginning, we chose Ni *foils* mainly because they are inexpensive and easily accessible through commercial suppliers. This helped saving considerable amount of time and effort during the initial part of the project which involved many trial and error steps. Moreover, using foils as the growth substrate can be specially attractive for certain research aspects, for example where mechanical flexibility is desired, as well as industrial applications where cost plays a role.

3.1 Experimental

Polycrystalline Ni foils (Alfa Aesar, 99.994% pure, 100 µm thick) were cut into 1×1 cm^2 pieces and cleaned using conventional solvents (acetone and isopropanol) and water prior to loading into the UHV chamber. The foils were then annealed in UHV for 20 minutes at 600 °C followed by an Ar sputtering step with a 2 kV acceleration voltage, and 10^{-4} mbar Ar pressure for another 20 minutes at the same temperature. The annealing and Ar sputtering steps are designed for desorbing water (caused by handling of the substrate in air) and further cleaning of the surface of the foils (from contaminations or Ni oxide). After cooled down in the preparation chamber, the foils were transferred into the growth chamber and annealed at 1000 °C for 30 minutes, before starting the h-BN deposition. This annealing step helps increasing the grain size of Ni crystallites as well as further cleaning of the surface from possible remaining Ni oxide. Figure 3.1 shows an AFM image of a Ni foil after annealing in the growth chamber. Although the image was taken immediately after unloading the sample from UHV, due to the fast oxidation of the Ni in air, the surface features such as atomic Ni steps do not appear sharp in the AFM image.

A high-temperature effusion cell (TUBO cell, CreaTec Fischer & Co. GmbH) operating at 1850 °C was used to provide the beam of elemental B with a flux of ~2.7×10^{12}

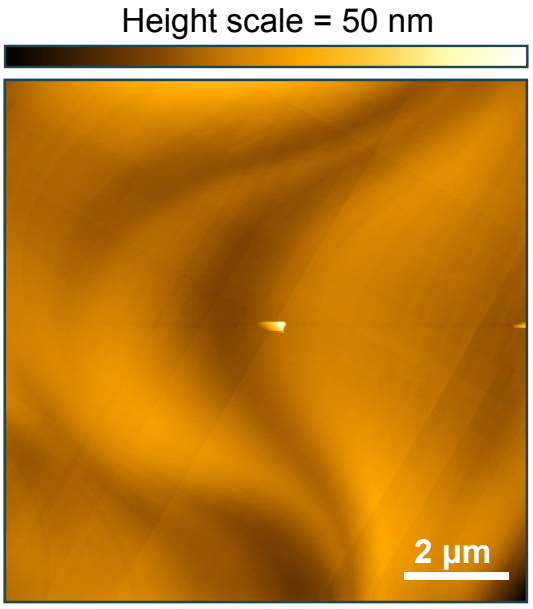

Figure 3.1: AFM of the Ni foil, after annealing in the growth chamber and prior to the growth of h-BN.

atoms/cm^{2}s. The B flux was obtained by calculating the number of atoms in a B film deposited at room temperature on a sapphire substrates over 600 minutes, with considering the density of B[123] and ex-situ AFM measurement of the deposited B film thickness. This B flux corresponds to a h-BN growth rate of ~5.3 monolayers per hour, if it is assumed that all the B atoms can remain on the surface and form h-BN. Active N-species were generated using an RF plasma source operating at 350 W with 0.2 sccm of N_2 flow, which resulted in a chamber pressure of 1.2×10^{-5} mbar during the growth. Films were synthesized over 180 to 300 minutes at two different substrate temperatures: 730 °C and 835 °C, as measured by an optical pyrometer.

3.2 Continuity and structural quality of h-BN films

The growth of crystalline h-BN on the Ni foils was initially confirmed using Raman spectroscopy. Figure 3.2a depicts a representative Raman spectrum of a h-BN sample synthesized over 300 minutes at 730 °C. The Raman spectra measured from the as-grown h-BN films are superimposed to a relatively strong background originating from the Ni substrate. For the spectrum shown in Figure 3.2a, this background signal has been subtracted. A spectrum before background subtraction as well as the Ni background spectrum is illustrated in Figure 3.2b. The sharp peak observed at ~1365 cm^{-1}, which arises from the doubly degenerate in-plane optical phonons of h-BN with E_{2g} symmetry, is indicative of high-quality h-BN.[124] The Raman signal was detected in all measurements over the surface, which can be considered as a first confirmation for the film continuity.

The surface morphology resulting from a synthesis at 730 °C over 300 minutes was evaluated by AFM. Figure 3.3 illustrates two AFM images typical of the growth with the mentioned growth parameters. The root-mean-square (RMS) roughness of the h-BN film was measured to be 1.0 and 0.3 nm over 1×1 µm^2 and 0.1×0.1 µm^2 areas, respectively. Uneven regions of the underlying Ni surface resulted in higher RMS values in some ar-

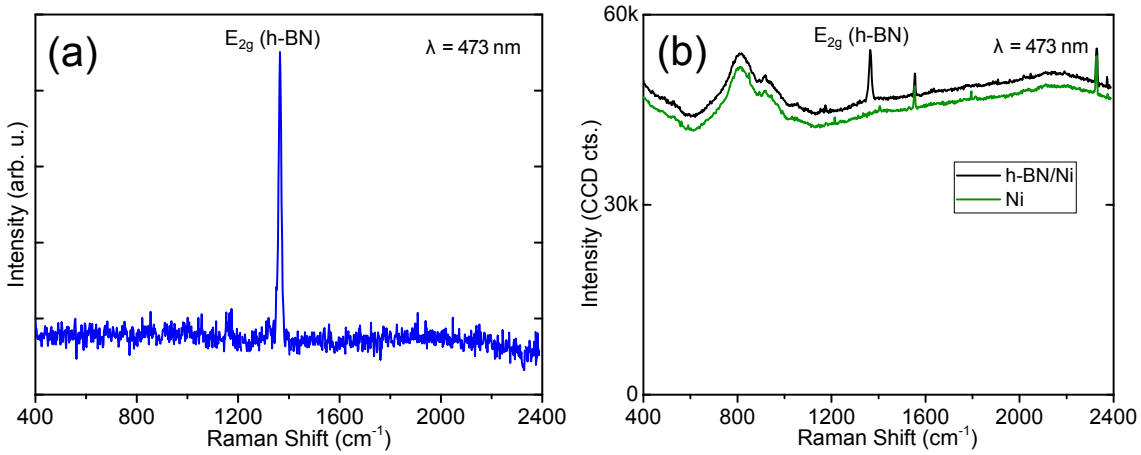

Figure 3.2: (a) Raman spectrum collected from a continuous h-BN film on Ni synthesized at 730 °C over 300 minutes. The substrate-related background signal is subtracted. (b) The Raman spectrum from the continuous film before background subtraction (black) as well as the spectrum from a bare Ni substrate (green). An offset is applied for better visualization. The spectra were excited at a wavelength of 473 nm with the laser beam focused onto the sample surface to ~1 µm diameter spot.

eas. Profile measurements from edges of the h-BN film showed 0.5–1.5 nm steps down to the bare Ni, revealing that the film is composed of few atomic layers of h-BN (the interlayer distance in h-BN is ~0.3 nm).[45] AFM also allowed the continuity of the h-BN films to be confirmed, as described following. In addition to the topographic features of the underlying Ni foil, such as step edges and terraces, a cellular array of linear features is easily discernible which are identified as wrinkles (Figure 3.3, red arrows). The h-BN film is expected to develop wrinkles during sample cooling due the relaxation of compressive strain in the h-BN arising from the unequal expansion coefficients of h-BN[44] and Ni.[125] In other words, due to the negative expansion coefficient of h-BN,[44,46] it tends to expand during cooling from growth temperature, while the Ni foil shrinks. As the h-BN does not freely slide on the Ni surface (i.e. due to pinning at grain boundaries or non-zero interaction with Ni), wrinkles are formed. Such wrinkles have been observed previously in both h-BN and graphene grown on metal substrates.[27,65,70] These wrinkles were not present on the bare Ni surface. The ubiquity of the wrinkle structure in numerous AFM scans, together with the uninterrupted observation of the h-BN Raman signal, offers strong evidence of a continuous h-BN film.

AFM scans also show a second distinct type of feature in the h-BN films. Rather than having a smooth profile along their length as the h-BN wrinkles do, these rougher raised regions appear to be decorated with a line of discrete "dots". The "dotted" features also protrude higher out of the plane of the film than the wrinkles (typically ~15 nm versus ~5 nm – see inset in Figure 3.3a) and are sufficiently pronounced to be evident even in larger area AFM scans (Figure 3.3b). These distinctions are sufficient to suggest that the two types of features form due to different mechanisms. Although this alternative mechanism is not yet clear, we speculate the dotted ridges may mark grain boundaries in a polycrystalline h-BN film. For instance, surface contaminants (e.g., from Ni foil)[126] or excess surface B (e.g., due to B-rich growth conditions) could be pushed by the growth front of the expanding h-BN crystal, with the consequent accumulation of material at grain boundaries leading to the formation of the observed "dots".

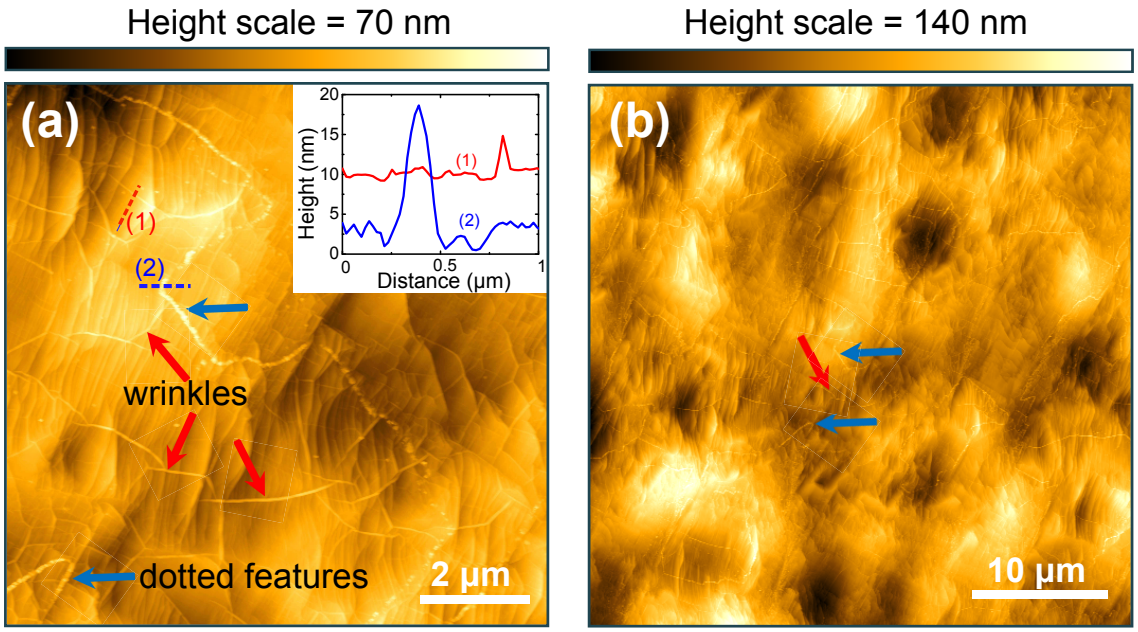

Figure 3.3: AFM images from a continuous h-BN film on Ni foil (300 minutes, 730 °C). (a) Two distinct types of ridges, marked with red and blue arrows, are observed across the entire area of the film. The smooth, continuous ridges are wrinkles in h-BN (red arrows), while the objects marked with blue arrows are discontinuous and appear dotted. The inset shows the line scans (1) and (2) obtained across a wrinkle and a dotted feature, respectively. The dotted features are ~15 nm high, while the wrinkles ~5 nm. (b) Larger area AFM scan of the same sample region. The blue and red arrows indicate the same features as in (a).

3.3 Thickness estimation by synchrotron-based X-ray reflectivity

Synchrotron-based XRR has been employed to estimate the thickness of the continuous h-BN films. The extremely (i.e., atomically) thin layer, in conjunction with low-Z, and thus weakly scattering constituents (boron and nitrogen) on one hand, and the unevenness of the foils (in millimeter and centimeter scale) on the other hand, necessitated a highly brilliant radiation combined with long signal acquisition for the successful application of this technique. Figure 3.4a shows the reflectivity curve as measured at the U125/2-KMC beam-line (BESSYII, Helmholtz-Zentrum Berlin). An X-ray energy of 10 keV has been selected by a double Si(111) monochromator, which yields an energy resolution ($\Delta E/E$) of about 10^{-4}. Due to the roughness of the underlying Ni foil, as well as the out-of-plane wrinkles and dotted features, the reflected intensity rapidly decreases with increasing the angle of incidence, α_i. Nevertheless, thickness oscillations are clearly traceable in the experiment. Figure 3.4b depicts three kinematic scattering simulations for h-BN layer thicknesses between 0.8 and 1.0 nm on a Ni substrate, in which the refractive indices of the materials and interface roughness were taken into account. From a direct comparison, we can conclude that the averaged h-BN layer thickness is close to 0.9 nm. This shows that the h-BN film is about three atomic layers thick (a single layer corresponds to ~0.3 nm),[45] in agreement with the AFM profile measurements taken at edges of the h-BN film.

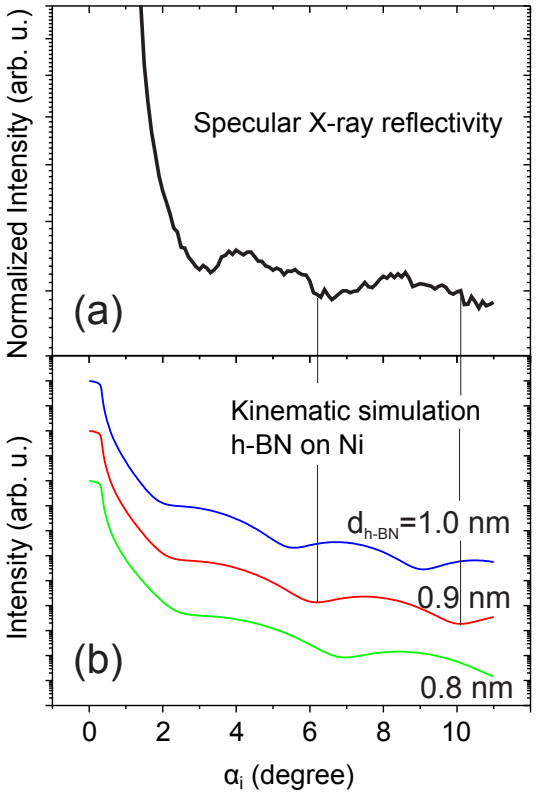

Figure 3.4: XRR measurement and h-BN film thickness estimation. (a) Experimentally observed specularly reflected X-ray intensity collected from a continuous h-BN film on Ni synthesized at 730 °C over 300 minutes. (b) Kinematic scattering simulations for a h-BN layer with the thickness ($d_{h\text{-}BN}$) varying between 0.8 and 1.0 nm on a Ni substrate.

3.4 An insight into nucleation and growth of h-BN on Ni foils

Using shorter duration depositions, we were able to gain insight into the nucleation and growth behavior of h-BN. Growth times of 180 minutes or shorter showed islands of h-BN, which were identifiable by SEM (Figure 3.5). Raman spectroscopy confirmed that these regions are crystalline h-BN.

Figure 3.6 presents a summary of the representative Raman spectra observed for h-BN samples grown over 180 minutes at 730 °C and 835 °C as well as the continuous h-BN film discussed above (synthesized over 300 minutes at 730 °C) after Ni originated background subtraction. For comparison, a Raman spectrum obtained from commercially available h-BN powder is also included. This peak showed slight width variations in numerous Raman measurements, ranging from 10 cm^{-1} to 18 cm^{-1}. The width observed for the MBE-synthesized h-BN is comparable to the those reported for h-BN single crystals (9-12 cm^{-1}),[127] grown by K. Watanabe and T. Taniguchi et al.,[56,61] which are widely used in research as standard high-quality h-BN. The intensity of the peak exhibits some variations, likely as a result of an inhomogeneous thickness distribution. Previous studies suggest that for first several layers, h-BN's E_{2g} peak intensity increases (almost) linearly with the number of probed layers.[127,128] The average peak height to background ratio for the continuous films is ~0.18, while for the ramified and triangular islands this value is ~1.1 and ~3.7, respectively. Since the intensity of the background originating from the

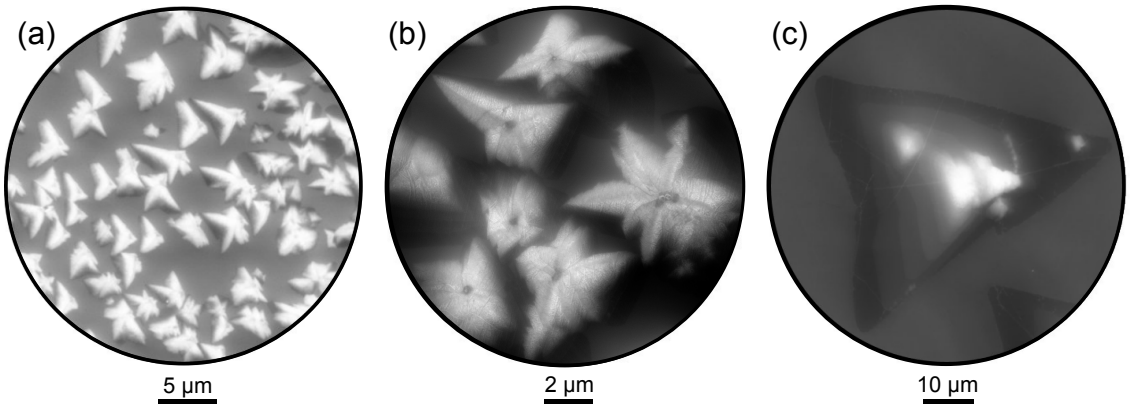

Figure 3.5: SEM micrographs of h-BN grown over 180 minutes (a) and (b) at 730 °C and (c) at 835 °C. The growth at 730 °C results in star-shaped h-BN islands – bright contrast in (a) and (b). When the substrate temperature is raised to 835 °C for growth, much larger islands form, which have a smoother, more compact shape (c). The contrast fluctuations in (c) clearly show that the island is composed of few layers of h-BN. However, contrasts observed in SEM do not provide enough evidence to verify formation of isolated islands. for example in (c) the contrast observed around the triangular island, is very similar to the second bright contrast from the edge of the island. In the other words, these bright regions, which are referred to as islands, can be few-layer h-BN forming on top of a more homogeneous underlying h-BN film. The field of view in (a) is 30 µm, 15 µm in (b), and 70 µm in (c).

underlying Ni is always on the same order of magnitude, the variation in the relative intensity of the characteristic h-BN peak to the background reflects a change in the volume of h-BN being probed, suggesting that the islands are composed of few h-BN layers. This is consistent with the few-layer character of the triangular island shown in Figure 3.5. Finally, we also observed small shifts in the peak position for the different types of h-BN structures. Variation in strain is a potential explanation for the observed shifts.[127,128]

The few-layer islands are speculated to lie on top of an extended and thinner (i.e. monolayer) h-BN film. While the atomistic growth mechanism of h-BN on Ni is unknown, a close examination of the few-layer island structures offers some clues to their origin. For instance, the h-BN islands typically include a small region of prominent contrast at the approximate geometric center of the island, possibly marking a surface defect at which the island nucleated heterogeneously. Heterogeneous nucleation has also been observed previously during the growth of other 2D materials, such as graphene.[129] The surface imperfections at which nucleation occurs here may be clusters of excess surface B, or possibly isolated regions of the intermetallic Ni_3B phase.

The morphology of the h-BN islands changes dramatically with the growth temperature (Figure 3.5). Hexagonal boron nitride islands grown at a substrate temperature of 730 °C have a distinct "star" shape, with multiple elongated lobes extending from a common nucleation site over few micrometer. With the same growth duration but a 835 °C substrate temperature, the h-BN instead forms smooth, compact, approximately triangular islands which are almost an order of magnitude larger. However, isolated regions with shapes other than those depicted in Figure 3.5 have also been observed, possibly due to changes in h-BN growth behavior on different crystallographic orientations of Ni.[130]

Possible explanations for the observed "star" shape can be the formation and propa-

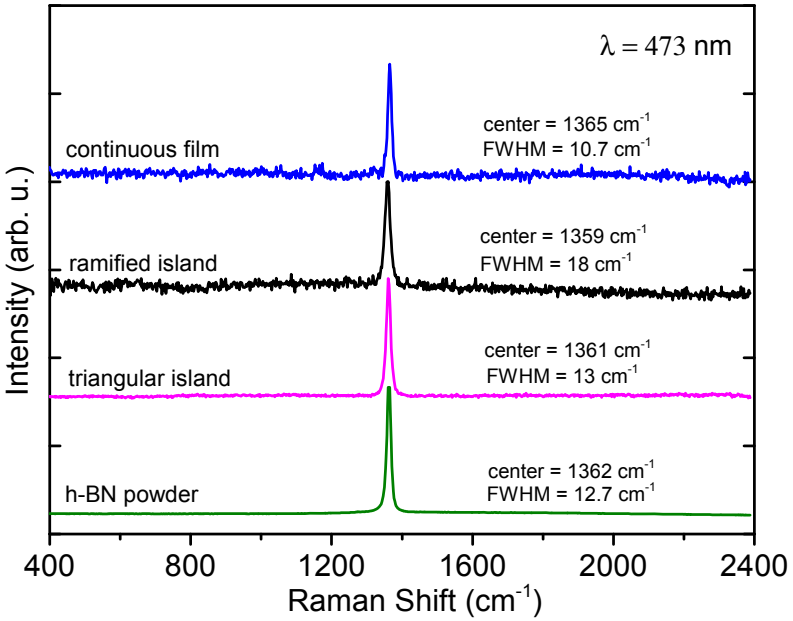

Figure 3.6: Raman spectra collected from a continuous h-BN film on Ni synthesized at 730 °C over 300 minutes (blue), and from h-BN islands grown for 180 minutes at 730 °C (black) and 835 °C (magenta). The substrate-related background signal was subtracted for all three spectra. A Raman spectrum from h-BN powder (green) is plotted for comparison. An excitation wavelength of 473 nm is used for the given spectra.

gation of two (or more) non-parallel triangular islands from the respective two (or more) closely located nucleation sites. Another explanation may be the dendritic growth because of the diffusion-limited aggregation of B and N ad-atoms at low temperatures. Indeed, the dramatic transformation in island morphology and size with growth temperature is more consistent with this possible explanation. On the other hand, it is also interesting to note the superficial similarities between the star-shaped h-BN islands formed on Ni and the morphology of graphene growing on (001) oriented grains in Cu foils. The fairly consistent orientation of the long-axes of the h-BN island lobes is a particularly striking detail to have in common with graphene islands on Cu. In the case of graphene on Cu, the island shape results from a complex interplay between the attachment limited growth mode, the polycrystalline island structure, and the substrate surface crystallography.[129] Whether the h-BN island shape observed here is caused by analogous growth phenomena remains an open question.

The morphology of the larger, compact h-BN structures grown at higher substrate temperatures also has precedent in the literature. Triangular h-BN islands have been reported for CVD grown h-BN on both Ni[67,69] and Cu[65] substrates, and theoretical calculations suggest this is due to the lower free energy of the N-terminated crystal edge.[131] However, because of their significantly larger size, few-layer thickness, random orientation, and deviation from perfectly triangular shapes (for some islands), it is unlikely that the preference for a given edge termination fully explains the morphology presented in Figure 3.5c. Rather the dramatic change in island morphology likely results from an interplay between kinetic factors, such as increased ad-atom diffusion, in combination with the energetic anisotropy of the edge structure. Contrast variations in the interior of the large island in Figure 3.5c reveal its layered structure. As the secondary electron intensity

emitted from h-BN scales linearly with the number of layers,[132] each observable variation likely marks the perimeter of an additional layer. The few-layer thickness imaged by SEM corroborates the Raman analysis (see Figure 3.6), in which the highest peak height to background ratio (~3.7) was obtained for this type of island.

3.5 Summary and conclusions

In summary, we report the growth of atomically thin h-BN films on Ni foils by MBE using elemental B and N. In these experiments, films were synthesized at substrate temperatures ranging from 730 °C to 835 °C over 180 to 300 minutes. The presence of crystalline h-BN was confirmed by Raman spectroscopy, which revealed a sharp peak at ~1365 cm^{-1}. AFM was used to examine the surface morphology of the grown films, and revealed two distinct features which were omnipresent over the entire film: a cellular array of linear features identified as wrinkles, and a second rougher type of ridge. The rougher, "dotted" ridges appear to originate from a different, as yet unknown mechanism. Using shorter growth times, we were able to gain insight into the nucleation and growth behavior of h-BN islands. According to SEM imaging, the morphology of h-BN islands evolves from ramified and "star"-shaped to much larger, smooth, and triangular islands with increasing growth temperature. Scanning electron micrographs also clearly show a small region of prominent contrast in the center of the grown islands, suggesting that the h-BN may have nucleated heterogeneously.

4 Growth of h-BN on Ni films

In this chapter, the results obtained from the h-BN growth experiments on thin Ni films, evaporated on MgO(111) substrates, are presented. Here, besides the optimized growth parameters yielding a continuous h-BN film, effect of the substrate temperature as well as growth duration on the synthesized h-BN will be investigated. The samples are studied using scanning electron microscopy, AFM, Raman spectroscopy. In addition, grazing incidence diffraction measurements were performed at beamline BM25B (SpLine) at the European Synchrotron Radiation Facility, Grenoble, France by collaboration with Michael Hanke and Thilo Krause from the department of microstructure, Paul-Drude-Institut für Festkörperelektronik, Berlin. These experiments helped to analyze the growth behavior and structural quality of the synthesized h-BN films.

Ni films with a thickness of 300 nm were deposited at room temperature on MgO(111) substrates using electron-beam evaporation of a Ni target. The Ni/MgO(111) templates were produced by the technology department of Paul-Drude-Institute. In comparison to Ni foils, better macroscopic evenness and smoothness as well as enhanced mechanical stability of the substrates [provided by the relatively thick MgO(111) crystal] facilitated performing characterization techniques such as GID and AFM. Furthermore, besides the precise control over thickness of the deposited Ni films, presence of possible contamination due to the industrial Ni foil preparation procedure (i.e. the cold-rolling) can be ruled out. In principle, MgO(111) allows the growth of fully epitaxial Ni(111) mono-crystalline films, if certain growth recipe and temperature treatment is applied,[133] and thus, can offer an extra-smooth surface for the growth of 2D materials such as graphene.[39] Initially, it was tried to grow the Ni films on MgO(111) substrates in our MBE system. However, due to the low flux obtained from the Ni effusion source, extremely long deposition duration was needed to obtain the desired thickness (as it will become clear in Chapter 4, relatively thick Ni film is needed for the growth of h-BN/graphene heterostructures). Therefore, in order to put more focus on the growth of the 2D materials (h-BN in this chapter and heterostructures in the next two chapters), we decided to use the Ni/MgO(111) templates produced by the technology department of the Paul-Drude-Institut, and enhance the surface quality by in-situ sputtering and annealing treatment of the templates before h-BN growth.

4.1 Experimental

Substrates were prepared by depositing at room temperature 300 nm of Ni on 1×1 cm^2 pieces of MgO(111) (purchased from CrysTec GmbH, single-side polished) by electron beam evaporation, and back-coating them with 1 µm of Ti. The Ti coating layer at the back side of the transparent MgO(111) substrate is necessary, as the sample is heated radiatively during annealing and growth. For the sake of simplicity, from here on, this stack will be referred to as Ni/MgO(111). The Ni/MgO(111) templates were transferred through air to the MBE system. In the preparation chamber (~1×10^{-9} mbar) the template is outgassed at 300 °C for 60 minutes, and sputtered with Ar (~1×10^{-4} mbar, 2 kV, 10 mA

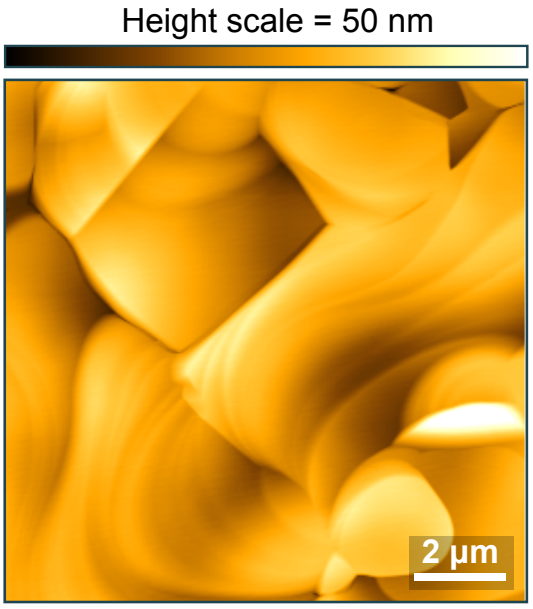

Figure 4.1: AFM image of a Ni/MgO(111) after annealing in growth chamber and before start of the h-BN growth. The topographic features of the Ni film such as step edge clusters, boundaries can be observed. Please note that due to the quick oxidation of Ni in air, the surface features (i.e. atomic steps) do not appear sharp in the image.

emission current) for 10 minutes. The annealing and Ar sputtering steps are designed for desorbing water (caused by handling of the substrate in air) and further cleaning of the surface of the Ni film. The Ni/MgO(111) substrate was subsequently transferred into the growth chamber and annealed at 850 °C for 20 minutes. An AFM image of a Ni/MgO(111) template after this annealing step is given in Figure 4.1. The annealing step in addition to the previous Ar sputtering step, helps cleaning the surface from the native oxide as well as smoothing the surface of the Ni.[39] The Ni/MgO(111) stack was subsequently cooled to the growth temperature to start the deposition of h-BN. In this chapter, we study h-BN samples synthesized at three substrate temperatures ~600 °C, 730 °C, and 835 °C over a deposition duration ranging from 10 to 300 minutes. The B and N fluxes are maintained similar to the optimized synthesis parameters used for the growth of continuous h-BN films on Ni foils (see Section 3.1 in Chapter 3 for details).

4.2 Results and Discussion

4.2.1 Growth of continuous h-BN films on Ni/MgO(111) templates

As the starting point for the growth h-BN on Ni/MgO(111) substrates, we implemented the exact same growth parameters which resulted in the growth of continuous h-BN layer on Ni foils – deposition at 730 °C substrate temperature over 300 minutes. XRR measurements and AFM profilometry verified that utilization of these growth parameters resulted in a h-BN film with an average thickness of ~3 monolayers on Ni foils (see Section 3.3 in Chapter 3). Figure 4.2 depicts AFM images of this sample. The RMS roughness of the h-BN was measured to be ~0.3 nm in 1×1 μm^2 which is an improvement to the one measured for the h-BN on Ni foils (~1 nm in 1×1 μm^2– see Figure 3.3 in Chapter 3). The

prominent height variations observed in Figure 4.2a originate from the topographic features of the underlying Ni film such as grain boundaries and step clusters. As expected, a network of wrinkles is observed in the grown h-BN film which is caused by the contraction of the underlying metal (Ni film) during sample cooling. Interestingly, these wrinkles are more abundant where the underlying Ni is more disordered (i.e. step clusters, grain boundaries), and less abundant, where a smoother Ni serves as the growth substrate. Figure 4.2b displays the topography of a smoother region, which is shown with the dashed rectangle in Figure 4.2a. At this magnification, the edge of the topmost h-BN layer can be easily distinguished. The green dashed line crosses the edge of the topmost h-BN layer and continues on the underlying h-BN layer(s). This can be verified with the step height of ~0.35 nm measured across the green dashed line, which is consistent with the thickness of one h-BN monolayer in bulk condition.[45] Please note that it is not possible to clearly define the number of grown h-BN monolayers from these AFM images as the surface is fully covered with h-BN.

It is interesting to see how h-BN crosses the atomic steps of Ni. The step height observed across the blue dashed line in Figure 4.2b is ~0.2 nm and consistent with the height of an atomic step of Ni(111).[134] However, from the (blue) height profile it is inferred that the h-BN does not necessarily follow the sharp atomic step of Ni(111), and instead, it buckles over this step. This buckling can be interpreted as an indication that the h-BN is able to (partly) release its strain (caused during the cooling, for instance) even on single atomic steps of Ni, which can be a reason why we see less wrinkles in h-BN film on smooth regions of Ni. On the other hand, a larger strain needs to be relaxed on Ni grain boundaries or on step edge clusters (i.e. caused by rotated or slightly off-axis/out-of-plane grains or step edge movements), which can be responsible for the observed network of higher (larger) wrinkles in h-BN in such regions (see Figure 4.2a). These observations propose that, using an extra-smooth surface of Ni (i.e. polished single-crystalline), combined with a slower cooling can greatly mitigate the formation of wrinkles in the h-BN film, and promote the growth of (fully epitaxial) high-quality h-BN layers using MBE. The pink dashed line in Figure 4.2b is drawn along another single step edge of Ni(111), which continues under the topmost h-BN layer. As it can be seen in Figure 4.2b, the topmost h-BN layer smooths the buckling of the bottom h-BN layer(s) on step edges. The 120° angle observed between the Ni step edges is consistent with the <110> directions on the Ni(111) terrace having a 3-fold symmetry. In Figure 4.2b, we can also see that some edges of the h-BN layers are parallel with these directions, which can be considered as a piece of evidence for the epitaxial growth of h-BN in this region. Furthermore, observation of curved edges of h-BN on Ni grain boundaries or larger step edges (an instance is shown by the black arrow in Figure 4.2b) suggest that h-BN growth front might have been hindered at the end of the (larger) step edge or other Ni surface features (i.e. grain boundaries). Please note that, here we try to gain some insight into the atomistic growth and propagation of a single atomic layer of (most likely single-crystalline) h-BN. Further study and characterization with other techniques such as in-situ low energy electron microscopy or scanning tunneling microscopy (STM) may provide a better understanding of the topic. In general, the AFM results suggest that Ni surface features are faded by the growth of h-BN over-layers and a smoother surface can be obtained by growing thicker h-BN films. Moreover, they demonstrate the significant effect of the Ni surface morphology on the quality of the MBE-grown *atomically thin* h-BN layers.

Synchrotron-based grazing incidence X-ray diffraction (GID) was used to examine the crystalline properties of the h-BN film grown on Ni/MgO(111) templates. These experi-

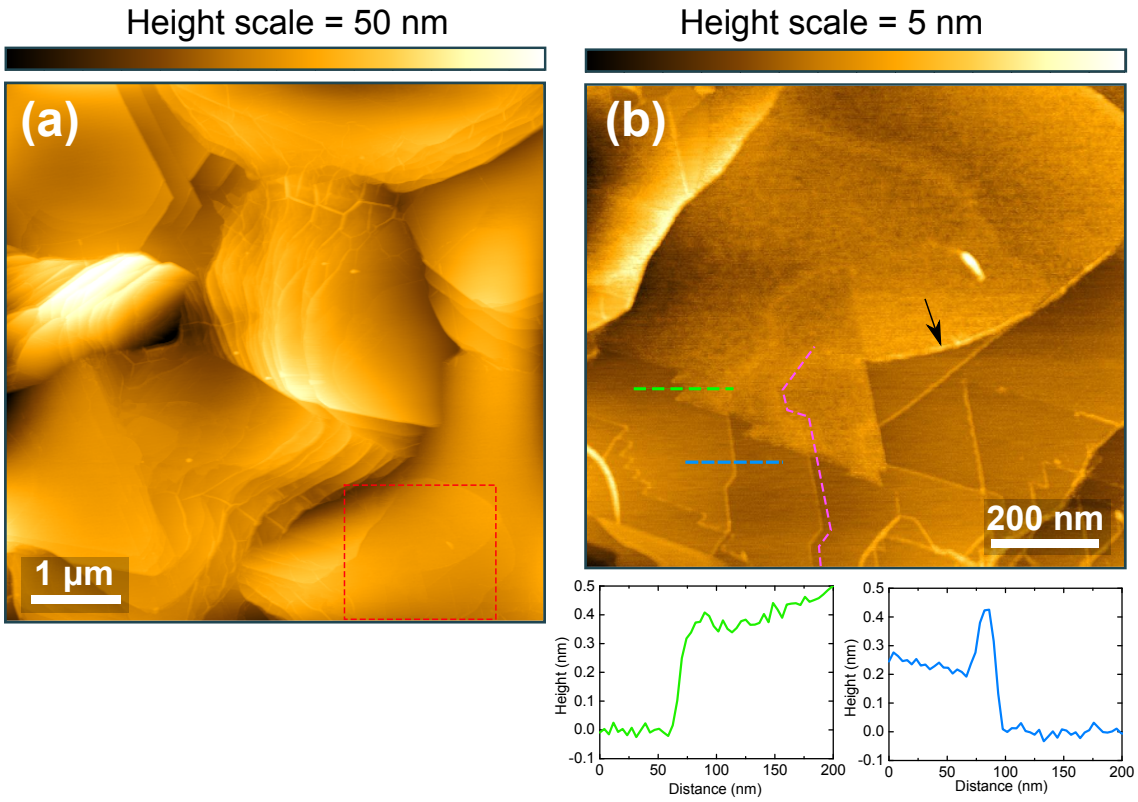

Figure 4.2: AFM scans of a continuous h-BN film grown on Ni/MgO(111) (a) Over larger areas, the topographic features of the underlying Ni film (i.e. step edge clusters, boundaries) are predominantly responsible for the height variations observed. Wrinkles in the h-BN film are are easily discernible on areas where the underlying Ni film has more disorder. (b) shows the surface topography of a smoother region shown with the dashed rectangle in (a). At this magnification, the edge of the top-most h-BN layer can be distinguished. The green dashed line crosses the border of the top-most h-BN layer. Black arrow shows a larger Ni step, on which the h-BN's growth front might have been hindered. The blue dashed line shows h-BN layer(s) crossing a Ni(111) single-atomic step edge. Height profiles along the green and blue dashed lines are given at the bottom of the AFM image (b). The pink dashed line is drawn (with some distance) along a single step edge of Ni(111).

ments were performed at beamline BM25B (SpLine) at the European Synchrotron Radiation Facility (ESRF), Grenoble, France, by collaboration with Michael Hanke and Thilo Krause from the microstructure department of Paul-Drude-Institut für Festkörperelektronik, Berlin. The X-ray energy used was 20 keV, with the beam at a 0.1° angle of incidence to ensure a high degree of surface sensitivity. In this technique, the grazing X-ray is diffracted by the lattice planes orthogonal to the sample surface normal, providing information about the in-plane lattice parameters and orientation of the surface layers. This technique has been previously used to obtain precise information about the structural configuration of single graphene layers.[135]

Figure 4.3 summarizes the results obtained from the GID measurements performed on the same sample which was used in the AFM studies previously discussed. Figure 4.3a depicts a reciprocal space map obtained from the angular and radial scans of GID measurement on this sample. The more prominent features observed in this map originate

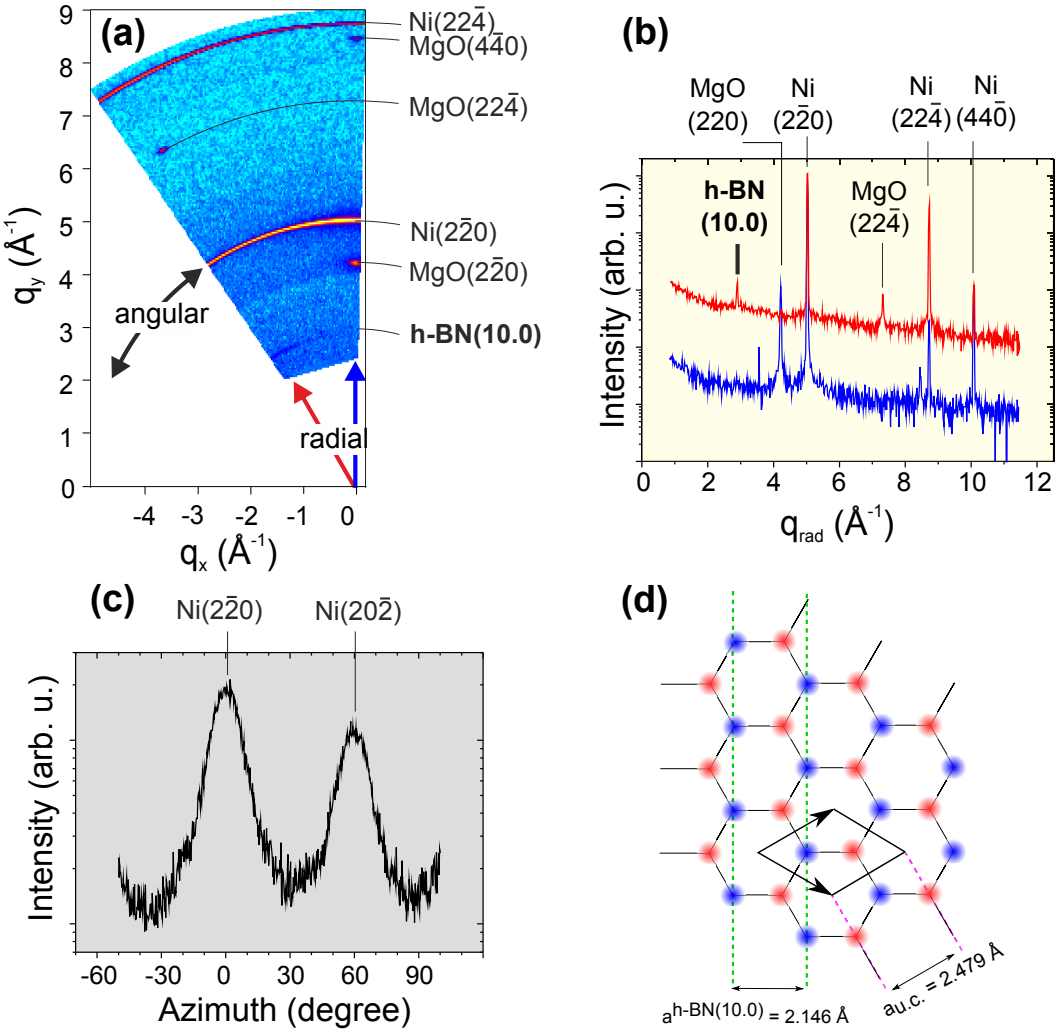

Figure 4.3: GID measurement from continuous h-BN grown on Ni/MgO(111) templates. (a) Reciprocal space map obtained from the angular and radial scans from the sample, and (b) radial scans along the <110> [blue direction in (a)] and a 30° azimuthally rotated direction [red arrow in (a)]. Contributions of different planes of MgO, Ni and h-BN in diffraction are marked in (a) and (b). (c) The azimuthal scan along the ring-like Ni diffraction [shown by the black arrow (a)]. There is a preferential alignment of Ni[110] ‖ MgO[110] which is observed from the intensity modulations of the Ni-related diffraction ring. (d) depicts a schematic of h-BN lattice. The arrows show a h-BN unit cell. The measured spacing between (10.0) planes (green dashed line) is 2.146 Å, which corresponds to a unit cell size of 2.479 Å (red dashed line) for the synthesized h-BN film.

from the single-crystalline MgO(111) substrate and the Ni, as they contribute with more volume in the diffraction. The two ring-like structures observed in Figure 4.3a originate from polycrystalline Ni which is composed of (111) oriented domains. The angular scan along the arrow in Figure 4.3a [on the more intense Ni-related ring-like contribution containing the Ni(2$\bar{2}$0)] is depicted in Figure 4.3c. The intensity modulation along the ring displays that although Ni(111) has a textured character, there is a preferred orientation of Ni(220) parallel to MgO(220). Examining two radial scans – one along the <110> direction (Figure 4.3b, blue) and one rotated azimuthally by 30° (red) – allows the compara-

tively weak h-BN reflections to be resolved. The h-BN peak shows a stronger structural correlation with the Ni surface on the 30° rotated scan. The diffraction peak at 2.927 $Å^{-1}$ results from the (10.0) reflection of the h-BN lattice, and corresponds to an in-plane lattice spacing of 2.146 Å, which translates to a h-BN unit cell size of 2.479 Å (see Figure 4.3d). The measured lattice parameter obtained here is slightly smaller compared to the one previously reported for bulk h-BN ($a_{u.c.}$ = 2.504 Å),[46] showing that the synthesized h-BN is ~1% compressively strained. As previously also discussed, the compressive strain is expected during the cooling of the sample from growth temperatures (730 °C here) to room temperature, because of the relatively large positive thermal expansion coefficient of Ni (~13–20×10^{-6} K^{-1} in temperatures ranging from 300 K to 1000 K),[125] and the negative one of h-BN (~ -2.9×10^{-6} K^{-1} to zero in the 300–1000 K temperature range).[44] These results suggest that formation of wrinkles and buckling can only *partially* relax the strain in the h-BN film. This observation can be evidence of a non-zero interaction between Ni and h-BN, responsible for the pinning of the two materials at their interface and subsequently affecting the h-BN's lattice parameter by the Ni lattice contraction upon cooling. This is in agreement with several previous studies reporting on the strong interaction between h-BN and Ni.[136–139] The interactions between h-BN and Ni will be further discussed in more details in Chapter 5, and will be further complemented by XPS results (see Figure 5.7 in Chapter 5). Furthermore, the GID measurements on a h-BN/graphene/Ni/MgO(111) sample reveal that the h-BN grown in the heterostructure (not in contact with the Ni) is strain-free, while the graphene in contact with the Ni experiences compressive strain (see Figure 5.8 and its discussion in Chapter 5). It should be noted that, Ni contraction is not responsible for all the strain observed in graphene lattice in the heterostructures discussed in Chapter 5. The reader is referred to the corresponding discussion in Chapter 5 for more details.

4.2.2 Growth of h-BN films at low temperatures

In this section, the influence of the substrate temperature on the growth of h-BN will be presented. However, the Ni/MgO(111) templates introduce limitations, which also need to be considered for the temperature studies presented here; heating the sample to very high temperatures (> 850 °C) or even keeping the sample at elevated temperatures (~835 °C) for a long time adversely influenced the Ni film continuity. This is mainly because of the ~16% lattice mismatch between the MgO(111) and the Ni(111) lattice, which means that, there is an accurate thermal budget, which leads to a desired compromise between the Ni crystalline quality, continuity and formation of twins in the Ni film.[133] For instance, if the films are kept for 30 minutes (instead of 20) at 850 °C during the annealing step in the growth chamber, the Ni film starts dewetting on the MgO(111) to release the strain caused by the lattice mismatch. The dewetting process begins with formation of some pits in the Ni film (pits are even observed in Ni films treated for 20 minutes at 850 °C in annealing step, however with less density), continues with an increase of their density and size, and finally to the formation of isolated 3-dimensional (3D) Ni islands on MgO(111), if the temperature treatment becomes too long. Therefore, the growth of samples using the substrate temperatures higher than 850 °C and the growth experiments with a duration more than 180 minutes at 835 °C were not possible. The dewetting process of Ni film on MgO(111) did not occur when lower temperatures are used for the growth. For instance, Ni films kept at 730 °C for ~600 minutes maintained their continuity, although some pits have been formed in the film. Using a bulk Ni single-crystal as

the growth substrate may also help avoiding these limitations.

Following, results obtained from a growth experiment at a substrate temperature ~600 °C over 300 minutes are presented. All the substrate preparation and growth parameters [B and N fluxes] of the optimized growth (discussed in Section 4.2.1) were maintained for this sample. The substrate temperature lies below the range which could be directly measured by the pyrometer and thus, was estimated by a combination of the temperature recorded from a thermocouple positioned about ~1 cm behind the sample in MBE manipulator (~640 °C) and extrapolation of (higher) temperatures directly measured by the pyrometer. Figure 4.4 presents AFM images obtained for this sample. Similar to previous samples, Ni topographic features dominate the most apparent height variations observed in larger scans from the sample (Figure 4.4a and b). Interestingly, unlike AFM scans of the sample grown at 730 °C (the standard continuous h-BN with optimized parameters discussed in Section 4.2.1), height scans of this sample do not show formation of long and straight wrinkles. This phenomenon may be explained by two effects originating from the lower growth temperature utilized here. The first one, which appears to be more likely and rather trivial, is the smaller thermally induced compressive strain in the h-BN lattice. In other words, Ni exhibits smaller contraction once cooled down from ~600 °C to room temperature as compared to 730 °C. Therefore, it enforces less compressive strain in the h-BN film. This explanation includes the presumption that there is an interaction between the h-BN and Ni (binding at their interface). In order to confirm this assumption for the growth at such low temperatures, further experimental efforts (i.e. XPS analysis) are necessary, although strong h-BN–Ni interaction is suggested in literature.[136,140] The second possible explanation can be the (partial) relaxation of the strain by small corrugations at grain boundaries of h-BN crystallites which could not be observed by AFM.

AFM scans of smaller areas suggest that the h-BN grown with these parameters is composed of small crystallites with very rough edges. The shape and the size of the crystallites and also the fact that they did not perfectly coalesce, although being extremely close, strongly suggest the growth occurred in the kinetically controlled regime, where ad-atoms have limited surface diffusion length before they attach to the crystal edge. Please also note that the ad-atom diffusion is considerably shorter on top of dielectrics as compared to the metal,[141] which means the shape and/or the size of crystallites might be different for the first h-BN layer forming on top of the metal surface than those of subsequent h-BN layers forming on top of the first layer. Figure 4.4c and d also display nanometer-sized particles, which are homogeneously spread all over the surface. Bresnehan et al.[141] have also reported the formation of similar 3D particles which are evenly spread on their CVD-grown h-BN on Cu foils. Their plane-view TEM investigations reveal that the 3D features are "onion-like" or fullerene-like h-BN nanoparticles having their planes perpendicular to the surface of the 2D h-BN film. According to their study, the nucleation rate of such particles increases exponentially with h-BN layer thickness, suggesting that such features nucleate at defects and leading to degradation of crystalline quality with increased thickness. We speculate that the particles observed in the AFM images have a similar origin. Finally, the step edge clusters of Ni in Figure 4.4a and b do not look as smooth as the ones in Figure 4.2, but rather rough and jagged. Considering the fact that these step edges are covered with h-BN, the observed roughness can also be related to the crystalline quality of the h-BN covering them; the former (Figure 4.4a and b) is covered with h-BN small crystallites having rough edges which is also consistent with the decreased ad-atom diffusion length due to the lower growth temperature, while the latter (see Figure 4.2) is covered with a h-BN film having larger domain size and smooth

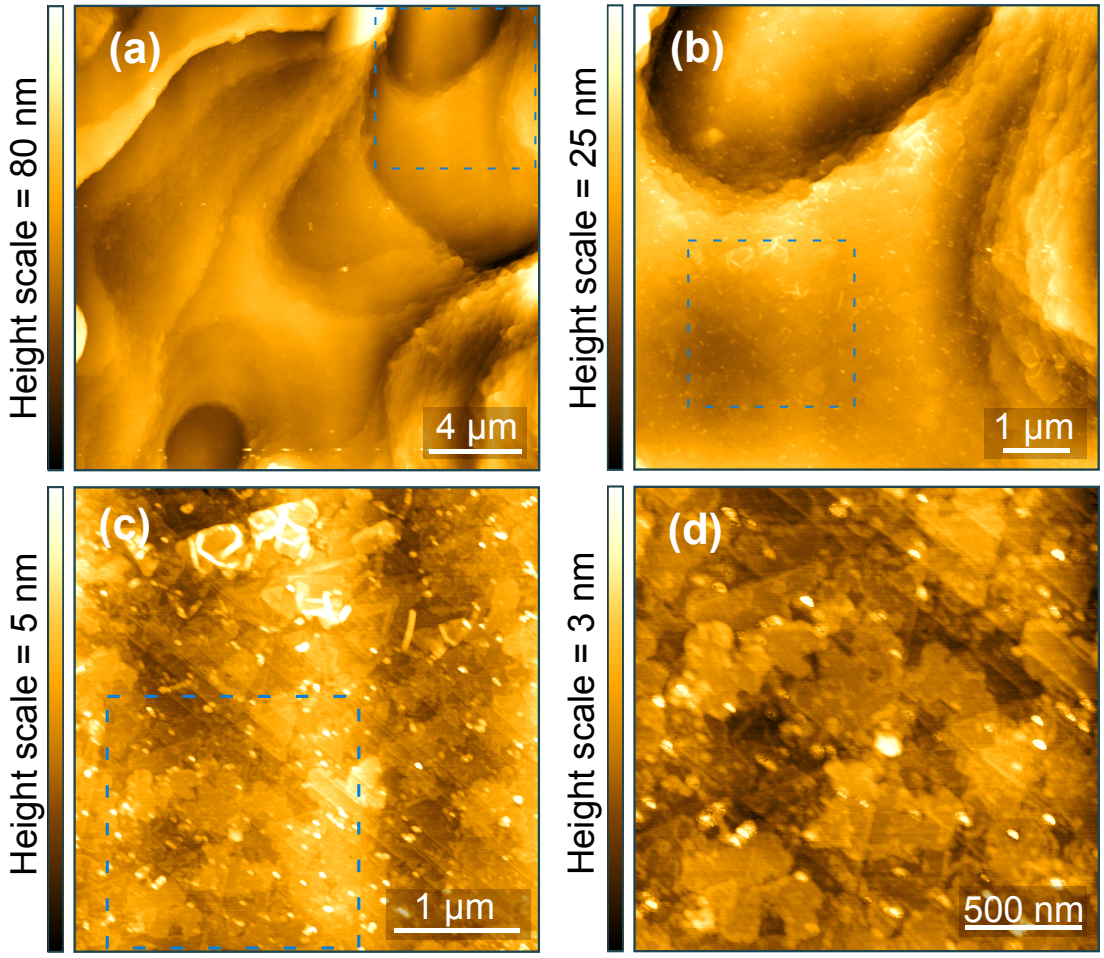

Figure 4.4: [AFM of h-BN grown at ~600 °C over 300 minutes. (a) The Ni features are predominantly observed in larger magnifications. (b-d) show higher magnification scans of the areas demonstrated by dashed squares in (a-c), respectively. The small and round protrusions on the surface in (b) and (c) are speculated to be nano BN particles.

edges.

Raman spectroscopy was additionally used to characterize the h-BN film grown at low temperature (growth at ~600 °C over 300 minutes). Figure 4.5 presents a Raman spectrum (red) obtained from this sample. For comparison, a Raman spectrum from a continuous h-BN grown at 730 °C over 300 minutes is also presented (black). Please note that the Ni-related background spectrum is not subtracted for the spectra given in Figure 4.5, and both spectra were obtained using the similar Raman acquisition parameters over long time to minimize the noise. The peak located at ~1365 cm^{-1} in both spectra is related to the E_{2g} optical phonon of h-BN.[124] As it can be easily observed in the spectra, the h-BN sample grown at 730 °C shows a sharp contribution at ~1365 cm^{-1} with a full width at half maximum (FWHM) of ~9.3 cm^{-1}, whereas the contribution of h-BN grown at ~600 °C is smaller and rather wider (FWHM = ~17 cm^{-1}). While the origin of lower intensity of this peak (for the low temperature sample) is not completely clear, the widening of the peak may be correlated to the degradation of crystalline quality upon growth at low temperatures. Wang et al.[74,142] reported on the complete disappearance of the h-BN's charac-

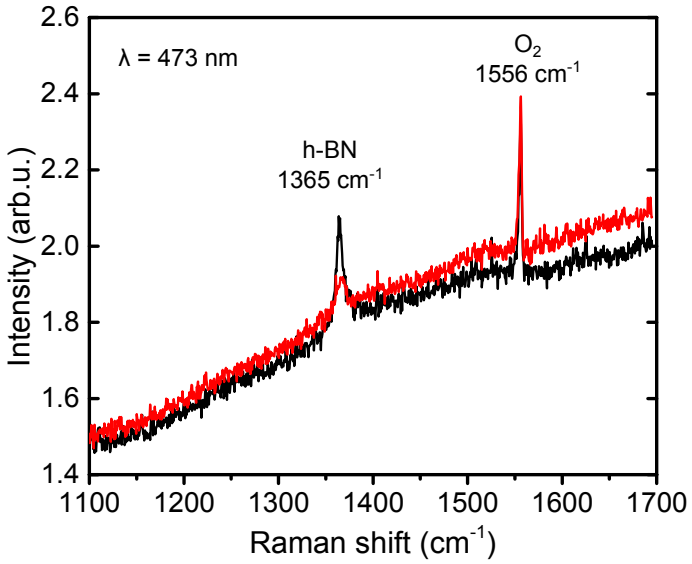

Figure 4.5: Raman spectra measured from h-BN film grown at ~600 °C (red) and 730 °C (black) over 300 minutes. In order to show the low intensity of the h-BN's characteristic peak, the as-measured spectra without Ni-related background subtraction are presented. The peak observed at ~1556 cm^{-1} is originated from oxygen molecules in air.

teristic Raman peak upon decreasing the growth temperature from 1050 °C to 600 °C for their h-BN grown on Cu [74] and Ni [142] foils using ion beam sputtering. They suggest that the formation of an amorphous BN phase as an explanation for the disappearance of h-BN's Raman peak. Same explanation can also hold true for the weaker and wider Raman signal observed from the sample grown at lower temperatures. However, as can be seen in Figure 4.5, the Raman spectrum obtained from the sample grown at ~600 °C clearly shows a contribution at ~1365 cm^{-1}, although being weak. Considering their suggestion, the weak Raman signal may be explained as following: 1) The sample contains a mixed crystalline and amorphous phase (within the laser spot size), which implies that this sample has a lower degree of crystallinity as compared to the one grown at 730 °C, or 2) the sample is composed of a crystalline phase (which is most likely in contact with Ni) and amorphous (or with lower degree of crystallinity) over-layers, which don't contribute to the Raman E_{2g} mode of h-BN. The second explanation appears to be more likely. As it will be shown later, evidence of the epitaxial growth was observed for samples grown at ~600 °C with partial coverage (see Subsection 4.2.4). The small FWHM of the h-BN's characteristic peak of the sample grown at 730 °C is comparable to the one measured for exfoliated single-crystals of h-BN (9–12 cm^{-1}), [127] and consistent with its high structural quality, while the larger FWHM of the sample grown at lower temperatures is generally considered as a degradation in structural quality. [143] Raman spectroscopy measurements do not show evidence for the formation of cubic boron nitride in these samples (i.e. Raman signal at ~1305 cm^{-1}). [124] Finally, the peak observed at ~1556 cm^{-1} (FWHM = 2.9 cm^{-1}) corresponds to the vibrational mode of O_2 in the air. [144,145]

4.2.3 The influence of the growth duration

In this section, the growth behavior of h-BN at different stages of the growth will be studied. For the samples introduced here, we kept all the Ni film preparation and h-

BN growth parameters similar to the optimized parameters (substrate temperature of 730 °C and same B and N fluxes) which was employed to obtain continuous films (see Section 4.2.1). The growth duration was varied between 10 and 60 minutes. The samples were then ex-situ studied by SEM as well as AFM by employing height and phase contrast modes.

Please note that the contrast which is related to h-BN in SEM images depends on various parameters. Thickness and coverage of h-BN, SEM imaging conditions (i.e. primary electron beam energy and current, working distance and the detector being used), charging effects, and the yield of producing different types of secondary electrons influence the contrast generated by each detector.

The SEM contrasts observed for low dimensional materials and the corresponding explanation has been the topic of several studies.[109,127,132,146] In this work, we have observed both positive and negative (inverse) contrasts for the h-BN on Ni. In other words, h-BN appears dark in imaging from some samples, while it looks brighter in images from other samples (with different coverage and growth parameters). Drawing a universal explanation for the changes in SEM contrast would lie out of the scope of this thesis, and requires further systematic investigations using standard samples with precise knowledge about their thickness. In this Chapter, it is tried to provide necessary information to understand each image individually.

The first important information obtained from the time series is the onset of growth, which can inform about the nucleation behavior of h-BN on Ni films. We could not observe any evidence of the h-BN formation in the growth experiment at 730 °C over 10 minutes. Therefore, the growth duration was increased to 30 minutes to study the first sample. Figure 4.6 depicts SEM images from this sample. In images (a-c) which are acquired by the In-Lens detector, the darker contrast indicates h-BN islands.[a]

In relatively low magnifications such as the one presented in Figure 4.6a, it can be seen that the h-BN islands are randomly nucleated and rather unevenly distributed on the Ni surface, which suggests that there are certain surface features promoting the nucleation. In particular, pits in the Ni film serve as nucleation centers for h-BN, as can be observed from the bright contrast in the middle of some of the islands presented in Figure 4.6a and b. However, we can see that nucleation does not necessarily happen only on Ni pits (Figure 4.6b and c); other surface features (i.e. Ni grain boundaries, protrusions), where the substrate has higher surface energy can also act as preferential nucleation site for h-BN islands. Interestingly, the islands nucleated on Ni pits are typically larger than the other ones, suggesting that they nucleated at an earlier stage of the growth.

The h-BN islands have random shapes and typically contain straight edges (e.g. Fig-

[a] The dark contrast observed for the regions covered by the h-BN in Figure 4.6a-c (recorded with In-Lens detector) can be due to the attenuation of the low-energy surface secondary electrons (SE1) by the h-BN layer, when leaving the Ni substrate.[146] The bare Ni also shows slight contrast variations, which are speculated to be related to the SE1 generation yield and the penetration depth of the primary electron beam into various crystalline orientations of the Ni grains. This contrast variation which is also observed in the h-BN covered regions, is referred to as channeling contrast.[72] Unlike the In-Lens detector, the conventional Everhart-Thornley (ET) detector did not provide useful contrast variations to image h-BN islands. For comparison, two micrographs which were recorded simultaneously with the In-Lens and ET detectors are presented in Figures 4.6c and d, respectively. As it was previously explained in Section 2.3 in Chapter 2, The In-Lens detector favors the SE1 electrons which have the direct information about the surface, while the contrast produced by the ET detector is obtained from a mix of electrons (namely SE1, SE2, SE3 and backscattered electrons). Thus, it is less efficient than the In-Lens detector for imaging thin layers. However, due to the position of ET detector in SEM system, it offers better topographic images of the surface. For more details see Section 2.3

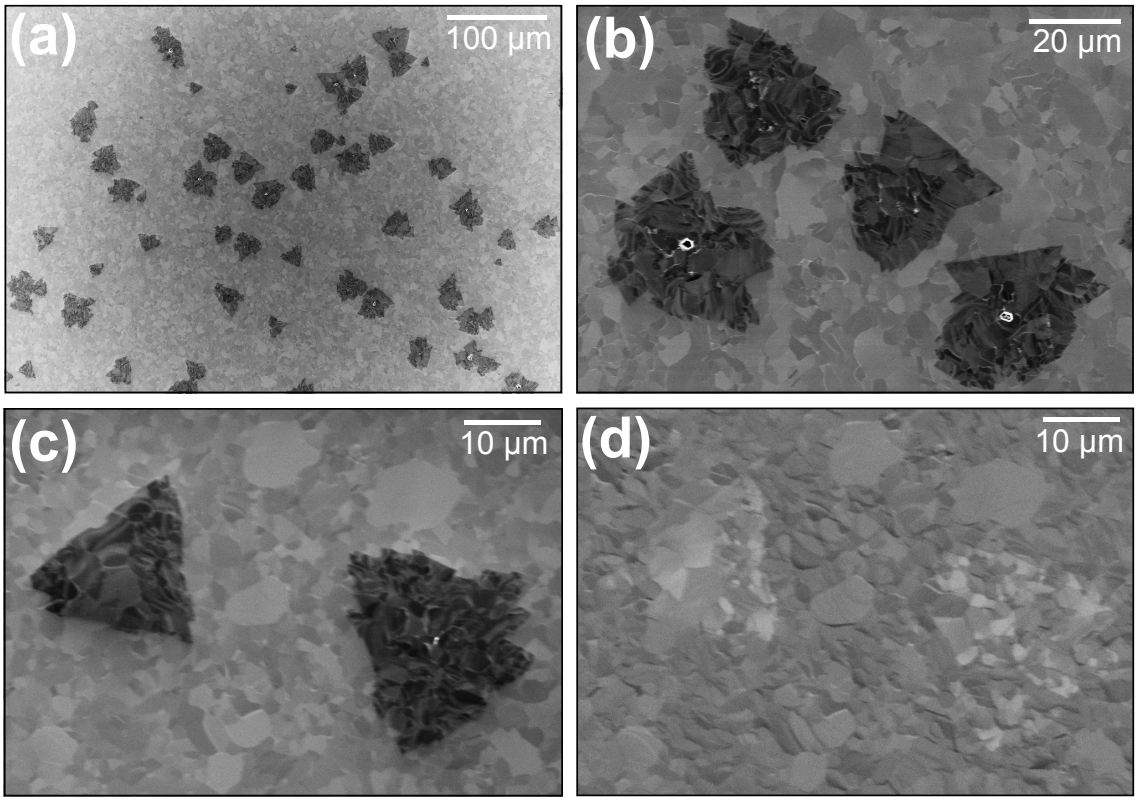

Figure 4.6: SEM of h-BN islands grown at 730 °C over 30 minutes. (a-c) show images obtained from the In-Lens detector of SEM. The dark contrast in (a-c) shows the h-BN islands. Pits in the Ni film act as nucleation sites for h-BN (a,b), however, not all the nucleation sites are pits in Ni (b,c). The h-BN islands have typically smooth edges which are spread over several Ni grains. (d) shows the image captured with the conventional secondary electron detector, the ET detector, from the exact same area of (c). Due to the position of the ET detector, it is more sensitive to the surface topography as compared to the In-Lens detector.

ure 4.6c). This suggest that the observed shapes are not a result of dendritic growth, but rather formed due to the coalescence of rotated crystallites which were nucleated on the same or very closely located nucleation centers. Moreover, the images suggest that, although h-BN can propagate on different grains of Ni (for instance see contrast variations withing h-BN covered regions in Figure 4.6c), it is yet influenced by the surface morphology of the substrate.

Performing the growth experiment over 60 minutes, while keeping all other preparation and growth parameters as before, led to the formation of h-BN with a much higher coverage. Wrinkles have been frequently observed in several AFM scans from this sample, suggesting that a continuous h-BN film has been formed. Simultaneously obtained AFM height and phase images are used for studying this sample. More information about AFM phase imaging can be found in Chapter 2. Literature also contains examples showing the efficiency of AFM phase imaging in providing additional information such as graphene coverage of SiC surfaces.[147,148].

Figure 4.7 depicts AFM height and phase images obtained from this sample. As previously explained, observation of wrinkles (e.g. pink arrow in Figure 4.7a) verify the presence of h-BN on the scanned area. A direct comparison of the height and phase im-

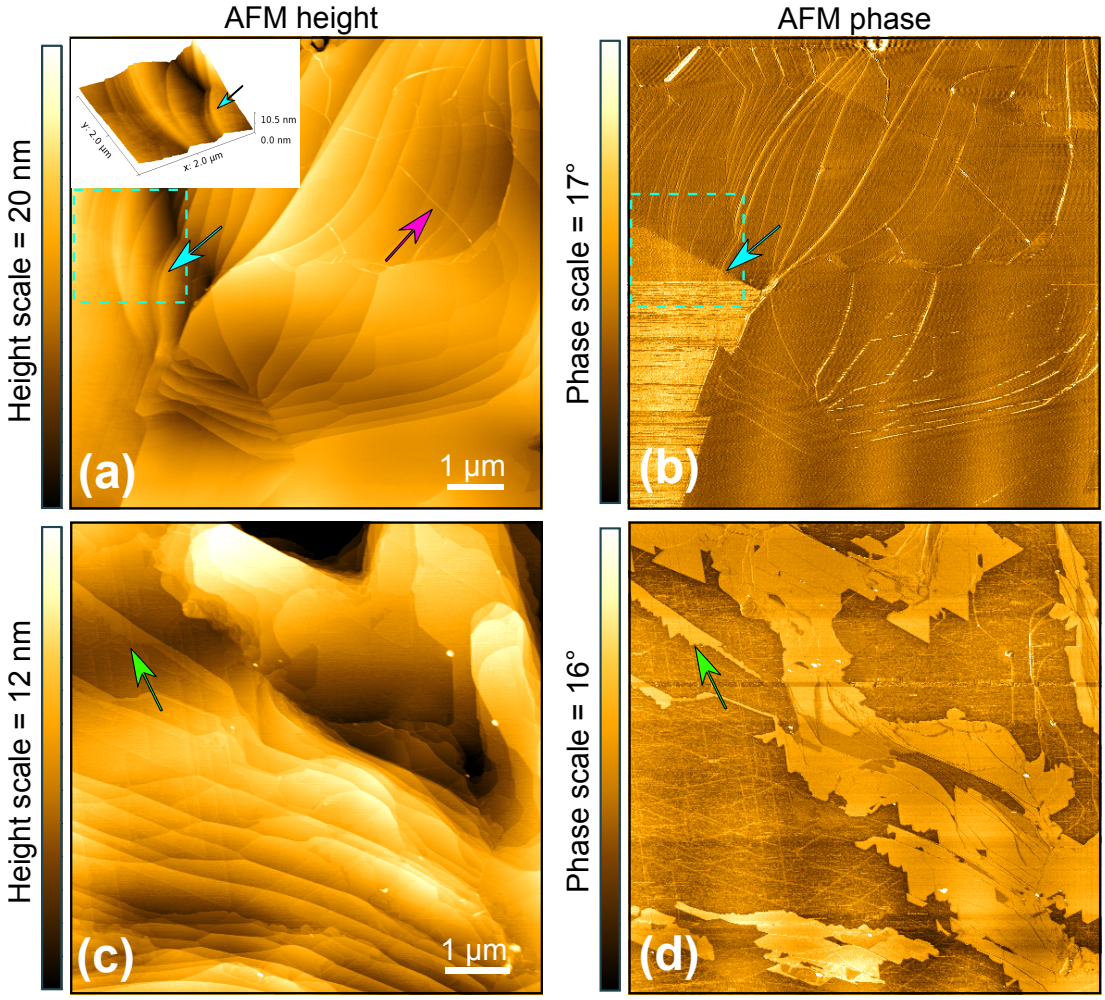

Figure 4.7: AFM images of a h-BN grown at 730 °C over 60 minutes on Ni film. (a) shows the AFM height scan and (b) the simultaneously obtained phase scan of a region containing large Ni terraces. The pink arrow shows a wrinkle in h-BN film. The region with higher phase contrast in (b) is speculated to be composed of thicker h-BN. The cyan arrows in (a) and (b) show the border of a thicker h-BN layer. The inset shows a 3D view of this border, where h-BN fades the Ni surface features. Similarly, (c) and (d) show height and phase scans of another area of the sample. The high phase contrast in (d) shows thicker h-BN in (c). The green arrows show one such region

ages provided in Figure 4.7a and b, reveals that the sudden height changes such as Ni steps and wrinkles in the h-BN cause a very *local* phase shift (e.g. the wrinkle shown by the pink arrow in Figure 4.7a and b). This has been previously observed for the step edges of SiC and wrinkles in graphene covering SiC surfaces.[147,149] The phase stays (almost) the same at both sides of the wrinkle or step edge suggesting that both sides of the wrinkle or step edge are covered with a similar material, in this case h-BN. To summarize, by now it is clear that regions having low phase-contrast in Figure 4.7b are fully covered with h-BN.

A portion of the imaged area shows a *permanent* phase shift compared to the rest of the image, such as what is observed at the bottom left corner of Figure 4.7a (higher phase-contrast). A meticulous examination using AFM height profiles and the observed topog-

raphy, confirms that those regions are covered with a thicker h-BN. For instance, the area shown by cyan dashed squares in Figure 4.7a and b, includes the border of such region (shown by cyan arrows). Besides a height difference of ~0.3 nm, we can see that the Ni topographic features (here step clusters) are faded where a thicker h-BN is present. A 3D view of the topography in the area shown by cyan dashes is given in the inset of Figure 4.7a. The fading of the step edges can also be verified in the phase image, where the the step edges of underlying Ni do not cause a pronounced *local* phase shift (see the dashed square in Figure 4.2b). Please note that, the fading of Ni surface features by thicker h-BN film has already been discussed previously in this chapter for the image shown Figure 4.2b. To summarize, by now it is clear that h-BN is present all over the imaged area given in Figure 4.7a and b, and that the thicker h-BN showed a permanent higher phase-contrast.

Similarly, in Figure 4.7d we see regions with higher phase contrast, and by checking the height image given in Figure 4.7c, it can be concluded that the higher phase contrast in this image corresponds to thicker h-BN layers. One such region is shown by green arrows in Figure 4.7c and d. A comparison of phase and height images depicted in Figure 4.7c and d, shows that the thicker h-BN regions are formed along the rougher parts of the surface such as Ni step clusters. This is also confirmed by SEM images obtained from this sample which will be discussed later.

It is worth noting that, we could only qualitatively use the AFM phase images. The phase-contrast may offer *hints* and could only be used together with the height images. In general, a clear correlation between the number of probed h-BN layers and the amount or the sign of the phase shifts could not be found.

Figure 4.8 shows SEM images obtained from the sample discussed above (grown over 60 minutes at 730 °C), which were acquired with the In-Lens and ET detectors. As previously discussed, the surface is covered with a continuous h-BN film with thickness inhomogeneities. Unlike the samples with partial h-BN coverage (e.g. presented in Figure 4.6a-c), the bright contrast in the image acquired with the In-Lens detector (Figure 4.8a) is related to regions covered with thicker h-BN.[b] A direct comparison of these two images suggest that the Ni surface imperfections (i.e. step clusters, grain boundaries) are preferential regions to observe a thicker h-BN, which corroborate the AFM results.

It is worth studying this sample around a region, where the underlying Ni film was scratched by the tip of a tweezer prior to the growth. As we observed in the beginning of

[b] As it was previously discussed, SEM In-Lens detector gives darker contrast for h-BN in partial coverages, probably due to an attenuation of SE1 electrons by h-BN (see previous footnote in same Section). The contrast observed from samples with full h-BN coverage was different, however. Studying the SEM images from h-BN samples with complete coverage suggests that, regions with thicker h-BN are brighter than the areas covered with thinner h-BN. This observation for the *fully covered h-BN regions* is consistent with a previous study,[132] claiming that the secondary electron intensity is proportional to the number of probed h-BN layers, over a large range of thicknesses (verified up to 10 monolayers). According to Sutter et al.,[132] except for the first h-BN layer grown on Ru(0001) [which produces a small *increase* in contrast due to the h-BN/Ru(0001) interaction[71]], the over-layers cause a distinct larger (and constant) contrast increase in SEM imaging. It is suggested to be the result of secondary electrons primarily originating from the "bulk-like" h-BN.

It is worth noting that the images acquired with ET and In-Lens detectors can demonstrate inverse contrasts, even when simultaneously employed to record images of a sample. Clear examples are given in Figure 4.9. The h-BN covered regions in those images appear darker in In-Lens images and brighter in ET images. This might be correlated to the different type of secondary electrons used for image construction by the two detectors. However, other factors such as charging effects[146] can also cause contrast inversion.

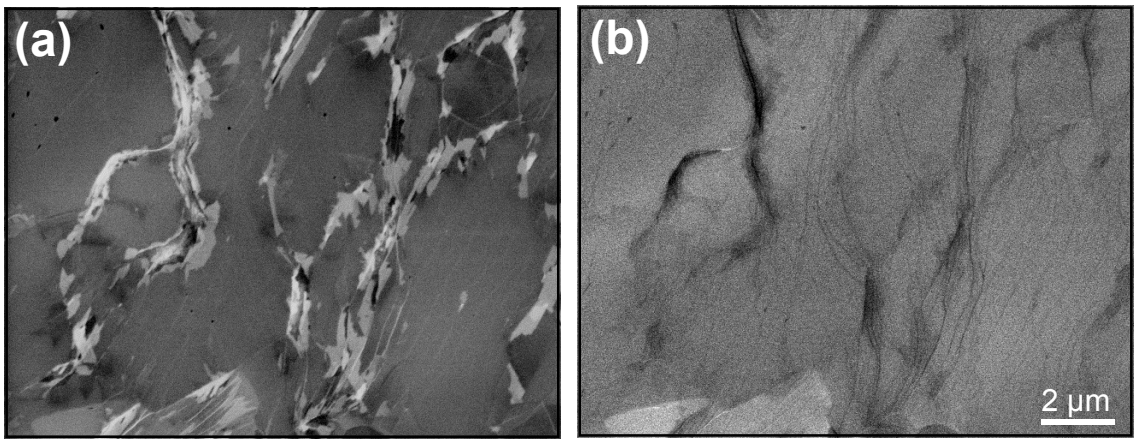

Figure 4.8: SEM of h-BN grown at 730 °C over 60 minutes. The images are simultaneously obtained from (a) In-Lens and (b) ET detector. H-BN covers the entire surface of this sample. The brighter contrast in (a) is related to a thicker h-BN. The topography of Ni is better observed in (b). Thicker h-BN is typically formed on rougher features of Ni surface.

this section for the sample grown over 30 minutes at 730 °C , the pits in the Ni film were preferred nucleation sites for h-BN. Considering the high surface diffusion length of ad-atoms at high temperatures, and the surface energy of the pits (their roughness and sharp edges), these pits can act as wells which trap and deplete the surface from diffusive B ad-atoms before they chemically bond to N ad-atoms and agglomerate to form h-BN islands. With this scenario, it is expected that these holes are regions with a more concentration of B ad-atoms, where h-BN nucleation starts. Here, an artificial roughness (scratch) on the Ni template may be considered as a series of pits connected together.

Figure 4.9 shows the SEM images of the scratched area after the growth of h-BN for 60 minutes. In the micrograph obtained by the In-Lens detector, the dark contrast shows the h-BN coverage, while the ET detector shows the h-BN brighter than the environment. For a better demonstration, the contrast of the image of the ET detector is enhanced by software. The top-right and bottom-left portion of the Figure 4.9a show the border of the continuous h-BN film. Higher magnification images from the scratched area and the border of the continuous h-BN film are presented in Figure 4.9b and c, respectively.

Figure 4.9a shows that the scratch offers preferential nucleation sites for h-BN, likely because of the similar reason explained for the pits as nucleation site. Interestingly, we see that the border of the continuous h-BN film (top-right of Figure 4.9a) is parallel to the main scratched line. There is a distance of 200–250 µm between them, which is not covered by a continuous h-BN film , but rather discrete nucleations. With a very rough estimation and neglecting the h-BN islands formed in this region, this distance suggests that the diffusion length of B ad-atoms is at least in the order of ~100 µm. In other words, it may be assumed that atoms adsorbed in the middle of this depleted region, migrate a length of at least ~100 µm either to reach the edge of the h-BN covered area or to the scratch. Similar way of ad-atom migration length estimation has been used in a previous study.[150] Please note, here the N atoms are assumed to exist in excessive amount all over the surface and only the diffusion of B ad-atoms are considered in this estimation. This high diffusion length of ad-atoms suggest that the growth is not kinetically limited, and thus h-BN films with larger grains can be produced by utilizing these growth parameters.

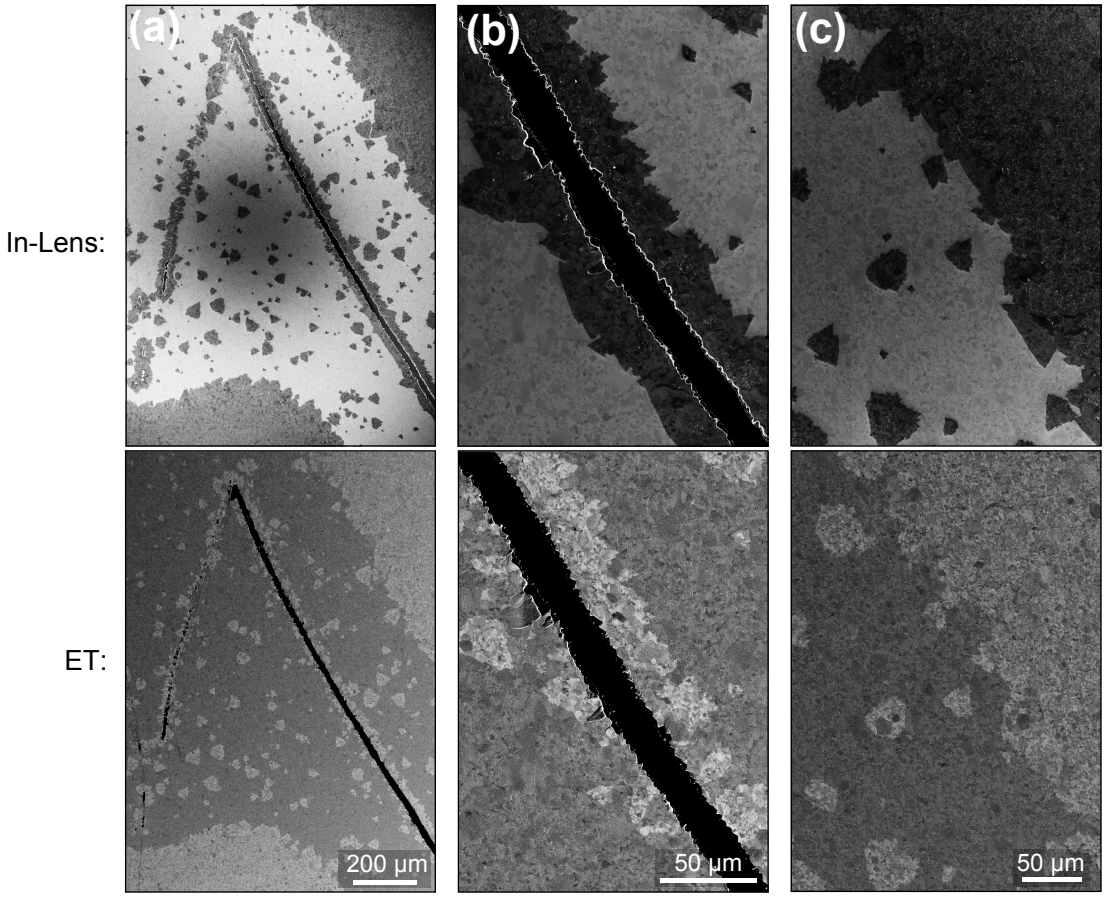

Figure 4.9: SEM images of a h-BN grown at 730 °C over 60 minutes close to a scratch on the Ni film. (a) and (b) show low and high magnification around the scratched Ni film, and (c) shows the border where the continuous h-BN starts. The images obtained from the ET detector are also provided for comparison.

This might be realized by reducing the nucleation density through the use of Ni templates with higher surface quality (i.e. single-crystal or larger crystalline Ni domains, reduced roughness).

The influence of the surface roughness on the nucleation and growth of h-BN has been the subject of few studies.[151,152] For instance, Tay et al.[151] claim a decrease in h-BN nucleation density by a factor of 3 and a transition from triangular to hexagonal nucleus shape (island shape) upon electrochemical polishing the Cu foils. Xu et al.[152] reports on larger domain sizes and more uniform thickness for their MBE-grown h-BN on polished cobalt foils.

4.2.4 Temperature dependence of nucleation and growth

In previous Subsection 4.2.3, the nucleation and growth behavior of h-BN samples synthesized at 730 °C over 30 minutes and 60 minutes were shown, and possible explanations based on growth kinetics were presented. In this Subsection, a study of h-BN samples grown at higher and lower temperatures than 730 °C is presented. For this, in order to find the onset of the growth, initially two samples were grown at ~600 °C and 835 °C over 30 minutes. All other Ni film preparation parameters, as well as B and N

fluxes were kept as before. Finally, this study will be complemented by the growth of two other samples: one grown at 730 °C over 10 minutes, and the other one at 835 °C over 60 minutes.

Figure 4.10 presents SEM images obtained from a h-BN sample grown at ~600 °C for 30 minutes. In these images, h-BN covered surfaces appear brighter than Ni. Figures 4.10b and c show corresponding simultaneously obtained images using ET and In-Lens detectors, respectively. As it is observed in Figure 4.10b, h-BN covers a hight portion of the surface. Please note that the h-BN coverage in Figure 4.10c might be misinterpreted, because of a contrast enhancement by software which was performed for a better demonstration of h-BN growth front. In other words, h-BN is present on all Ni grains of these images, although it might not be quite clear, due to image size and contrast enhancement. A magnified view of the region shown by red dashed rectangle in Figure 4.10b is given in Figure 4.10d.

A comparison between these images (Figure 4.10) and the ones presented for the growth of h-BN at 730 °C with the same duration of 30 minutes (given in Figure 4.6), sheds light on several temperature dependent aspects of h-BN growth. For instance, unlike the h-BN grown at 730 °C, holes in the Ni film are not necessarily the preferred nucleation sites for h-BN grown at ~600 °C (compare Figure 4.6a to Figure 4.10a). The images in Figure 4.10b-d clearly show that other Ni surface features, in particular step edges, promote the nucleation and growth of h-BN at ~600 °C. This evidence indicates the dramatic reduction of ad-atom diffusion length at lower growth temperatures. Moreover, unlike the growth at 730 °C where h-BN domains expand over several Ni grains (see Figures 4.6b and c), here we see no h-BN domain crossing Ni grain boundaries, which further supports the claim for reduced ad-atom diffusion length observed in this growth experiment. Additionally, it is observed that the h-BN coverage is much higher at ~600 °C as compared to 730 °C for the same growth duration (30 min). This reveals the larger sticking coefficients of B and N atoms (or their lower rate of desorption from substrate before incorporating into h-BN crystal lattice) at ~600 °C, considering the unchanged impingement rate of the constituents (fixed B and N fluxes) used here. It is worth noting that, discussions about the sticking coefficient and desorption of atoms for MBE growth of 2D materials have some precedent in literature. For instance, Dabrowski et al.[153] have tried to quantify the high desorption of C and C clusters from h-BN surfaces for MBE-grown graphene. Also, the dependency of sticking coefficient on temperature as well as on different growth substrates have been used to explain the behavior of growth and nucleation using MBE.[42,154,155] Besides the higher coverage obtained at ~600 °C, these images (given in Figure 4.10) also suggest that after the h-BN growth started at the step edge clusters of Ni, it propagates on the upper Ni terrace. A region demonstrating evidence for this growth behavior is shown by the green dashed circle Figures 4.10b, similar to what has been previously observed in Figure 4.7d (green arrow). Furthermore, the jagged shape of the h-BN growth front observed in these images strongly suggest that the h-BN coverage is locally composed of several parallel triangles, which is consistent with their epitaxial alignment with respect to the underlying Ni grains.

The Ni grain boundaries (e.g. in Figures 4.10b) typically appear brighter in SEM images, suggesting the presence of thicker h-BN in those regions.[c] Interestingly, higher magnification SEM images reveal some distinct round features, which have been formed

[c] We are aware that also charge accumulation on sharp edges leads to a bright contrast of edges. However, the bright contrast discussed here is caused mostly from closely located discrete particles, and can be better observed in images with original size.

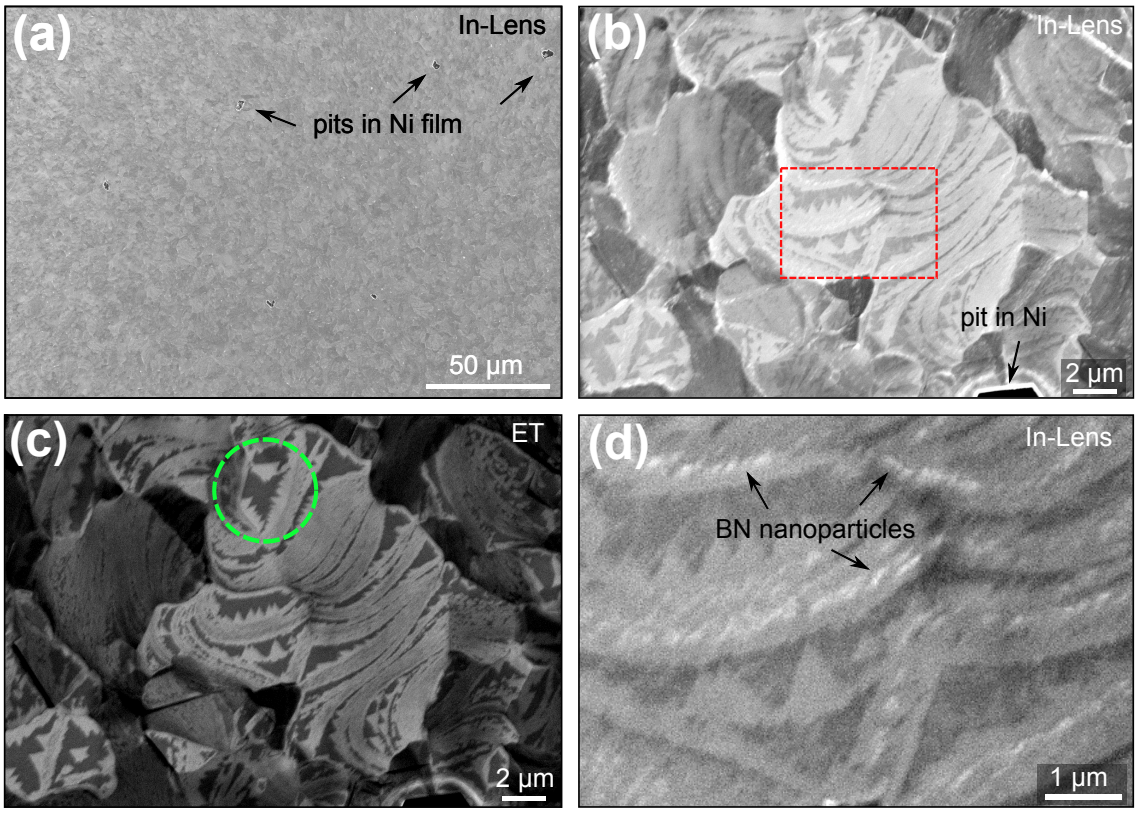

Figure 4.10: SEM of h-BN grown over 30 minutes at ~600 °C (a) A low magnification image, showing that there is no specific contrast variation denoting preferred nucleation around Ni pits. (b) and (c) are simultaneously obtained images from In-Lens and ET detector of this sample. It can be observed that the h-BN growth is initiated from step edges and propagates on the upper terrace (green dashed circle). The red dashed rectangle in (b) is presented with a higher magnification in (d). Some round features are observed on the middle of h-BN layers on Ni. These features are most likely nanoparticles of BN which are formed due to limited ad-atom diffusion length at low growth temperature

on the surface. These features are observed on the h-BN covered areas, and their density is much higher on h-BN forming on rough Ni surface, more specifically on Ni step clusters. Also, a high density of features of similar type is observed on the h-BN covered Ni grain boundaries. The small features are perhaps BN nanoparticles forming on top of the first h-BN layer. With the present information, it can be thought of two possible explanations for their formation. The first one, which appears to be more likely, considers the low diffusion length of ad-atoms on Ni surface (due to the low growth temperature), and even much lower on h-BN covered surfaces. In this scenario, at the initial state of the growth, the exposed Ni surface enhances the diffusion of ad-atoms, leading to the formation of h-BN layer (probably from step edges of Ni) and propagating on the Ni surface. Once a portion of the surface is covered with h-BN, the ad-atoms partly land on the h-BN covered areas, having very low diffusion. These ad-atoms can diffuse to reach the exposed Ni surface and take part in the growth of h-BN layer, if they are close to the edge of the h-BN covered region. However, if they are far from the h-BN layer growth front, they diffuse on the h-BN covered area until they reach a rougher region of the h-BN

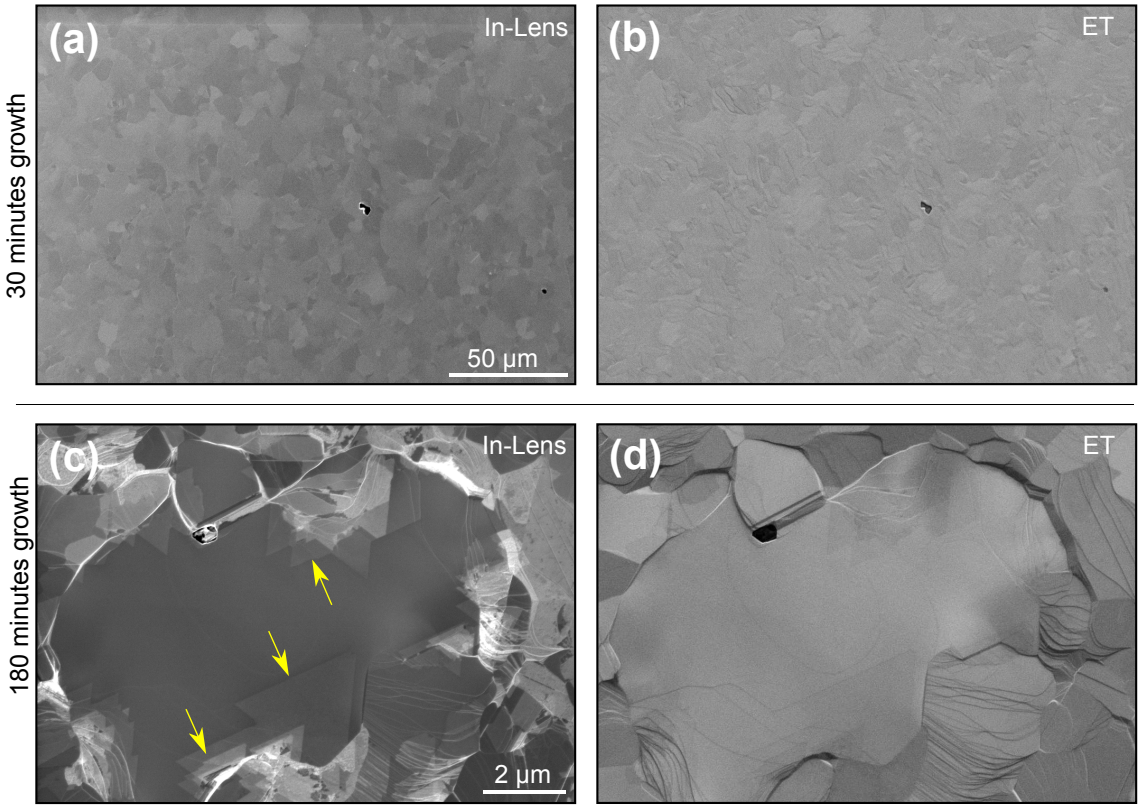

Figure 4.11: SEM of h-BN grown over 30 minutes at 835 °C (a) image obtained from the In-Lens and (b) ET detector show no evidence of h-BN formation utilizing these growth parameters. (c) and (d) show the In-Lens and ET image of h-BN grown at 835 °C over 180 minutes, respectively. Yellow arrows point out to the edges of thicker h-BN

surface such as on step clusters (covered by h-BN). Since rougher surfaces offer smaller Gibbs free energy barrier for nucleation, the ad-atoms agglomerate on these regions and form nanoparticles (or nanoclusters) of h-BN. In Figure 4.10d, it is observed that these features are typically formed in the middle of the h-BN covered regions and far from the growth front, which is consistent with the explanation given above. We speculate that the previously observed BN nanoparticles in the sample grown at ~600 °C over 300 minutes (see Figure 4.4c and d) have similar origin. The second possible explanation is that, these nanoparticles have been formed at the interface between Ni and the first h-BN layer; the B and N ad-atoms could intercalate under the h-BN through the edges of h-BN islands and diffuse to reach the Ni step edges to form the clusters. However, this second possible explanation appears less likely. The reason is that a relatively long surface diffusion should be considered for B and N ad-atoms to be able to travel from the edges of h-BN islands to the Ni step edges. Considering this high diffusion length the nucleation of well-defined triangular islands instead of round features would be expected at the h-BN/Ni interface. In order to study an earlier stage of the growth at ~600 °C, we reduced the growth duration to 10 minutes (instead of 30 minutes). However, SEM images showed no nucleation and growth for the utilized parameters (not shown).

Unlike the samples grown at ~600 °C over 30 minutes, which showed high h-BN coverage, the SEM images obtained from the sample grown at 835 °C over 30 minutes did not

show any evidence of h-BN formation. Figures 4.11a and b depict an example of a region with a hole in the Ni film, where h-BN nucleation was more probable to occur (compare with Figure 4.6b or Figures 4.10b). The weak contrast variation seen in the In-Lens image is due to different Ni grain orientations, as previously discussed. This observation is consistent with the decreased sticking efficiency of the B and N atoms to the Ni surface at higher temperatures. In order to obtain h-BN at this temperature, the growth duration was increased to 180 minutes. Figures 4.11c and d depict SEM images (simultaneously obtained by In-Lens and ET detectors) of such sample. The Ni surface is completely covered by h-BN, as verified by observation of wrinkles in the h-BN film (however, not quite visible in the small and flat area chosen here, see also Figure 4.2b) and Raman spectroscopy. The thicker h-BN appears brighter in Figure 4.11c. As expected, due to the high diffusion length of the ad-atoms, the thicker h-BN regions typically appear as triangles with smooth edges (e.g. shown by yellow arrows in Figure 4.11c). It is also clearly seen that the smooth surface of the middle Ni grain is more homogeneously covered with h-BN and the thicker h-BN regions start from the rough Ni surface features such as grain boundary or step edge clusters.

4.3 Summary and conclusions

In this chapter the growth of h-BN on Ni/MgO(111) substrates was studied. As the first step, the optimized growth parameters which resulted in the formation of atomically thin and continuous h-BN films on Ni foils were reproduced. Employing Ni/MgO(111) templates instead of Ni foils led to some improvements in the structural quality and morphology of grown h-BN films. For instance, a sharper Raman characteristic peak (a FWHM of 9.3 cm^{-1} for h-BN on Ni films vs. 10.7 cm^{-1} for h-BN on Ni foils), and a reduced RMS roughness (by a factor of ~3). The GID experiments revealed that the h-BN film grown at 730 °C over 300 minutes is ~1% compressively strained, which is most likely induced by the Ni in contact with the h-BN film during the cooling stage. Replicating this growth recipe at lower temperatures resulted in a h-BN film containing small coalesced crystallites and small round features on its surface, which are likely BN nanoparticles. The weaker and relatively wider (FWHM = ~17 cm^{-1}) Raman characteristic peak suggest a degradation in crystalline quality of the h-BN upon decreasing the growth temperature from 730 °C to ~600 °C. The growth behavior of h-BN on polycrystalline Ni surfaces using MBE is a complex interplay between B and N sticking coefficients, ad-atom diffusion and effects of the surface on nucleation mechanism. This scheme becomes even more complicated for the growth of h-BN over-layers, when the Ni surface is partly or completely covered with h-BN. Here, by systematically varying the growth temperature and duration, we were able to shed some light on the growth behavior of h-BN on Ni. For instance, while the growth over 30 minutes at 730 °C resulted in low h-BN coverage consisting of discrete islands with a size up to 25 µm in diameter, the growth at ~600 °C with same duration resulted in formation of much higher h-BN coverage, which is composed of smaller coalesced triangular islands (up to ~2 µm). The growth attempt with same duration at 835 °C did not show any h-BN formation. The higher coverage is the consequence of larger sticking coefficient of the B and N species at ~600 °C. Similarly, a decrease in sticking coefficient at high temperatures can explain why no h-BN was grown at 835 °C for the same growth duration. The ad-atom diffusion length explains the difference in island sizes, preferred nucleation sites and growth behavior of h-BN at 735 °C and ~600 °C. The islands at 730 °C typically nucleate around Ni surface features with extreme

roughness (i.e. pits in Ni film), and single h-BN domains can grow over several Ni grains. Unlike the growth at 735 °C, in the growth at ~600 °C even small changes in the surface energy, such as Ni step edge clusters, offer several nucleation sites for h-BN formation. Therefore h-BN grown at ~600 °C is composed of small triangular islands with parallel edges, which were closely nucleated and coalesced. SEM images show no evidence that these small islands expand over several Ni grains, which is in agreement with the limited ad-atom diffusion length at ~600 °C. Moreover, SEM images of samples grown at elevated temperatures (730 °C and 835 °C) show that thicker h-BN regions also have smooth and straight edges, which can be explained by the enhanced ad-atom diffusion even on h-BN surface, at these temperatures.

The results obtained in this chapter serve to demonstrate the significance of ad-atom diffusion engineering using precise control over temperature, and also the necessity of a smooth Ni surface to achieve better control over the quality and thickness homogeneity of h-BN layers grown by MBE.

5 Growth of h-BN/graphene heterostructures

In this chapter, growth of h-BN/graphene (vertically stacked h-BN on top of graphene) will be studied. Unlike heterostructure growth, the literature contains many instances of graphene and h-BN being synthesized alone using both chemical and physical vapor deposition methods (CVD and PVD, respectively); experiments which have made clear that metal substrates offer the chemical environment most conducive to the synthesis of high-quality films of both materials. Examples include the widely replicated CVD growth of graphene on Cu foil substrates (e.g. Reference [27] among many others), as well as h-BN synthesis on Ni,[64] Pt(111),[156] Cu,[65] and more. Metallic substrates can support the growth of fully epitaxial films of both graphene[157] and h-BN,[156] and individual crystalline domains millimeters across even in the absence of epitaxy.[158] This is in contrast to graphene and h-BN films deposited on dielectric substrates, which typically results in limited domain sizes and substantial crystalline disorder.[154,159] The efficacy of metallic substrates for the production of high-quality films of graphene and h-BN points to a problem inherent to the production of multilayer heterostructures: once the substrate is covered by the first material, the favorable environment it provides is no longer accessible for the growth of the subsequent material.

Here a novel MBE-based scalable growth method will be introduced which allows both graphene and h-BN to form in a stacked heterostructure in the favorable growth environment provided by a Ni substrate. In Chapter 3, it has been shown that Ni is an effective substrate for the growth of atomically thin and continuous h-BN films. Moreover, Ni substrates have been frequently studied and utilized for the growth of graphene (and graphite layers) using various synthesis techniques such as CVD (among many others),[33,121], and MBE.[39] Here we exploit the finite solubility of C in Ni[33] by first saturating a Ni film [deposited on MgO(111)], then depositing a few-monolayer thick h-BN film from elemental B and N on the exposed Ni surface, and finally ramping the sample temperature down to controllably precipitate the C and form few-layer graphene at the interface between the h-BN and Ni. The resulting heterostructure film is composed of a top layer of h-BN on an intermediate layer of graphene, supported by the Ni/MgO(111) substrate. The resulting heterostructures have been studied using various techniques such as UV and visible Raman spectroscopy and AFM as well as XPS by collaboration with Xianjie Liu from department of physics, chemistry and biology, Linköping university, Sweden. Additionally, GID measurements were performed at beamline BM25B (SpLine) at the European Synchrotron Radiation Facility, Grenoble, France by collaboration with Thilo Krause and Michael Hanke from the department of microstructure, Paul-Drude-Institut für Festkörperelektronik, Berlin. This allowed learning about the structural properties and quality as well as the growth mechanism of the heterostructures. These results illustrate a different pathway for the production of h-BN/graphene heterostructures, and open a new perspective for the large-area preparation of heterosystems combining graphene and other 2D or 3D materials.

5.1 The hybrid synthesis method to grow h-BN/graphene heterostructures

The main steps involved in the fabrication of the h-BN/graphene heterostacks studied here are illustrated schematically in Figure 5.1. The Ni/MgO(111) substrates used here were prepared similar to what has been explained in Chapter 4 [300 nm Ni deposited at room temperature on MgO(111) with Ti back-coating]. After being transported through air into the MBE chamber, the substrate annealed and treated with Ar sputtering in order to desorb water and further cleaning of the surface of the Ni film (see Section 4.1 in Chapter 4 for details). The Ni/MgO(111) substrate was subsequently transferred into the growth chamber and annealed at 850 °C for 20 minutes. The annealing step in addition to the previous Ar sputtering step, helps cleaning the surface from the native oxide as

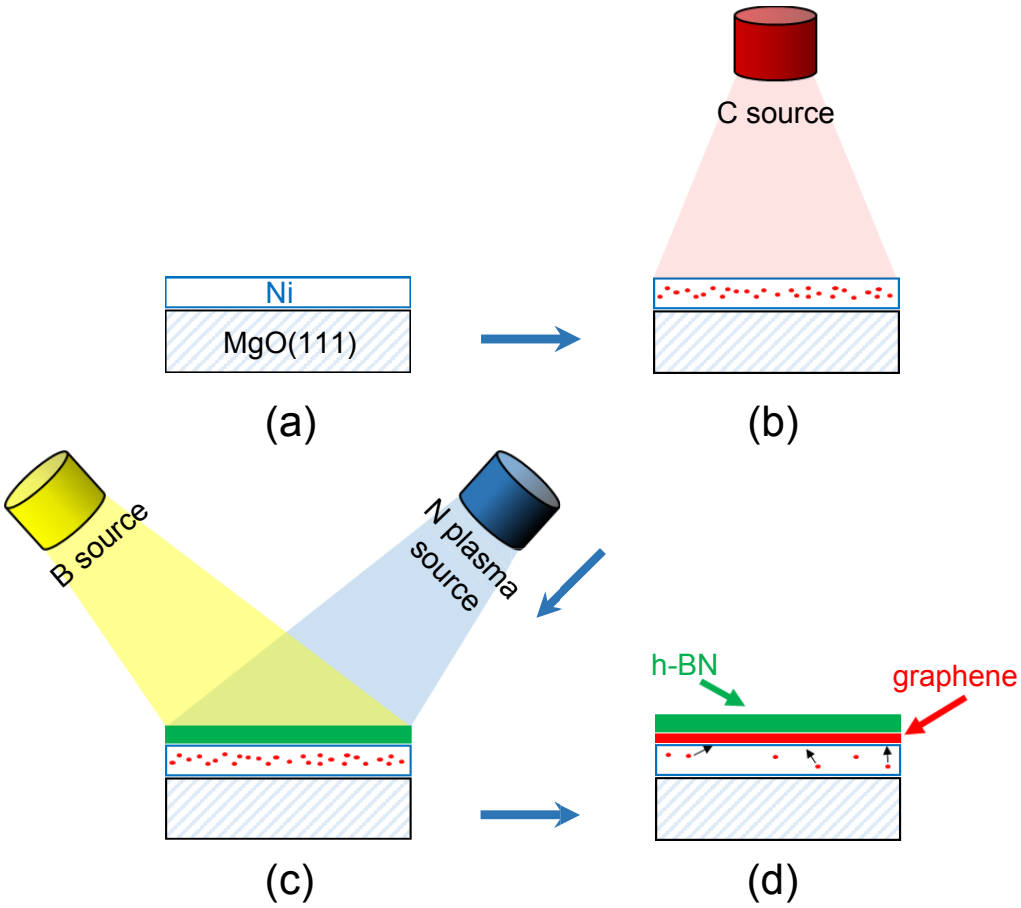

Figure 5.1: Schematic illustration of the synthesis process utilized here for h-BN/graphene heterostructures on Ni/MgO(111) templates. (a) Starting with a blank Ni/MgO(111) substrate (b) C is dissolved into the Ni film by e-gun evaporation at high temperature. (c) This is followed by the MBE growth of a few-layer thick h-BN film on the exposed Ni surface utilizing N-plasma and elemental B. (d) The last step consists of forcing C precipitation from the Ni film by controlled sample cooling, resulting in few-layer graphene forming as a continuous film at the h-BN/Ni(111) interface. Note that the illustrations are not to scale. For the sake of simplicity, possible precipitation of C at the Ni/MgO interface is not considered in the illustrations.

well as smoothing the surface of the Ni.[39] The Ni/MgO(111) stack was subsequently cooled to 730 °C for C saturation, which was accomplished by evaporating elemental C provided from an electron-beam heated HOPG target (Figure 5.1b). For the samples discussed here, a C flux equivalent to few layer graphene (using e-beam parameters: 99 mA, 5 kV, 40 min) was introduced to the Ni surface at 730 °C. The extent of carbon introduced at this step (and later precipitated) was adjusted by changing the duration of C deposition, followed by ex-situ Raman spectroscopy for graphene thickness estimation. The amount of carbon utilized for the saturation step was chosen to avoid the concomitant formation of graphene at the Ni surface,[5,160] with the intent of allowing the subsequent h-BN growth to occur directly on the bare Ni surface. After C deposition was stopped, h-BN was then grown using elemental B and N from a high-temperature effusion cell and an RF plasma source, respectively, similar to what has been described in Chapter 3. Deposition was halted once the h-BN film reached an average thickness of ~3 monolayers (ML, as calibrated by XRR and AFM profilometry – see Section 3.3 in Chapter 3). Finally, few-layer thick graphene (2 to 3 ML) was formed at the interface between the h-BN and Ni from the C previously dissolved in the Ni film by cooling the sample at 4 °C per minute. The resulting heterostructure film is composed of a top layer of h-BN on an intermediate layer of graphene, supported by the Ni/MgO(111) substrate (see Figure 5.1d).

5.2 Topography of heterostructures

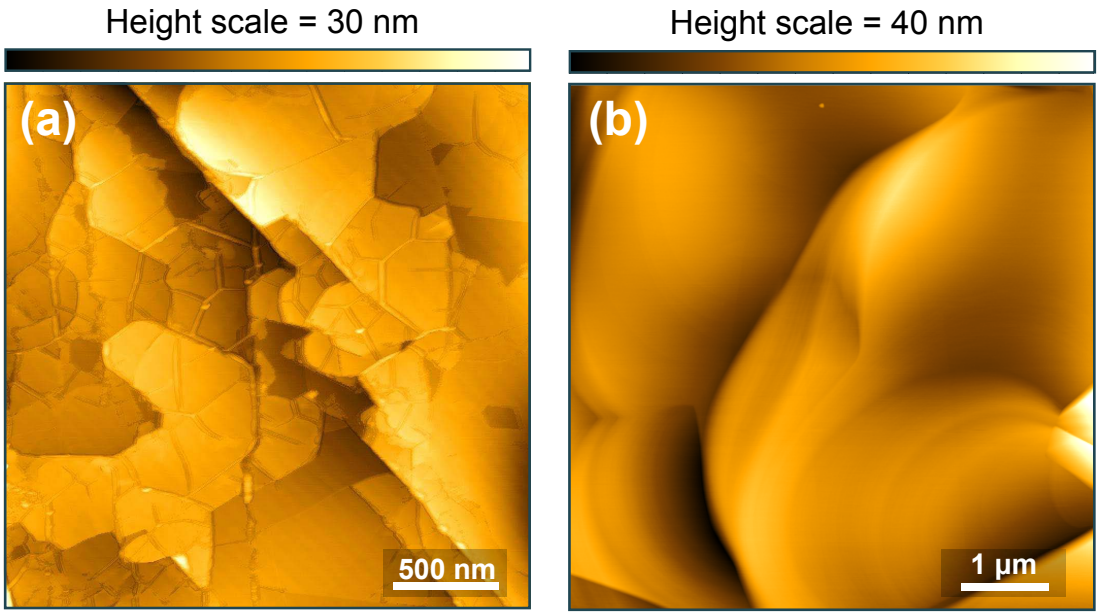

Figure 5.2: (a) AFM image of a h-BN/graphene heterostructure film grown on Ni/MgO(111). The surface shows the typical features resulting from the growth of a 2D material on a metal template (wrinkles), as well as topographic variations such as step edges which originate from the surface of the underlying Ni film. (b) AFM image of a bare Ni/MgO(111) template after annealing at 850 °C for 20 minutes (without subsequent growth). The surface contains typical topographic features of the Ni film surface such as step edges and flat terraces. However, no wrinkles are observed.

AFM scans of the h-BN/graphene heterostructure samples show the network of wrin-

kles typically seen in two-dimensional films grown on metallic substrates (see an example in Figure 5.2a), which is very similar to what previously observed for continuous graphene[39] and h-BN prepared by MBE (see Figure 3.3). The formation of wrinkles takes place during cooling and is mainly related to the unequal expansion coefficients of the 2D materials and Ni. Hence, the wrinkle structure, which is observed in all AFM measurements performed at different locations of the sample surface, indicates that a continuous film is formed after employing the synthesis method described in Figure 5.1d. Note that over larger scales the surface topology is dominated by the features of the underlying Ni film, including step clusters and grain boundaries. Height variations seen in the AFM image are mainly related to these, as well as to localized thickness inhomogeneities in the h-BN and graphene coverage. Figure 5.2b shows, for comparison, an AFM height image of a bare Ni/MgO(111) prepared in the same manner (treated with exact temperatures and durations) but without subsequent heterostructure growth.

5.3 Raman characterization of the heterostructures

5.3.1 Visible excitation Raman spectroscopy

Figure 5.3 presents a Raman spectrum from a h-BN/graphene heterostructure showing the scattering peaks characteristic of both materials. The G and 2D peaks of the few-layer graphene spectrum are clearly defined, and the defect-related D peak has a low relative

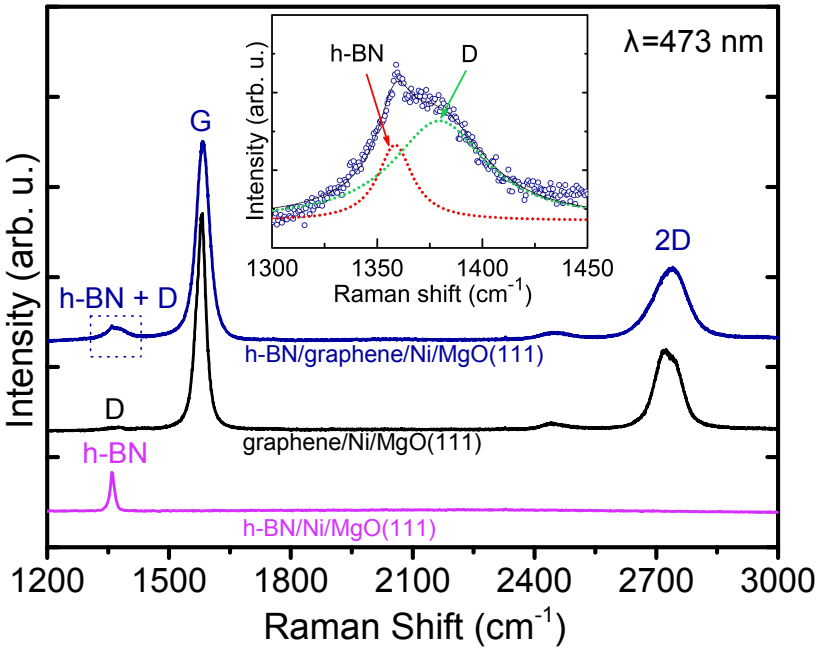

Figure 5.3: Raman spectra of a h-BN/graphene heterostructure film (blue), as well as of pure graphene (black) and h-BN films (magenta) also grown by MBE. All spectra were excited at λ = 473 nm. Note that for the h-BN spectrum the Ni-related background was subtracted. The inset shows a magnification for the heterostructure film spectrum of the region where the D peak of graphene and h-BN related peak overlap. The contribution located at ~2450 cm^{-1} is the D + D'' peak (detailed information about this mode can be found elsewhere).[161]

intensity. The D peak is probably associated to the defects originated from an unintentional N-doping of the underlying graphene, as it will be discussed later. For comparison, the Raman spectra obtained from pure MBE-grown graphene [graphene/Ni/MgO(111)] as well as pure MBE-grown h-BN [h-BN/Ni/MgO(111)] using the same growth parameters as for the heterostructure constituents, are also presented in Figure 5.3 (see Section 5.1 for more details). For the heterostructure case, it is immediately apparent that the Raman signal originating from the graphene layer is significantly more intense than that from the h-BN film. This is to be expected because even though the two materials are present in approximately the same quantity, scattering from the graphene film is resonant with excitation lasers in the optical range (λ = 473 nm here, or E = 2.62 eV), while the h-BN is not. The observation of the h-BN signal in the combined heterostructure spectrum is further complicated by the overlap of its characteristic peak with the D peak of graphene. However, a closer examination of the relevant spectral range (inset in Figure 5.3) clearly shows the Raman intensity to be composed of separate and distinct peaks, confirming the presence of both materials. The narrow FWHM of the h-BN peak, 12 cm^{-1} is also consistent with the high crystalline quality of the h-BN. When using the 473 nm laser the Raman signal from graphene was observed regardless of where the spectrum was collected, confirming the formation of continuous few-layer graphene film over the entire heterostructure. However, the h-BN Raman peak was possible to resolve only at ~20% of the locations examined, possibly coinciding with locally thicker regions in the h-BN film. Raman mapping using this laser line was also not possible due to the presence of spatially inhomogeneous luminescence coming from the Ni substrate.

5.3.2 UV excitation Raman spectroscopy

Unlike Raman scattering in the visible spectrum, UV excitation (λ = 244 nm, or E = 5.08 eV) allowed the continuity of the h-BN over the full heterostructure to be verified. Figure 5.4a depicts a typical Raman spectrum from a h-BN/graphene film excited with the UV laser. The signal related to the E_{2g} optical phonon of h-BN is enhanced, since the efficiency of Raman scattering from h-BN exhibits a certain degree of resonance for excitation at 5.08 eV.[124] In addition, previous studies have shown that both the D and the 2D peak of graphene exhibit a linear blue-shift as well as a strong decrease in intensity with increasing excitation energy, while the G peak position remains unaltered.[101,106,162,163] Considering the linear dispersion suggested in literature,[106] the D peak of graphene is expected at ~1485 cm^{-1} when the 5.08 eV laser is used. Thus, the well-defined peak observed at ~1364 cm^{-1} originates purely from the h-BN in the heterostructures. This peak was always detected in numerous UV Raman point measurements and mappings regardless of the position being measured, which indicates that the h-BN forms as a continuous layer covering the entire heterostructure rather than as isolated islands. A representative map of the position of this peak over a 50 µm × 50 µm area is shown in Figure 5.4b. The h-BN's Raman signal is always clearly observed in the presented map with a signal to noise ratio typically around 500 and always better than 100. The frequency of the h-BN phonon line is found to be centered at ~1364 cm^{-1} (consistent with the reported values for bulk h-BN)[124,127] with a total variation between 1360 and 1367 cm^{-1}. We did not observe any significant intensity near 1485 cm^{-1} in Raman spectra collected from the heterostructures; consistent with the quenching of the graphene's D peak in UV Raman measurements.[106] The broad band observed at ~3150 cm^{-1} (labeled as 2G) is attributed to a non-resonant second-order Raman scattering in graphene.[164] The 2D peak could

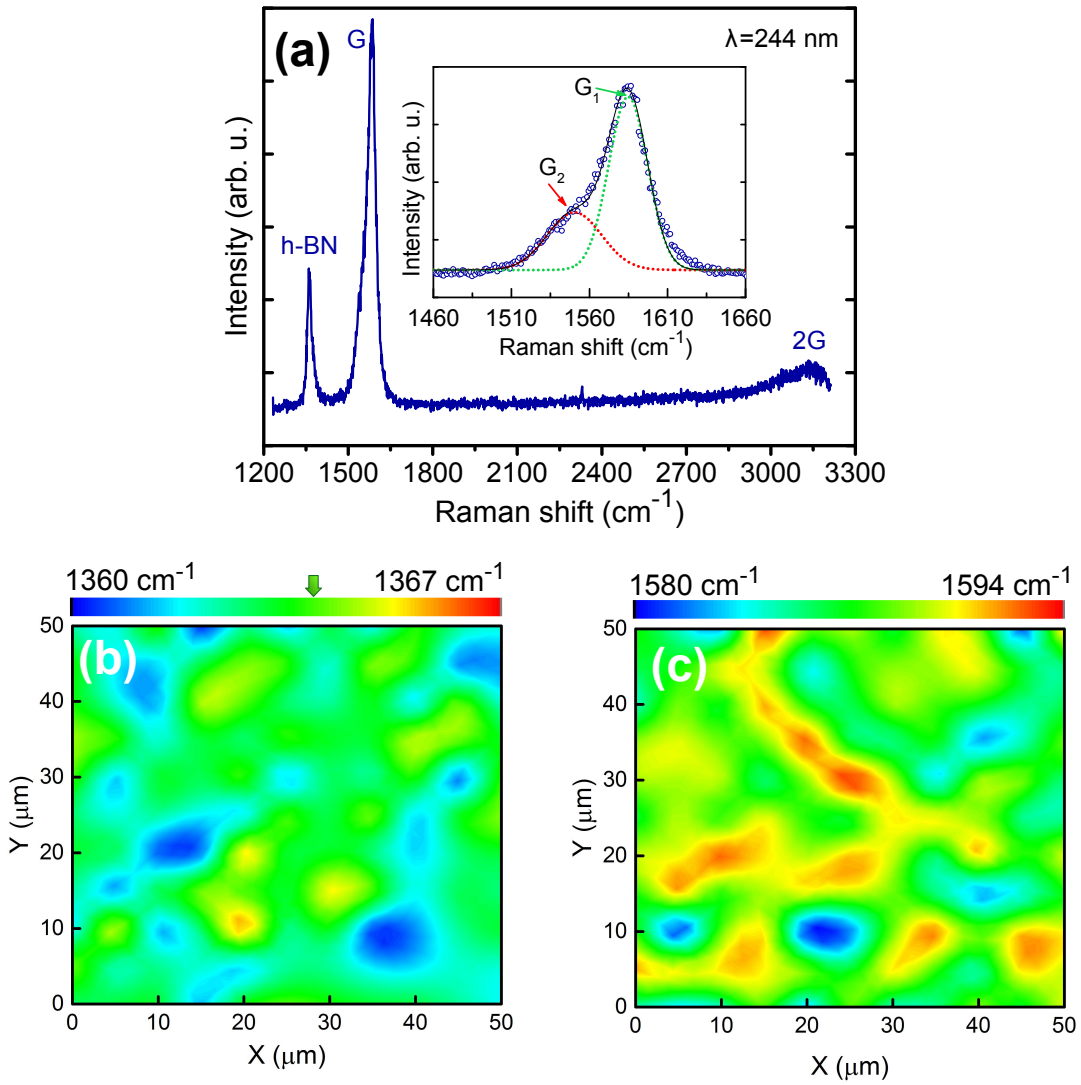

Figure 5.4: (a) UV Raman spectrum of heterostructure excited at $\lambda = 244$ nm (E = 5.08 eV). The inset shows a magnification of the region around the G peak. The G peak is fitted with two Gauss functions (G_1: green dashed line and G_2: red dashed line). (b) and (c) Mappings of the position of the h-BN phonon line and of the G_1 peak (the more prominent component of the G peak) of graphene, respectively. They were both acquired for the same 50 µm × 50 µm area. The arrow in (b) shows the peak position of bulk h-BN at 1364 cm^{-1} according to literature.[124] The corresponding UV Raman mapping were recorded with excitation at $\lambda = 244$ nm. The signal to noise ratio for the mappings in (b) and (c) was always larger than 100.

not be detected in the UV Raman measurements, which is also consistent with previous studies.[162,164,165] The most prominent peak present in all UV Raman spectra is the G peak of graphene. Interestingly, it has an asymmetric shape and is composed of two components: a more prominent component observed within the 1580–1594 cm^{-1} range (G_1), and a small shoulder centered at 1555 ± 20 cm^{-1} (G_2 – see the following discussion for further details). Figure 5.4c shows a mapping of the position of the G_1 component, which

was taken at the exact same position as the h-BN map (Figure 5.4b). As in the case of h-BN, the uninterrupted and clear detection of this graphene-related peak in numerous measurements performed at different surface positions serves to demonstrate the lateral continuity of the graphene formed underneath the h-BN.

5.3.3 Raman analysis of heterostructures transfered onto SiO_2/Si substrates

A standard wet chemical transfer technique based on a method published previously [166] was used to transfer the h-BN/graphene heterostructures from the growth substrate

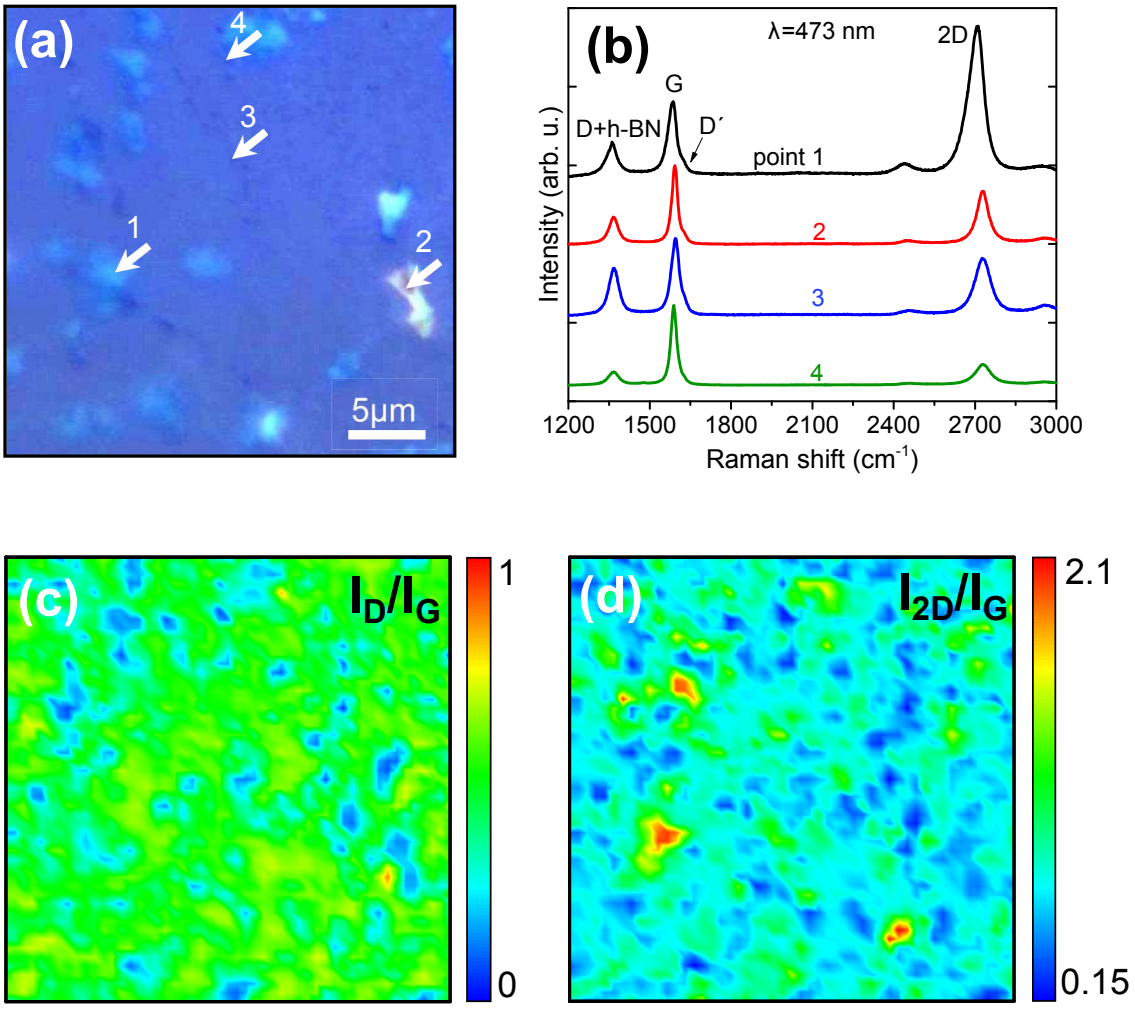

Figure 5.5: Raman spectroscopy results obtained from a transferred heterostructure. (a) Optical micrograph (30 μm × 30 μm) of a h-BN/graphene heterostructure transferred onto SiO_2/Si wafer. The brightness and contrast of the image is manually enhanced for a better demonstration. (b) Raman spectra of the points shown by arrows in (a) using a 473 nm laser. (c) and (d) show the Raman maps of the D peak intensity over G peak intensity (I_D/I_G) and 2D peak intensity over G peak intensity (I_{2D}/I_G), respectively, measured over the exact same area presented in (a). Please note that the intensity measured for the D peak also includes a small contribution from the h-BN peak (at ~1364 cm^{-1}).

[Ni/MgO(111)] onto SiO_2/Si substrates. Raman measurements performed on the transferred h-BN/graphene heterostructure films yielded very similar results. For instance, the G and 2D peak of graphene were also observed in all spectra obtained from the transferred heterostructures, reconfirming the presence of graphene all over the heterostructure. Moreover, it was also possible to perform Raman mappings using visible light excitation as a Ni-related background signal was not present. Figure 5.5a presents an optical micrograph of a transferred h-BN/graphene onto SiO_2/Si substrate. The regions with higher brightness can be related to thickness inhomogeneity in the h-BN and/or in the graphene layers. Figure 5.5b depicts four Raman spectra obtained from typical regions in the transferred heterostructure film. Maps of the D peak intensity over G peak intensity (I_D/I_G) and 2D peak intensity over G peak intensity (I_{2D}/I_G) measured over the exact same area shown in Figure 5.5a are presented in Figures 5.5c and 5.5d, respectively. Please note that the transfer process itself may induce additional defects in the structure of the graphene layers, affecting the D (and D') peak intensity. Finally, the Raman results obtained from the heterostructures serve as a piece of evidence for the formation of few-layer graphene at h-BN/Ni interface and not on top of the h-BN. Previous studies have shown that at similar growth temperatures, even the direct deposition of C on top of exfoliated h-BN single crystals results in highly defective and localized graphene (i.e. exhibiting a D peak that is more intense than the G peak)[153,167] which is not the case for the heterostructures reported here.

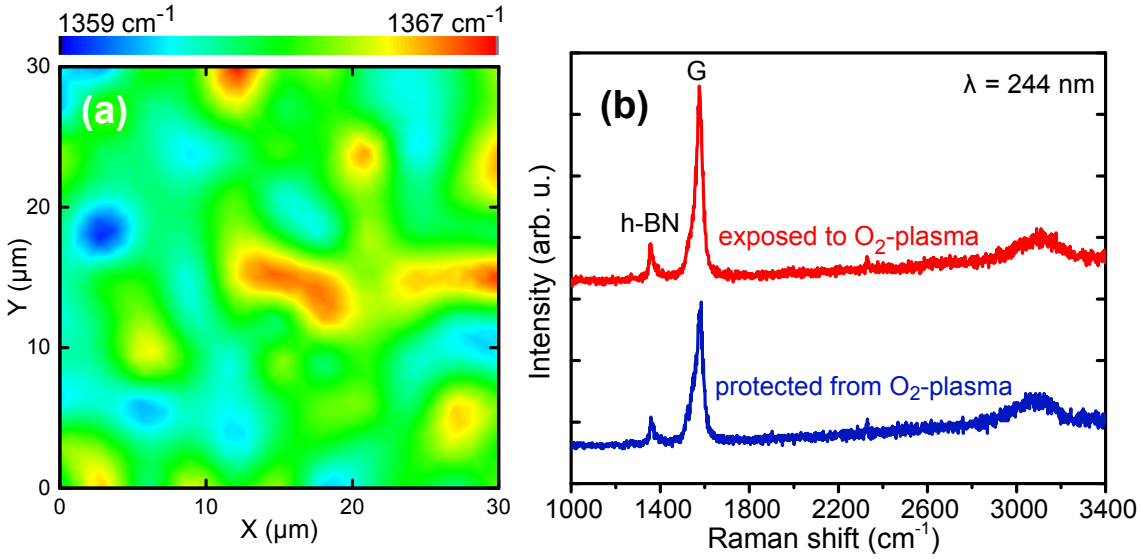

Figure 5.6: UV Raman spectroscopy of a transferred heterostructure: (a) Map of the h-BN's peak position over a 30 μm × 30 μm area obtained from the transferred h-BN/graphene onto a SiO_2/Si wafer using the 244 nm (E = 5.08 eV) laser. The signal to noise ratio of the h-BN peak was always better than 100. (b) Raman spectra from a transferred h-BN/graphene heterostructure using the UV laser. The red spectrum is acquired from a region which was exposed to O_2-plasma, while the blue one is obtained from a region which was protected by a solid mask from the plasma.

The h-BN's characteristic peak (at ~1364 cm^{-1}) was also always observed in UV Raman measurements performed on the transferred heterostructures (see Figure 5.6a), confirm-

ing that a h-BN film is present over the entire heterostructure, also showing a successful transfer process of heterostructures. The stacking order of graphene and h-BN layers was additionally verified by exposing a heterostructure sample to O_2-plasma treatment (plasma parameters: 100 W, 2 minutes, O_2 pressure: 0.5 mbar) which etches graphene[42,135] (in case it had been formed on top of h-BN), and preserves h-BN. Raman measurements show that the G peak of graphene is preserved in the O_2-plasma treated areas (Figure 5.6b), showing that the Raman signal originates from graphene formed under the h-BN layers.

5.3.4 Discussion

As already pointed out, our Raman investigations provide evidence for the presence of unintentional modifications in the few-layer graphene film formed at the interface. In fact, for our growth experiments, graphene doping and/or alloying close to the h-BN/graphene interface cannot be ruled out. During the growth of h-BN (see Figure 5.1c), when B and N are exposed to the hot surface of Ni, it is possible that undissolved C atoms and even a few graphene inclusions from the previous saturation step (see Figure 5.1b) are present at the Ni surface. In this environment, a stronger interaction between C and N is anticipated considering a relatively strong reactivity of N species generated by the plasma source in comparison to elemental B. In this case, the main modification taking place in the few-layer graphene would be doping with N which is probably inhomogeneous laterally and along the growth direction. In addition to the existence of a low-intensity D peak, which is consistent with the existence of defects originated from N-doping,[168] the observed position of the G_1 peak (see Figure 5.4c) is generally blue-shifted as compared to the one of pristine graphene (at ~1580 cm^{-1}),[169] which suggests that N and/or B atoms have been incorporated into the graphene film as dopants.[168,170,171] Furthermore, the splitting of the G peak into two components indicates the existence of a doping (charge density) gradient across the few-layer graphene film, which induces a dipole formation between the topmost and bottom graphene layers. The inversion symmetry breaking induced by such gradients is known to result in a G peak splitting.[172,173] An alternative explanation for the low-frequency G_2 peak is a possible alloying of the h-BN and graphene films close to their interface. In previous work, the observation of a red shift and broadening of the G peak in h-BNC alloys with respect to pure graphene has been reported.[174,175] Uddin et al. recently proposed that the G peak of graphene downshifts (towards the h-BN phonon line), when a homogeneous single phase alloy of h-BNC is formed.[176] Nevertheless, the overall shape of the Raman spectra (e.g. broad D and G peaks and high D peak intensity) reported by these studies and more recently by Meng et al.,[177] also for h-BNC alloy films, is different from what is observed in the present case. This and the XPS and GID results shown next, indicate that alloying does not take place in the heterostructure films studied here.

5.4 XPS analysis

XPS was employed to investigate the chemical composition and binding states of the heterostructures. The samples were transferred in air for the XPS measurements. The measurements were performed using a Scienta ESCA 200 spectrometer with a base pressure of 7.5×10^{-11} Torr. The chamber was equipped with a monochromatic Al(K alpha) X-ray source providing photons with 1486.6 eV for XPS. The experimental condition was

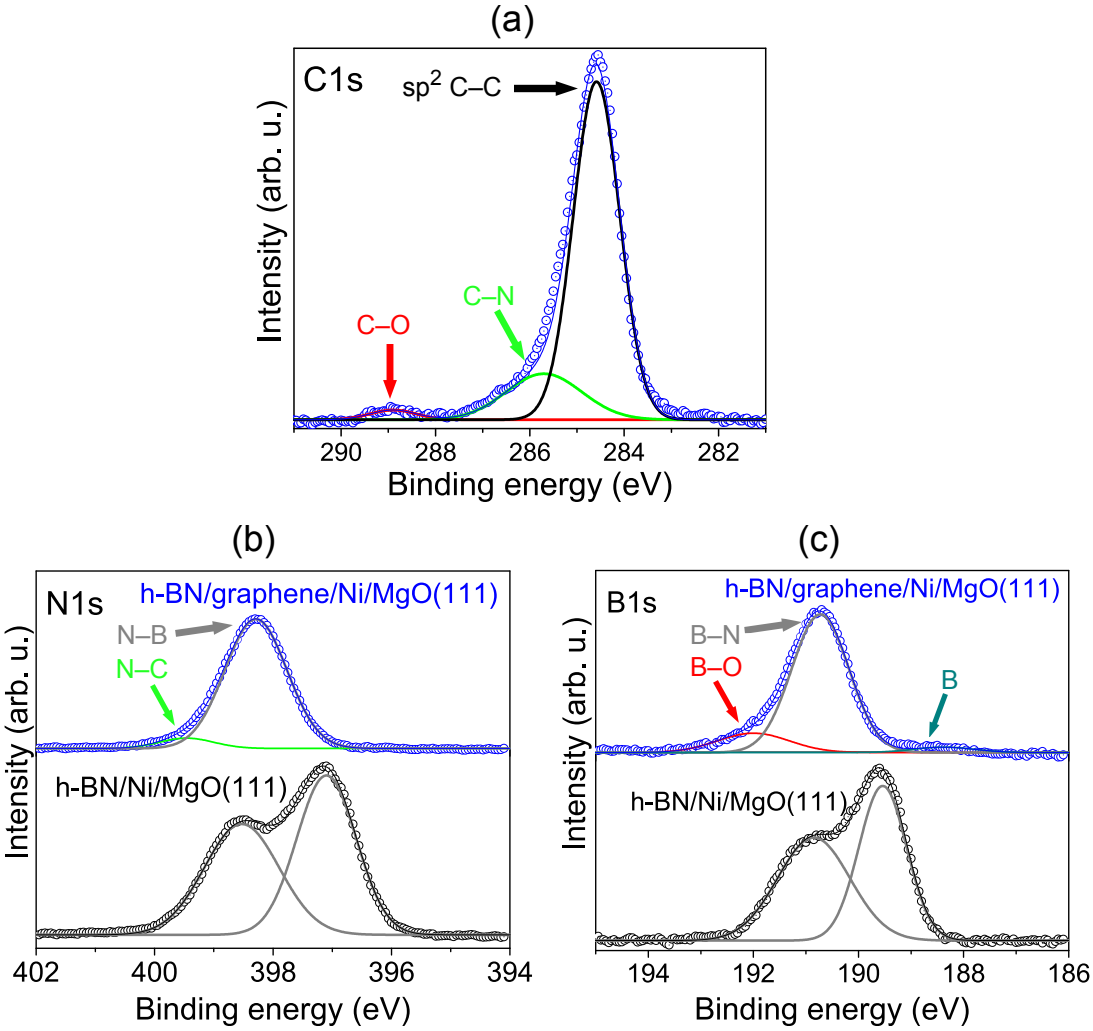

Figure 5.7: XPS core-level spectra of the (a) C1s, (b) N1s, and (c) B1s regions for h-BN/graphene heterostructure film (a-c) and h-BN (b,c) synthesized on Ni/MgO(111) templates.

set so that the FWHM of the clean Au 4f7/2 line was 0.65 eV. All spectra were collected at room temperature with a photoelectron takeoff angle of 0° (normal emission) and without sample pre-annealing.

5.4.1 Binding states of B, N, and C in h-BN and h-BN/graphene heterostructures

Figure 5.7 displays the C1s, B1s, and the B1s spectral regions obtained from the h-BN/graphene heterostructure. For comparison, the N1s and B1s regions of a h-BN film grown on a Ni/MgO(111) template utilizing the exact same parameters (but without the C saturation step illustrated in Figure 5.1b) is also presented. For the latter, both the N1s (Figure 5.7b) and B1s (Figure 5.7c) core level spectra show two components. For the N1s region, they are located around 398.5 and 397.1 eV, and for the B1s region around 190.8 and 189.6 eV. This result is very similar to what has recently been reported by Yang et

al.[178] for h-BN synthesized on Ni(111) by CVD. According to this report, the existence of epitaxial (and thus tightly bound to the Ni) and non-epitaxial (weakly bound) h-BN islands on the Ni surface is the origin of the high- and low-binding energy components, respectively. A strong correlation between the N1s and B1s binding energies and the interaction between h-BN and the underlying metal template has also been observed for the cases of Ru, Rh, Ir, and Pt.[179–182] An analogous scenario is likely in our h-BN samples, where different regions of h-BN interact differently with the underlying Ni surface.[183] It is therefore anticipated that h-BN grown on the atomically flat (111) terraces is tightly coupled to the metal surface,[184] whereas a weaker interaction probably takes place at step edge clusters and other disordered regions.[185]

The results obtained from a heterostructure sample exhibit marked differences in the N1s and B1s spectral regions. They are both now composed of a dominant component with binding energies around 398.3 (N1s) and 190.7 eV (B1s). These values are in good agreement with previously published data for h-BN on top of graphene.[86,89] The existence of a weak component located at 399.6 eV in the N1s region is interpreted as being due to N-C bonding,[168,186] whereas the B1s contributions at ~188.3 eV and 192 eV can be associated with the existence of elemental and oxidized B.[187,188] Although a B/N intensity ratio around 1 was found, as expected for stoichiometric h-BN, a slight excess of surface B might be the reason for these observed contributions (see Figure 3.3).[119] Note that despite not being observed in spectra from the purely h-BN film (probably due to the much higher intensity of the double-shape h-BN related peaks), excess surface B (and associated oxidized B) is also expected for this sample.

The existence of graphene in the heterostructure film is confirmed by measuring the C1s spectral region (Figure 5.7a), which is dominated by a component with a binding energy around 284.6 eV associated with the sp^2 bonded C atoms within graphene.[86,89,189] The shoulder observed on the higher binding energy side is due to an additional component located near 285.8 eV, and has been correlated to bonding between C and N atoms.[168,190,191] The weak component observed at 288.9 eV can be attributed to a slight CO contamination in the heterostructure films, and has also been observed for pure h-BN films.[191,192] The formation of C-B bonds, which should result in components appearing at a lower binding energy in the C1s region (283–283.5 eV), and in the 187–188 eV range for the B1s level,[175,177,187] were not detected. This suggests that a weak N doping of the graphene film during the initial stages of the h-BN growth is indeed the main reason for the splitting of the G peak observed by UV Raman spectroscopy.

5.4.2 Discussion

Importantly, the transition from two-component to one-component XPS spectra reveals that the heterostructure formation leads to a more homogeneous interaction of the h-BN film with the underlying template, a result of the continuous few-layer graphene coverage formed at the h-BN/Ni interface via C precipitation. It indicates that the synthesis approach used here results in the growth of graphene underneath the h-BN, even in regions where the first h-BN atomic layer is strongly bound to the Ni surface. This is different from what has recently been reported for the CVD-based synthesis of graphene under h-BN, in which graphene could only be formed under weakly bound h-BN islands.[178] Hence, in order to get initial insights on the feasibility of such constricted interfacial graphene growth as observed here, it is interesting to consider aspects related to the growth of graphene films by MBE on the same type of Ni/MgO(111) templates.

Wofford et al.[39] have shown previously that graphene starts to grow at step edge clusters and then propagates to the terraces to form an extended layer. Sequential growth (from below) of further graphene layers will also initiate at the step edge regions.[33,39] In the present case, even though the Ni surface is covered by h-BN, a similar formation mechanism appears to be feasible. This is a result of the expected weaker interfacial bond between h-BN and Ni in regions containing step edge clusters in comparison to the strong interaction present in Ni(111) regions.[185] Interestingly, for graphene this interaction remains strong regardless of the Ni surface region.[185] In this way, the existence of weakly bonded h-BN coverage at step edge clusters should not constitute a barrier for the formation of underlying graphene at this region. However, the formation of graphene at the h-BN covered Ni(111) terraces is somewhat more intriguing, given the similar origin of strong chemical bonding occurring at h-BN/Ni(111) and graphene/Ni(111) interfaces (the hybridization between Ni d state and π states of the 2D layer).[136–139] In spite of their similar nature, Oshima et al.[193] suggest that stronger interfacial bonding takes place between graphene and Ni as compared to h-BN and Ni. Such a difference becomes significant when considering the two paradigms through which graphene may grow during the C precipitation at the h-BN/Ni interface: as thicker graphene/graphite deposits (possibly confined to step edge clusters), or as a continuous film (as it is observed experimentally here). It is illustrative to differentiate these two modes using a simple energy balance, analogous to traditional thin film growth on an exposed substrate surface [i.e. Volmer-Weber (VW) vs. Frank-van der Merwe (FM) growth].[194] There are four interfacial (γ) energies: the bonding strength between h-BN and Ni ($\gamma_{\mathrm{hBN/Ni}}$), between graphene layers ($\gamma_{\mathrm{Gr/Gr}}$), between graphene and h-BN layers ($\gamma_{\mathrm{Gr/hBN}}$), and between graphene and Ni ($\gamma_{\mathrm{Gr/Ni}}$). Given the similar van der Waals interactions between layers in both graphene and h-BN – and its small absolute magnitude – the strength of the bonding between each material and the Ni surface is likely to dominate. If the energetic driving force to maintain the h-BN/Ni bonding is larger than the graphene/Ni binding energy:

$$\gamma_{Gr/Gr} + \gamma_{hBN/Ni} > \gamma_{Gr/hBN} + \gamma_{Gr/Ni} \quad , \tag{5.1}$$

the graphene will preferentially form thicker multilayer deposits, minimizing the total area of h-BN which is decoupled from the Ni surface upon C intercalation (similar to VW growth mode). However, if the graphene/Ni binding energy is larger:

$$\gamma_{Gr/Gr} + \gamma_{hBN/Ni} < \gamma_{Gr/hBN} + \gamma_{Gr/Ni} \quad , \tag{5.2}$$

the formation of a continuous graphene film will be more favorable (comparable to FM growth mode). The observation of the continuously detected graphene Raman signal across the sample surface proves that the C precipitated as a continuous graphene film, consistent with the behavior expected from the h-BN/Ni and graphene/Ni interactions.[193] Note that this analysis assumes that thermodynamics rather than kinetics dominating the growth, which is reasonable given the extremely slow cooling rate used during the precipitation process (4 °C/min).

5.5 Structural analysis of heterostructures using GID

Grazing incidence X-ray diffraction (GID) was used to evaluate the crystalline configuration of the surface layers of the heterostructure. These experiments were performed at beamline BM25B (SpLine) at the European Synchrotron Radiation Facility (ESRF),

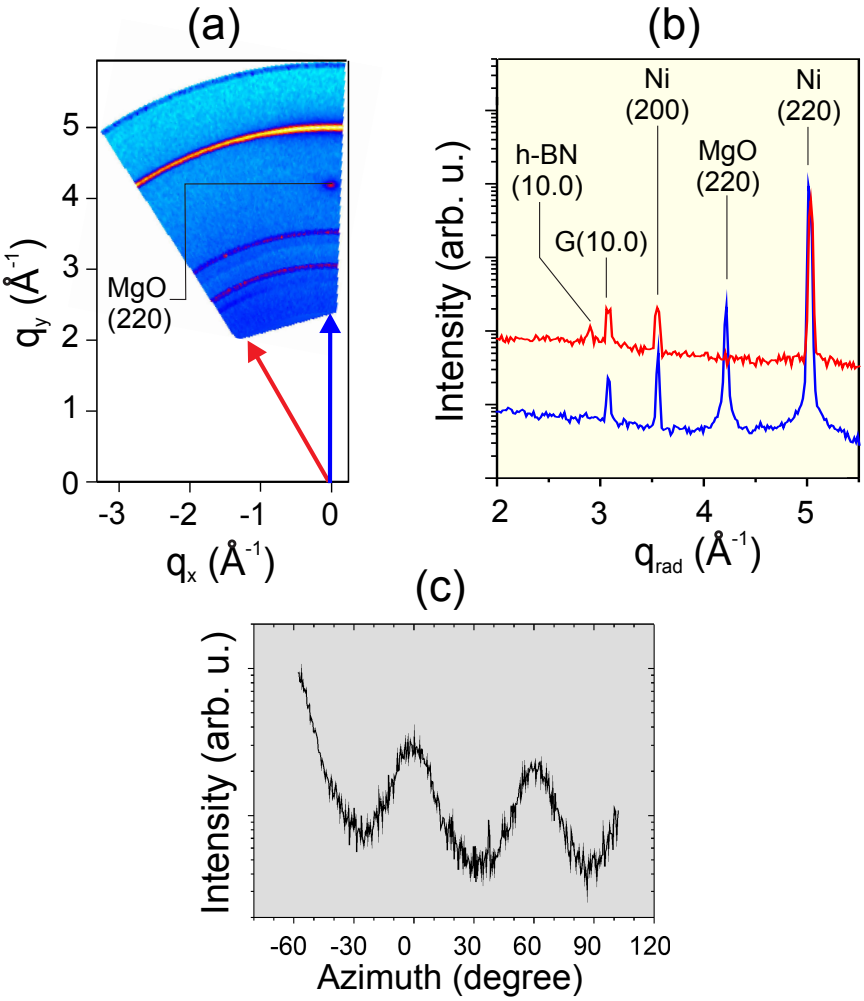

Figure 5.8: (a) GID reciprocal space map, and (b) radial scans from a h-BN/graphene heterostack grown on Ni/MgO(111) [see blue and red arrows in (a)]. Although difficult to resolve in (a), diffraction peaks from both h-BN and graphene are easily observed in (b). The Ni-related diffraction in (a) forms rings, showing that there is rotational disorder. (c) shows the intensity profile obtained from the angular scan along the ring-like Ni contribution in (a). There is a preferential alignment of Ni[110] ‖ MgO[110], however, Ni has a textured character.

Grenoble, France. The X-ray energy used was 20 keV, with the beam at a 0.1° angle of incidence to ensure a high degree of surface sensitivity. Both constituent materials of the h-BN/graphene heterostructures could also be detected via GID. This technique has proven to be very powerful in obtaining precise information about the structural properties of single graphene layers.[135] Figure 5.8a shows a reciprocal space map of the sample surface, which is dominated by intense diffraction from the larger volume of the Ni film and MgO(111) substrate. The ring-like structure of the Ni-related features indicates a polycrystalline film composed of (111) oriented domains, with a preferential orientation of Ni(220) parallel to MgO(220) visible in the intensity modulation along the ring (Figure 5.8c). Examining two radial scans – one along the <110> direction (Figure 5.8b, blue)

and one rotated azimuthally by 30° (Figure 5.8b, red) – allows the comparatively weak h-BN and graphene reflections to be resolved. The diffraction peak at 2.899 $Å^{-1}$ results from the (10.0) reflection of the h-BN lattice, and corresponds to an in-plane lattice spacing of 2.502 Å which is very close to its bulk value.[46] Moreover, the h-BN peak shows a stronger structural correlation with the Ni surface as the arc formed by its (10.0) diffraction is centered on the 30° rotated scan. This is consistent with its growth occurring on the bare metal.[137] The (10.0) reflection of graphene at 3.085 $Å^{-1}$, however, refers to an average real-space in-plane lattice parameter of 2.352 Å, and reveals that the graphene lattice is strongly compressed in about 4% (in comparison to graphite – a = 2.461 Å).[135] The direct contact between graphene and Ni(111) leads to a compression of the graphene lattice during cooling because of the different thermal expansion coefficients of graphene and Ni.[5] Nevertheless, this effect alone cannot account for the lattice shrinkage measured by GID. Substitutional incorporation of N atoms in the graphene lattice is most likely the dominant effect behind it, since the length of the C-N covalent bond is shorter (1.32 Å) than that of the C-C one (1.42 Å).[195] Additionally, N incorporation in pyridinic and pyrrolic sites,[168,186,191] which is also likely to take place, will result in the creation of vacancies in the graphene lattice. This type of point defect is known to contribute to a reduction of the average lattice parameter in graphene.[40] Note that the lattice parameter as well as the general blue-shift of the G peak of graphene observed here are very similar to what have been reported by Zafar et al.[168] for N-doped graphene with an average N concentration of 3% prepared by CVD on Cu substrates. Overall, the results obtained by GID corroborate the Raman and XPS findings. As previously mentioned, the preference for N incorporation instead of B is probably associated with the higher reactivity of the N species generated by the plasma source during the growth of the h-BN layers. Finally, the GID data show that the graphene film contains a larger rotational disorder in comparison to the h-BN one (as illustrated by its presence in both radial scans). The extent of rotational disorder in the graphene agrees with previous reports which show that growth on Ni at substrate temperatures above 650 °C reduces the likelihood of epitaxy.[196]

5.6 Summary and conclusions

In this chapter, a novel growth method for the production of layered h-BN/graphene heterostructures based on MBE was demonstrated. The utilization of a Ni film pre-saturated with C as a substrate for h-BN deposition is shown to enable the growth of few-layer graphene at the h-BN/Ni(111) interface by controllably ramping the temperature down to precipitate the C out of the metal. The primary benefit of this technique is that both constituent materials of the heterostructure form in the chemically favorable environment offered by the Ni surface, resulting in continuous graphene and h-BN layers. The top h-BN layer in the stack is strain free, consistent with it being decoupled from the Ni substrate due to the interfacial graphene growth. A careful analysis of the material properties also revealed a significant contraction of the graphene's crystal lattice due to N-doping. We correlate the N-doping to the possible existence of undissolved C atoms and graphene inclusions present at the Ni surface at the moment when h-BN starts to be grown. Further adjustment of growth parameters shall be implemented in order to mitigate this effect. Another possibility is to remove the surface C using Ar sputtering before start of the h-BN growth. In terms of thickness homogeneity, it is anticipated that the use of Ni films with smoother surfaces and thus a lower density of step clusters will be beneficial. The h-BN/graphene heterostructure film could be transferred to a SiO_2/Si

substrate without having its structural properties substantially affected, as verified by Raman spectroscopy. In general, the procedure described here offers an alternative route for the scalable production of h-BN/graphene heterostructures which overcomes many of the drawbacks faced by other methods. It also opens a new pathway for the production of other heterosystems composed of graphene in combination with another material, especially in cases where the formation of a homogeneous graphene under-layer (e.g. as a bottom electrode) might be required.

6 Growth of graphene/h-BN heterostructures

Graphene supported by a dielectric material is ideally suited for integration in various device applications. However, most of investigations on devices involve transfer of graphene, obtained from mechanical exfoliation or grown by CVD technique. Besides the time and scalability issues, there is always a high chance of introducing contamination and damage to the graphene, which is inherent to a transfer process. Overcoming such challenges has led to intensive ongoing research efforts to directly grow graphene on top of dielectric materials. Among various growth techniques being investigated for this purpose, MBE stands as a promising technique due to the good control it offers over the growth conditions. Recently, growth of graphene on non-metal substrates using MBE has been intensively investigated. Various device-compatible dielectrics such as Al_2O_3,[42,197–201] mica,[202,203] SiO_2,[204] Ge,[41] and h-BN[150,153,167,205] have been tested as the growth substrate. Besides the favorable assets that each of these non-metallic growth substrates offers, there are also weak aspects, which puzzle the realization of the growth of high-quality graphene. One common major challenge that most of the dielectric substrates share is the limited diffusion length of C atoms on their surfaces as compared to the metal surfaces. In other words, the C ad-atoms can diffuse very small distances before they incorporate into the most energetically favorable attachment sites (sp^2 sites) in edge of the growing graphene, which leads to the formation of coalesced graphene crystallites with small domain size and degradation of its crystalline quality. The resulting graphene film is typically referred to as "nanocrystalline graphene" in literature. Although a good progress has been achieved, such as thickness controlled growth[42] or epitaxial growth on h-BN flakes,[205] a growth recipe offering control over thickness and quality over large areas remains elusive. In particular, to the best of my knowledge, in-situ growth of graphene on large-area MBE-grown h-BN has not been reported yet.

As the last chapter in this thesis, the large-area MBE-grown h-BN films [h-BN/Ni/MgO(111)] are tested as growth substrates for the direct deposition of C atoms. The main goal of this chapter is to demonstrate the feasibility of the growth of large-area graphene/h-BN heterostructures by means of MBE. The resulting graphene/h-BN heterostructures are then characterized using Raman spectroscopy and AFM. The experimental outcome clearly demonstrates the complexity of the topic. Although possible explanations and discussion are offered based on the investigations presented in Chapters 4, 5 and previous studies in literature, yet, these experimental findings should be considered as preliminary results and as a step towards the controlled growth of large-area graphene/h-BN heterostructures.

6.1 Direct deposition of graphene on h-BN films

The growth templates used for the synthesis of graphene/h-BN heterostructures were identical to the ones utilized for the growth of samples studied in Chapter 4 and 5; 300 nm Ni films deposited at room temperature on 1×1 cm^2 pieces of MgO(111) by electron beam evaporation, and back-coating the MgO(111) with 1 µm of Ti. After preparing the

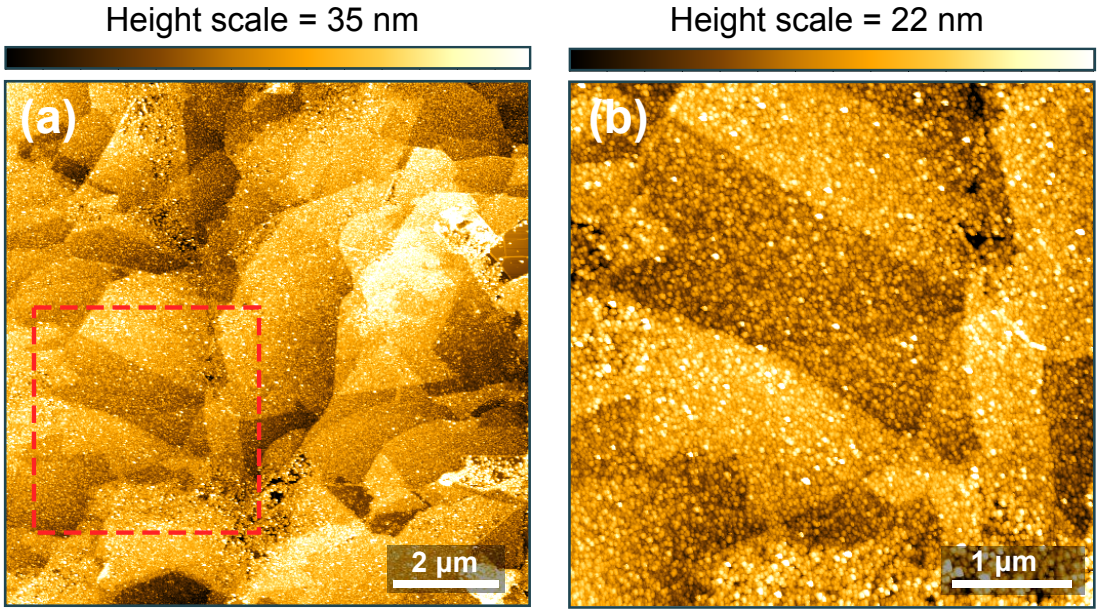

Figure 6.1: AFM images of a graphene/h-BN heterostructure grown on Ni/MgO(111) templates with the C deposition step performed at 730 °C. (a) shows a typical morphology of a larger area of the sample. The scan from the red dashed square in (a) is given in (b).

Ni surface in the MBE chamber, h-BN was grown over 300 minutes at 730 °C utilizing the similar parameters which resulted in the growth of atomically thin continuous h-BN films (see Subsection 4.2.1 in Chapter 4). Subsequent to h-BN synthesis, the graphene film was grown by direct deposition of C atoms evaporated from HOPG (using e-beam parameters: 150 mA, 5 kV) onto the surface of h-BN at 730 °C over 10 minutes. The utilized e-beam parameters results in a C flux of ~8.3×10^{14} atoms/cm^{2}s, as estimated from ex-situ AFM thickness measurements of a C film deposited at room temperature. This corresponds to about 130 ML of graphene, if it is assumed that all C atoms are retained at the surface to form graphene. However, the average thickness of the C film grown on h-BN at 730 °C was about ~5 nm (~15 ML) as roughly estimated by AFM profilometry. The resulting graphene/h-BN film was then studied using Raman spectroscopy and AFM. Additionally, the effect of substrate temperature for the growth of graphene was examined. Two additional substrate temperatures were tested: ~600 °C and 835 °C.

6.2 Raman and AFM analysis of graphene/h-BN heterostructures

Figure 6.1 depicts AFM images obtained from a graphene/h-BN heterostructure showing the typical surface morphology of the sample. The C deposition step for this sample was performed at 730 °C. In the AFM scan of a large area (Figure 6.1a), several micrometer-sized domains with a certain height range are noticeable. Figure 6.1b is a high magnification scan of the dashed square in Figure 6.1a, which clearly shows a region containing such domains. H-BN's thickness inhomogeneities or Ni terraces or a combination of both may have caused these micrometer-sized regions showing the hight contrast. A comparison of these AFM images and the ones obtained from h-BN films grown on Ni films (see Figure 4.2 in Chapter 4) sheds light on some properties of the grown graphene/h-BN

heterostructure. For instance, we can see that the surface of the graphene/h-BN sample (Figure 6.1a) is visibly rougher than that of h-BN (see Figure 4.2 in Chapter 4). The measured RMS roughness of ~2.5 nm in a 1×1 μm^2 of the graphene/h-BN heterostructure is about one order of magnitude higher than the one measured for the h-BN films, which strongly suggests that the graphene film is responsible for the observed roughness. The RMS roughness measured here is comparable to some previous reports for MBE-grown graphene on sapphire,[197] or Ge,[41] however, higher than some other reported values in literature (e.g. on $(6\sqrt{3} \times 6\sqrt{3})$ R 30°-reconstructed SiC surfaces[40] or on sapphire).[42] Furthermore, in the depicted area in Figure 6.1 wrinkles are not observed in the heterostructure film, which might be due to the thick graphene film covering the h-BN and burying possible wrinkles.

Besides the relatively rough surface morphology observed in Figure 6.1, which is representative of a higher portion of the surface (morphology "type I"), regions with significantly different morphology also exist on the surface of the sample (morphologies "type II" and "type III"). The AFM scans of these regions clearly show a network of wrinkles in their structure. Furthermore, these regions generally appear to have a smoother surface (excluding the wrinkles and considering the area between the wrinkles) than the regions of type I. For a better comparison, AFM height and phase scans of areas containing all three morphologies are presented in Figure 6.2. These images were obtained from graphene/h-BN samples, in which the C deposition step was performed at 835 °C (a and b) and ~600 °C (c and d). Cyan and green arrows in Figure 6.2a point out regions with morphologies type II and type III, respectively. In the lower half of the Figure 6.2a, the morphology type I is predominantly seen. These three morphology types also appear different in the corresponding AFM phase images given in Figure 6.2b with brightest contrast generally showing the type I, the darkest contrast showing the type III and the middle contrast pointing out the type II morphology. In the AFM scan from a smaller area given in Figure 6.2c, the smoother character of morphologies type II and III (compared to rougher morphology type I) can be clearly observed. Also it is immediately apparent that the area type II contains a cellular network of short-length wrinkles with high density, while the wrinkles in regions of type III are comparatively longer, smoother and have a lower density. Furthermore, the smooth surface of the regions of type II and specially type III allow observation of some features on the surface (shown by white arrows in Figure 6.2c), which are 4 – 8 nm high and their diameters can be up to ~100 nm.

This observation is important in several perspectives, which are proposed as following: First, it is important to know if graphene has grown on the entire surface of the h-BN film, including the type II and type III regions and, if the answer is positive, which graphene has a better structural quality and the reason for that. If there is no graphene on the regions of type II and III, what happens to the carbon deposited on these regions at such low temperatures (~600 °C), while the neighbor regions (with morphology type I) are clearly covered with a C film. Discussions about the sticking coefficient and the diffusion length of C, as well as the interaction of the C atoms with these different surfaces might then come up. Additionally, it is essential to know the origin of the formation of these three morphologies; whether it is related to the graphene growth process, or it is linked to the growth behavior of h-BN which became noticeable after the graphene film was deposited on h-BN. Probably the most important challenge is then to gain control over the phenomena and to lead it towards the favorable outcome. These are only some examples of questions that arose from the AFM images, which clearly demonstrate the complexity of the topic. Following, it is tried to suggest possible explanations for these observations

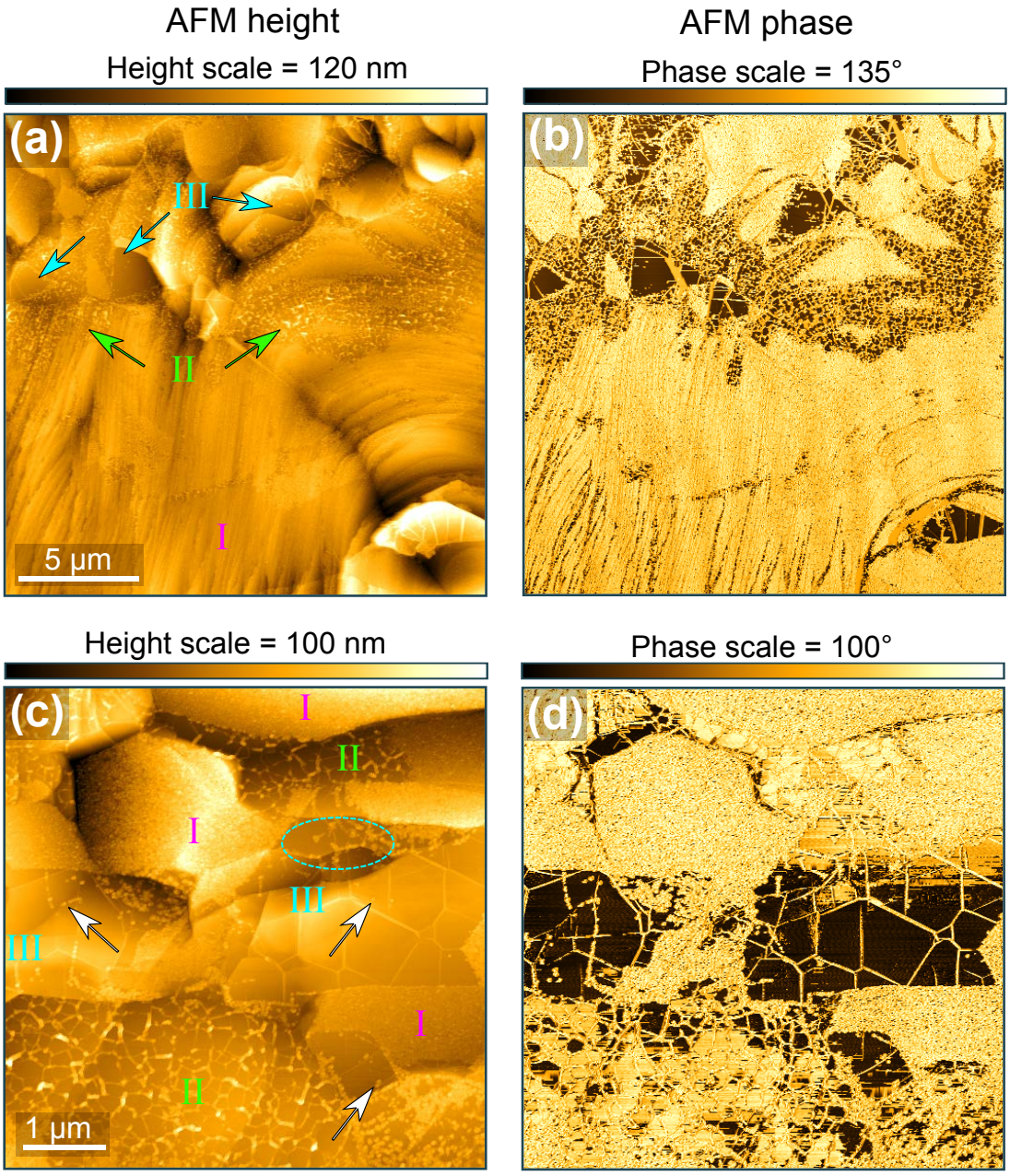

Figure 6.2: AFM height and phase images of graphene/h-BN heterostructures grown on Ni/MgO(111) templates with the C deposition step performed at (a,b) 835 °C and (c,d) ~600 °C. The green and cyan arrows in (a) indicate the regions with morphology type II and III, respectively. The white arrows in (c) point out some C aggregates in regions with morphology type III. The phase images here may only be used as hints to find morphologies type I to III in the respective height images.

based on the findings in this thesis and previous studies. However, further in-depth study and investigations using other characterization techniques are absolutely necessary to answer these questions with more certainty and resolve the complexity.

Before discussing the morphology of the graphene/h-BN heterostructure, it is worth mentioning that the continuity of h-BN in the heterostructures was verified by UV Raman (λ = 244 nm) measurements. Furthermore, Raman spectra (excited at λ = 473 nm)

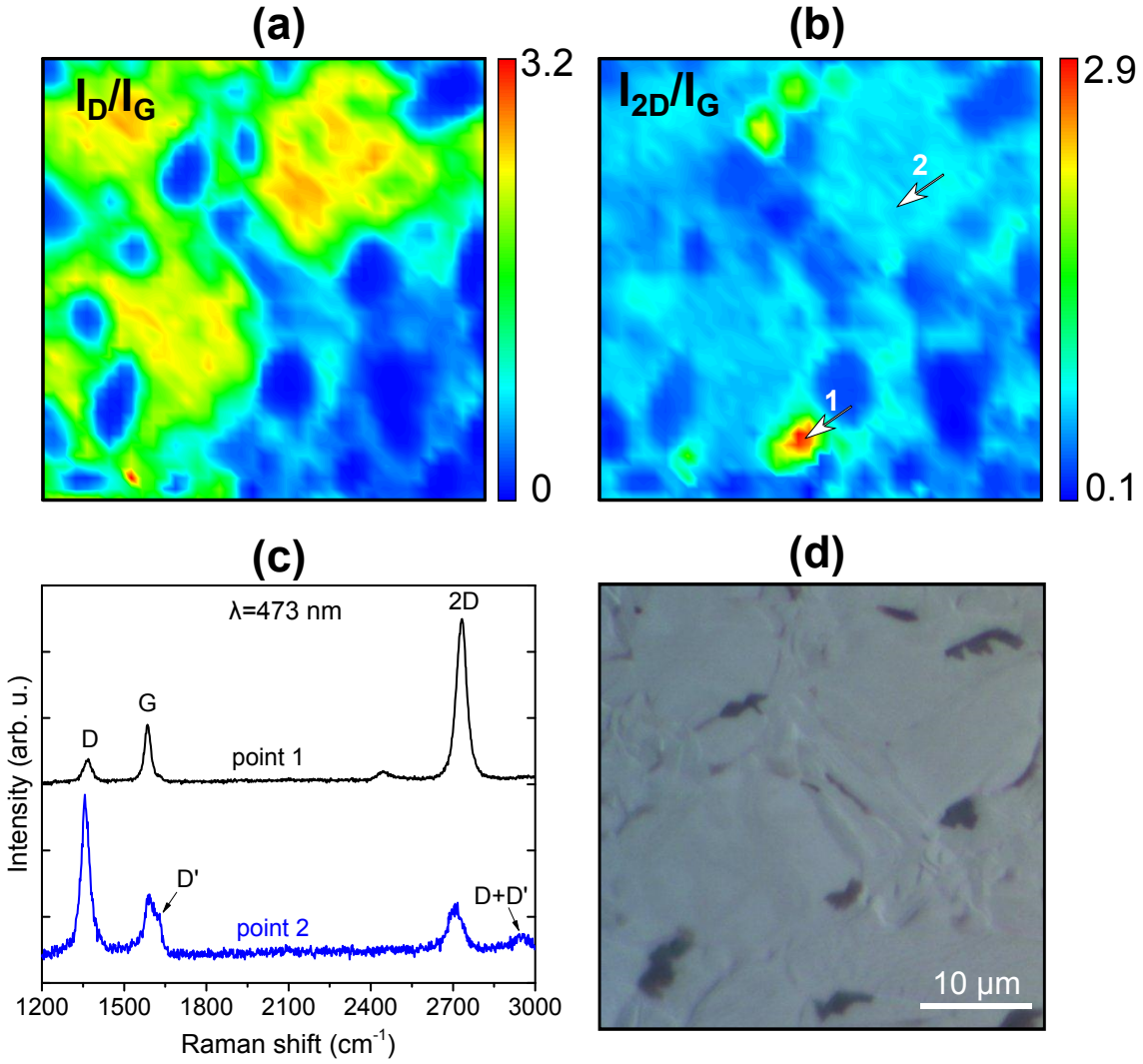

Figure 6.3: (a) Map of the relative intensity of the D peak and the G peak (I_D/I_G), and (b) the 2D peak and the G peak (I_{2D}/I_G) of graphene in a graphene/h-BN heterostructure, in which the C deposition step was performed at ~600 °C. Please note that, the intensity collected for the D peak also contains a negligible contribution of h-BN's E_{2g} peak. Each map consists of 1681 points obtained from a 40 μm × 40 μm area. The wavelength of the excitation laser is 473 nm. (c) displays single Raman spectra of the points which are shown by white arrows in (b). (d) displays the corresponding optical micrograph of the mapped area. The darker regions in the optical image might be thicker regions of graphene, which probably have been formed due to diffusion of C atoms through grain boundaries of h-BN to the Ni and forming graphene under the h-BN.

obtained from the samples discussed in this chapter show the characteristic peaks of graphene (the D, G and 2D peak), indicating that graphene is also present all over the surface. Figure 6.3 displays the map of the relative intensity of the D peak to the G peak (I_D/I_G) as well as the 2D peak to the G peak (I_{2D}/I_G) in a 40 μm × 40 μm area from a graphene/h-BN heterostructure sample in which the C deposition step was performed at ~600 °C. Figure 6.3d shows the optical micrograph of the corresponding mapped area. The maps were obtained using a λ = 473 nm excitation laser with a spot size of ~ 1

µm. Considering the resolution, these results are indicative of a continuous graphene film. Furthermore, these maps also display the local variations in the structural quality of the graphene, which is consistent with the different surface morphologies observed from AFM images given in Figure 6.2. However, finding a direct correlation between the morphologies observed by AFM and the Raman maps appeared to be very challenging due to the lateral resolution of our Raman system. For this purpose a combined Raman-AFM imaging system or tip-enhanced Raman spectroscopy would be more suitable. Figure 6.3c shows two single spectra which are representative of graphene with high (in comparison to nanocrystalline graphene) and low structural quality, which are collected from points 1 and 2 in the mapped area (shown by arrows in Figure 6.3b), respectively. It is worth noting that, although we know a continuous h-BN film with an average thickness of ~ 3 ML forms by utilizing the mentioned h-BN growth parameters, it is not possible to completely rule out the formation of graphene inclusions under the h-BN film. For instance during the C deposition step, some C atoms might have been able to diffuse through the grain boundaries or defects in the h-BN film into the Ni and segregate as graphene islands at the interface of the h-BN and Ni. However, we think this is not the reason for the formation of graphene regions with higher quality (as suggested by Raman spectrum of point 1). Formation of graphene under the h-BN film, alone cannot justify the nonexistence of nanocrystalline graphene on top of h-BN (if there were nanocrystalline graphene on top of h-BN, a much higher I_D/I_G for that region would be expected). Furthermore, low FWHM of the D, G, and 2D peaks (31, 25, and 41 cm^{-1}, respectively) strongly suggests that graphene is present only on one side of the h-BN layer; the superposition of Raman spectra from graphene layers on both sides of the h-BN would lead to wider peaks, due to the peak shifts caused by different environments (i.e. doping and strain). As previously mentioned, the Raman results were mainly presented as confirmation for the continuity of the graphene. Further in-depth investigations (i.e. combined AFM-Raman measurements) are necessary for a better understanding of the topic. More elaborations on Raman spectroscopy measurements for graphene grain size estimation of the nanocrystalline graphene will be presented later in this chapter. Following, the morphology of graphene/h-BN samples will be discussed.

The features shown by white arrows in Figure 6.2c resemble the shape of C clusters, similar to what has been previously observed by other groups in MBE-grown graphene on single crystalline h-BN flakes obtained from mechanical exfoliation.[153,167,205] We would like to choose the nomenclature C "aggregates" as suggested by Summerfield et al.[205] for these features, although the ones observed in this work have smaller physical dimensions. They show that the regions between these aggregates have uniform contrast in high resolution AFM imaging and are fully covered with graphene, such that it is possible to resolve Moiré patterns resulted from the alignment of the graphene and the underlying h-BN lattices. Yet, the reported graphene Raman spectrum in their study resembles the ones typically observed for defective or nanocrystalline graphene. Dabrowski et al.[153] have observed similar aggregates, and suggested distinct h-BN surface defects and impurities as possible sites for their nucleation. They also observe homogeneous AFM height contrast between these aggregates and claim that "in principle it is possible that these regions are covered by a flat graphene film".[153] However, their reported Raman spectrum is also indicative of nanocrystalline graphene. Garcia et al.[167] observed a high density of non-uniform deposited C on h-BN flake edges and also on flat terraces, while some other areas on the h-BN flake was depleted from C. All these studies share the advantage that, in principle they benefit from the atomically smooth surface of single

crystalline h-BN flakes as growth substrate. We also speculate that the difference observed between the morphologies of the regions type I to III might have originated from variations in crystalline perfection and smoothness of the corresponding underlying h-BN; regions of type II and III have smoother surface and better crystalline quality than type I. With this assumption it is possible to explain the observed phenomena as following: Dabrowski et al.[153] suggest that the smallest h-BN surface imperfections, such as a mono-atomic h-BN step, promote the graphene nucleation and growth. This argument best explains the morphology type I, where the underlying h-BN has a rougher (highly corrugated) surface, probably due to the high density of step edge clusters of the Ni under it. This leads to a high density of nucleation centers for the impinged C atoms to form a graphene film. This scenario is different if we assume that the underlying h-BN in the regions type II and III has a smoother surface and with less defects as compared to the region type I. Dabrowski et al.[153] found, based on DFT calculations, that the energy barrier for the desorption of C ad-atoms from *perfect* h-BN is low, and just slightly higher than the energy barrier to overcome for diffusion. In the other words, C has a very small effective sticking coefficient on a perfect h-BN surface. Furthermore, Plaut et al.[150] have observed that C atoms have a migration length of more than 100 µm on the flat surface of a single crystal h-BN flake, such that part of the adsorbed C ad-atoms spill off the edge of the flake, and only a very small portion of adsorbed atoms remain on h-BN surface (in the reported case, the ratio of remaining C atoms on h-BN flake to the ones on the supporting SiO_2 substrate was 3–5% at a growth temperature of ~500 °C). Based on these studies, we can conclude that if the regions type II and II have smoother surface and a higher crystalline quality, the desorption of C atoms is higher than for the regions of type I. Moreover, the adsorbed C atoms on regions II and III tend to migrate long distances until they they reach type I regions, where there are more energetically preferred sites to incorporate into graphene nucleation seeds. This might also be the reason to observe the C aggregates with less density on regions of type II and III. Figure 6.2c also shows that the C aggregates in regions of type III are typically less abundant where the h-BN lies on top of a smooth Ni terrace, and more abundant where h-BN crosses a Ni grain boundary (for instance in the region shown by cyan dashes in Figure 6.2). This also corroborates the explanation given above. In other words, the C aggregates can be also formed in regions of morphology type II and III, where the surface energy is changed due to roughness (here for instance where h-BN expands over Ni grain boundaries).

Thickness variation of the underlying h-BN may also be an explanation for the different morphologies observed in Figure 6.2. The morphologies type II and III are speculated to be correlated to the regions where the h-BN layer under graphene is thinner (single h-BN layer), while a thicker (i.e. few-layer) h-BN film lies under the regions with the morphology type I. The metal under the thin, or more specifically one monolayer thick h-BN might still influence the graphene growth behavior, for instance, by affecting the chemical potential of the h-BN surface. This influence is screened when a thicker h-BN layer acts as the growth substrate. Although proof of this hypothesis was not found, there are some examples of experimental observations reported by other groups which support this hypothesis. The situation is better known for the case of graphene on metals.[206] For instance Zuo et al.[86] claimed improvement in MBE-grown h-BN on thinner graphene supported by cobalt, as compared to thicker graphene. Nagashima et al.[207] observed a weakening of metal d orbitals and graphene π orbitals hybridization upon the growth of second graphene layer on top of the first one, indicating an interaction between the metal and the second graphene layer which is not completely screened by the first graphene

layer. In other words, they experimentally show that the interaction between the first and the second graphene layer on a metal is different from the van der Waals interaction (as expected between graphite layers), which is related to the influence of the underlying metal not being completely screened, even when covered by a monolayer graphene. For the case of epitaxial monolayer h-BN on Ni(111), based on DFT calculations Tonkikh et al.[137] report the overlapping of h-BN's π orbitals and the Ni 3d states leading to a metallic character of monolayer h-BN on Ni(111). While such strong interaction between a monolayer h-BN and Ni affecting the growth of graphene on h-BN is probable, yet additional experimental observations are needed to confirm it.

Until here, the suggested explanations for the formation of morphologies type I to III were based on the assumption that h-BN film acting as the substrate for graphene growth can have different characters: smooth h-BN surface versus a rougher one, or thin (i.e. single) h-BN layer versus few-layer h-BN. In fact previous studies also observed the coexistence of h-BN layers with different character within a grown h-BN film. Yang et al.[178] have experimentally observed the simultaneous formation of two types of h-BN ad-layers on top of Ni(111): a weakly interacting h-BN with Ni (h-BN_{nonepi}), and a strongly interacting h-BN with Ni(111) for h-BN which is epitaxially aligned with Ni(111) (h-BN_{epi}). Besides the different growth rate and work function, these ad-layers have also different separation to Ni substrate, with the calculated value of 2.9 Å for h-BN_{nonepi}, and 2.0 Å for h-BN_{epi} which is also in very good agreement with the reported value obtained from cross sectional TEM[137] of epitaxial h-BN on Ni(111). They further observed that while h-BN_{nonepi} allows the propagation of another h-BN_{nonepi} on top or under it, h-BN_{epi} only allows the growth of h-BN_{nonepi} on top of it. In other words, the few-layer h-BN regions have always h-BN_{nonepi} on the topmost surface. We suggest that the morphologies of type II and III are the regions where graphene is forming on h-BN monolayers which are strongly interacting with Ni, while the morphology type I is correlated to graphene forming on multilayer h-BN and/or weakly interacting h-BN with Ni. It is also speculated that the morphologies type II and III are different in the way that in type III the underlying monolayer h-BN is formed on a large and flat terrace of Ni, while the h-BN in the regions of morphology type II is formed where the underlying Ni has a higher density of step edge clusters and shorter terraces. This promotes a higher density of wrinkles in h-BN formed in regions type II (see also Figure 4.2 and the related discussion in Chapter 4). Please note that, for the samples studied here, the assumption of having two different types of h-BN ad-layers is consistent with our XPS observations. Figure 5.7b and c in Chapter 5 show that the N1s and the B1s core-level spectra of h-BN are composed of two components, suggesting the coexistence of strongly and weakly interacting h-BN ad-layers with Ni, and also consistent with the XPS results of Yang et al.[178] However, as previously mentioned, confirming these explanations necessitates further investigations to collect additional experimental evidence.

6.3 Estimation of average graphene domain size

As it was shown in previous section in Figure 6.3, the graphene film grown on top of h-BN exhibited a variation in its structural quality ranging from a defective or nanocrystalline graphene to a comparatively higher quality film with less structural defects. In this section, we present an investigation of the nature of structural defects in graphene grown on h-BN films. In order to discuss the topic in more details, we put the focus on a

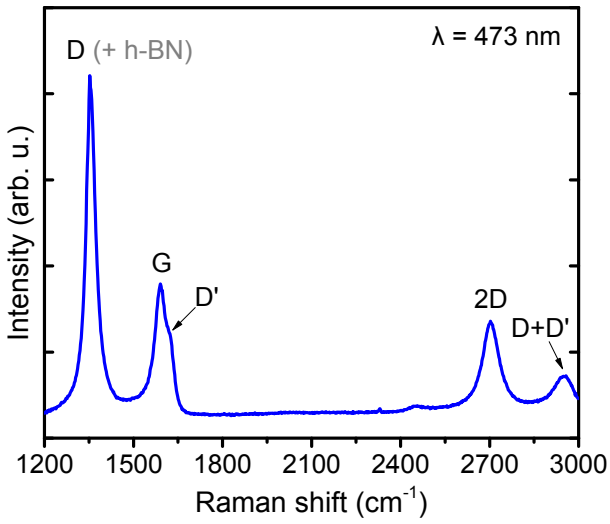

Figure 6.4: Raman spectrum obtained from a graphene/h-BN heterostructure in which the C deposition step was performed at 730 °C.

single Raman spectrum, typical of a defective region, which was obtained with optimized Raman acquisition settings to minimize the noise. This allowed for very accurate fitting of the Raman peaks, which is necessary for this study. The Raman acquisition time and the laser power were chosen in a way that the sample is not damaged. A representative Raman spectrum obtained from a graphene/h-BN sample (C deposition step performed at 730 °C) using the a λ = 473 nm excitation wavelength is presented in Figure 6.4. The Raman spectrum clearly shows the characteristic peaks of graphene, namely the G peak at ~1590 cm^{-1} and the 2D peak at ~2700 cm^{-1} as well as a relatively high defect-induced D at ~1350 cm^{-1} and D' at ~1620 cm^{-1}, indicative of defective sp^2-bonded C or nanocrystalline graphene.[42] The combined D+D' mode[99] is also observed at ~2950 cm^{-1} in the spectrum. Please note that the feature at ~1350 cm^{-1} also contains a very small contribution of h-BN (at ~1365 cm^{-1}), which is negligible compared to the high intensity D peak observed there (for more details see also Figure 5.3 in Chapter 5 and the corresponding discussion).

As previously mentioned, the D peak is related to the defects in graphene lattice and is not observed in a perfect hexagonal sp^2-bonded C lattice.[99] This peak is associated to the breathing mode of the hexagonal C rings,[208] and only activated once defects (e.g. crystal edge, point defects or grain boundaries) are present. The relative intensity of the D peak to the G peak (I_D/I_G) is commonly used in literature to describe the crystalline quality of graphene layers.[99] Ferrari and Robertson[208] suggest three stages for amorphization trajectory of C materials ranging from perfectly sp^2-bonded C (as stage one) to amorphous carbons (stage three), and explain the evolution of Raman spectrum for each stage. According to their study, in stage one, first a D peak appears, the I_D/I_G increases, the D' peak appears, all the peaks start to broaden, D +D' peak appears, and finally the G and D' peak become so wide that it is more convenient to consider them as a single blue shifted wide G peak at ~1600 cm^{-1}. Based on this classification, the sample discussed here lies within the first stage of amorphization trajectory[208] described above, as the G peak maximum is observed at ~1590 cm^{-1} and the D' is distinguished as a shoulder to the G peak at ~1620 cm^{-1} in Figure 6.4. Thus, based on the Raman features observed in Fig-

ure 6.4 it is possible to call the MBE-grown graphene film obtained in most of the regions "nanocrystalline graphene", which is also consistent with previous studies.[42] With this definition, it is meaningful to have an estimation of the average grain size of the grown graphene film.

Various ongoing studies aim at quantifying defects based on Raman fingerprints of graphene[99,101] (from many others). Among these studies, some were able develop models to estimate the average grain size (or domain size) of nanocrystalline graphene, however by considering that grain boundaries are the *only* defects present in the film. Therefore, one should pay especial attention for using these models, since other types of disorder such as vacancies or sp^3-hybridized C may also be present which influence the obtained Raman spectra. For instance, Cançado et al.[209,210] proposed an empirical model that considers the relative integrated intensities of the D and G peak (A_D/A_G), as well as the D' and G peak ($A_{D'}/A_G$) to estimate the average domain size, L_a, as following:

$$L_a(nm) = \frac{560}{E_l^4}\left(\frac{A_D}{A_G}\right)^{-1} \tag{6.1}$$

and

$$L_a(nm) = \frac{160}{E_l^4}\left(\frac{A_{D'}}{A_G}\right)^{-1} \tag{6.2}$$

where E_l is the excitation laser energy, which is 2.62 eV in our case. For the sample discussed here (C deposition performed at 730 °C), Equations 6.1 and 6.2 result in different average domain size of ~6 nm and ~27 nm, respectively. The discrepancy observed for the calculated values strongly suggests that this model may not be used for calculation of the average domain size of the sample studied here, as the grain boundaries are not the only existing defects in the grown graphene film. In other words, this model will give consistent results only if:

$$\frac{A_D}{A_{D'}} = \frac{560}{160} = 3.5 \tag{6.3}$$

which is different than the respective calculated value of ($A_D/A_{D'}$)~14 for the sample discussed here.

Eckmann et al.[102] suggest that the ratio between the D and D' peak intensity ($I_D/I_{D'}$) informs about the type of the defects present in graphene. According to their study, this intensity ratio is highest, ~13, for sp^3-hybridization sites, it decreases to ~7, for vacancy-like defects, and ~3.5 for grain boundaries. For the sample discussed here, this ratio $I_D/I_{D'}$, is ~8, indicating that also the vacancy-like defects notably give rise to the defect-induced peaks. This further supports the argument why the mentioned model (Equations 6.1 and 6.2) might not be applicable for the sample studied here.

Another proposed empirical model,[210] which is also established based on samples containing grain boundaries as defects, estimates the average grain size based on the width (Γ or FWHM) of the Raman peaks as following:

$$\Gamma = C_1 + \frac{C_2}{L_a} \tag{6.4}$$

where C_1 (cm^{-1}) and C_2 (cm^{-1}.nm) are constants, which take different values depending on the peak that is considered for the calculation.[210] Using the Equation 6.4 and considering the widths of the D, 2D , G, and D' peak the average grain size is calculated to be ~25 nm, ~24 nm, ~30 nm, and ~17 nm, respectively. Besides the limitation inherent to the

model, which considers grain boundaries as defects causing the widening of the peaks, the difference observed for the calculated average grain size values using the width of the G and D' peak could have arisen from the uncertainty in peak fittings, due to closely located G and D' in the spectrum.

The discussion above can be summarized as following: the average domain size of graphene was estimated based on the two existing empirical models in literature. These models correlate the graphene average grain size with the width and integrated intensity of graphene Raman features, and were established based on samples which contain only grain boundaries as defects in graphene. However, other types of defect such as point defects, sp^3-hybridized C or inhomogeneous strain also affect Raman features of graphene. In the graphene sample studied here, based on Raman studies, we know that at least two of these defect types, namely grain boundaries and point defects, are present. Thus, the average grain size calculated based on these empirical models offers a lower estimate of the actual value.

The typically observed Raman spectra obtained from defective graphene regions of the samples, in which the C deposition step was performed at 835 °C and ~600 °C were not noticeably different from the one discussed above. A possible explanation could be that in the chosen temperature range, the C surface diffusion was not sufficiently manipulated, in a way that affects the defect concentration in graphene, as estimated by Raman spectroscopy.

Additionally, the growth experiments, in which the substrate temperature was raised to ~860 °C for the C deposition step (taking 10 minutes) have been performed. However, keeping the templates even for this short period at high temperatures led to expansion of the pits in Ni followed by dewetting of the Ni film on MgO(111) substrate. Furthermore, Raman measurements show no evidence of the presence of graphene even on remaining Ni film on the MgO(111). This might be related to the high desorption rate expected at higher temperatures or even dissolution of C in exposed Ni, probably due to the rapid change of the Ni surface.

6.4 Summary and conclusions

As the main goal of this chapter, the feasibility of the synthesis of graphene from a solid source of C on top of the large-area MBE-grown h-BN has been demonstrated. The uninterrupted observation of graphene's characteristic Raman peaks in numerous Raman measurements and mappings indicate the formation of a continuous graphene film over the entire substrate. The continuity of the h-BN was likewise confirmed using a UV excitation laser for Raman experiments.

A careful examination of graphene/h-BN heterostructures by AFM, revealed that their surface consisted of three different morphologies, namely type I to III. The more frequently observed morphology type I appears rougher than the ones of type II and III. Also, wrinkles could only be observed in regions with morphology type II and III. Although a clear understanding of the origin of the observed morphologies remains as a topic of future investigations, two possible explanations based on the findings in this thesis and previous studies have been offered, which are summarized as following: a) By assuming that the underlying h-BN in the regions of type II and III are smoother and/or have less crystalline disorder than the regions of type I. Based on previous studies, using the surface of h-BN with high crystalline quality will lead to a lower sticking coefficient of C atoms, lower density of nucleation sites, as well as long migration lengths of C ad-

atoms on the surface, which might result in a smoother morphology of the graphene/h-BN in regions of type II and III. b) The underlying h-BN in the regions of type II and III are monolayer h-BN having high interaction with Ni, while the regions type I are few layer or weakly interacting h-BN with the Ni. The incomplete screening of the monolayer h-BN/metal interaction might have had influence on the chemical potential of the h-BN surface, which led to a different growth behavior of graphene in regions type II and III. Besides demonstrating the complexity of the topic, these results clearly show the potential playground for future research efforts, which need to be devoted, in order to understand and gain control over the growth behavior of graphene/h-BN heterostructures using MBE.

As a consensus among various studies, in general, utilizing a smooth substrate and enhancement of C ad-atom diffusion length through increasing the growth temperature are the key factors to improve the quality of large-area MBE-grown graphene on dielectrics. However, every choice of substrate, currently being tested, imposes constraints on achieving these ideal conditions for wafer-scale growth of graphene using MBE. For instance, melting of the substrates[41], local[199,201] or complete decomposition[167,200,211], or chemical reaction with C[212] are counted as restrictions for utilizing very high temperatures. The results presented in this chapter suggest that obtaining a better quality graphene by direct deposition of C on h-BN is feasible at temperatures as low as ~600 °C. On the other hand, vacancy-like defects are responsible for a high portion of disorder in the graphene film, as discussed in this chapter based on Raman measurements. A recent study[201] suggest that the number of vacancy-like defects can be considerably reduced by introducing Ni as a surfactant, which is co-deposited with C, leading to further improvement of the quality of graphene film. In general, the results presented in this chapter, display the suitability of MBE as a growth technique for large-area graphene/h-BN heterostructures and open pathways for the future work towards a more controlled growth of this heterostructure.

7 Conclusions and outlook

In this chapter, a summary of the results obtained in the thesis is provided. Additionally, suggestions for future experiments are given.

Conclusions

This thesis focuses on the growth of large-area h-BN and stacked heterostructures of graphene and h-BN by means of MBE. The grown films were investigated using various characterization techniques to learn about their structural quality as well as growth behavior.

Initially the feasibility of the synthesis of h-BN on Ni foils from elemental sources of B and N was demonstrated. Growth parameters which result in the formation of a continuous h-BN film were found. Utilization of these parameters led to the growth of an atomically thin h-BN film with an average thickness of ~3 ML, as estimated by XRR and AFM profilometry. An SEM study of the films obtained from shorter growth durations shows that the morphology of developing h-BN evolved from star-shape to larger, smooth triangular islands with increasing growth temperature. Observing small points of high contrast at the approximate geometric centers of the islands in SEM images indicates that the h-BN nucleated heterogeneously.

In order to gain more insight, further growth experiments were performed utilizing thin Ni films deposited on MgO(111) substrates as the growth template. Reproducing the previous growth parameters on Ni/MgO(111) templates resulted in h-BN films with slightly better quality, as confirmed by AFM and Raman spectroscopy. The average lattice parameter of h-BN, measured by GID experiments, shows that the synthesized film is ~1% compressively strained, likely due to the thermal contraction of Ni in contact with h-BN during cooling down from the growth temperature. Replicating these growth parameters at a lower temperature led to the formation of a h-BN film with lower structural quality, as confirmed by Raman spectroscopy. AFM scans obtained from this sample additionally display the formation of some particles on the h-BN film, which are speculated to be BN nanoparticles. By systematic variation of the substrate temperature in shorter growth durations, I could shed some light on the nucleation and growth behavior of h-BN on thin Ni films. Enhancement of ad-atom diffusion and a decrease in sticking coefficients of B and N upon increasing the growth temperature were evoked to explain the origin of preferred nucleation sites, size of the crystallites, and h-BN coverage. These results additionally demonstrate the significance of a high-quality and smooth Ni surface for gaining better control over the thickness homogeneity of h-BN films grown by MBE.

Large area growth of h-BN/graphene vertical heterostructures (h-BN on graphene) was demonstrated by employing a novel MBE-based technique, which allows both h-BN and graphene to form in the favorable growth environment provided by Ni. In this hybrid technique, graphene forms via the precipitation of C atoms previously dissolved in the thin Ni film, after the h-BN is directly grown on the exposed Ni surface. The continuity of h-BN and graphene films were verified using Raman spectroscopy. Additionally, the suitability of UV Raman spectroscopy for the characterization of h-BN/graphene

heterostructures was demonstrated. Formation of a continuous graphene film at the interface between h-BN and Ni indicates stronger graphene/Ni bonding than h-BN/Ni bonding, consistent with previous studies. GID experiments on h-BN/graphene heterostructures show that the h-BN film is strain-free, while the graphene lattice is by ~4% compressively strained. Observation of strain-free h-BN is consistent with its decoupling from Ni upon formation of graphene at their interface. While the contraction of Ni in contact with graphene during cooling can be responsible for a portion of the compressive strain in graphene, N incorporation in graphene lattice is likely the main reason for the reduction of its average lattice parameter. This is consistent with the observed doping-induced shifts in graphene Raman peaks and the results obtained from XPS studies. The transition from two-component core level spectra (B1s and N1s) obtained from h-BN on Ni, to single-component ones obtained from h-BN/graphene heterostructures in XPS measurements, is further evidence of graphene formation at h-BN/Ni interface.

Finally, large-area synthesis of graphene/h-BN vertical heterostructures (graphene on h-BN) has been demonstrated to be feasible by the direct deposition of C atoms on top of MBE-grown h-BN. Presence of graphene and h-BN over the entire heterostructure was confirmed using Raman spectroscopy utilizing visible and UV excitation wavelengths. A careful examination of graphene/h-BN heterostructures by AFM revealed that the surface consisted of three morphology types. A clearer understanding of the origin of the observed morphologies remained as a topic of future investigations. However, based on previous findings in this thesis and earlier studies, I could offer two possible explanations for the newly obtained preliminary results. These explanations consider the thickness inhomogeneity and variation in structural quality of the underlying h-BN film. Mapping the characteristic Raman peaks of graphene over a large-area showed that the structural quality of graphene varies in a range from graphene with relatively good structural quality (compared to what is typically seen for graphene grown on dielectrics) to nanocrystalline graphene. The average grain size of nanocrystalline graphene was estimated based on two empirical models in literature. Furthermore, it was found that vacancy-like defects are mainly responsible for a high portion of disorder in nanocrystalline graphene.

Outlook

The results obtained for the growth of h-BN on Ni films demonstrated the significance of a Ni surface on controlling the thickness homogeneity of h-BN films. For more detailed fundamental studies of nucleation and growth, as well as a better control over the thickness homogeneity, utilization of a single crystalline Ni substrate with a very smooth surface would be especially advantageous. It was found that the growth of h-BN overlayers fade the surface features of the underlying substrate. Faster growth of thicker and smoother h-BN films on Ni is anticipated to be facilitated by employing an e-beam evaporator for producing a higher B flux.

Availability of a higher B flux allows examining the growth of h-BN on dielectric surfaces. Sapphire substrates can be particularly interesting because of their stability at high temperatures, feasibility of epitaxial h-BN growth due to their similar hexagonal lattice, and their large and atomically smooth terraces. The h-BN grown on sapphire substrates can be used as growth templates for graphene synthesis using the direct deposition of C atoms. Extremely high growth temperatures allowed by these templates may lead to formation of graphene with higher structural quality. Additionally, it is known that H atoms can etch the unorganized or defective edges of graphene grown by CVD.[213] Therefore, it

is worth examining the effect of introducing a H flux (during the deposition of C atoms) on the quality of the MBE-grown graphene films.

Another approach to the synthesis of h-BN/graphene vertical heterostructures over large areas is to employ epitaxial graphene formed on the surface of SiC substrates as the growth template. Monolayer graphene films can be grown on the Si-face of SiC substrates by depletion of Si atoms from the surface at hight temperatures. Ongoing experiments regarding the growth of h-BN on these substrates show very promising results.[214] Additionally, other substrates such as thicker graphene layers obtained on C-face of SiC substrates or quasi-free-standing bilayer graphene produced by air annealing of monolayer graphene on the Si-face of SiC substrates[149] can be considered as templates for h-BN synthesis.

Finally, the results obtained from graphene/h-BN heterostructures displayed variations in their surface morphology. Also, the graphene film was shown to consist of regions with different structural quality. Further investigations such as tip-enhanced Raman spectroscopy or a combined AFM-Raman characterization can help correlating these variations in surface morphology with graphene quality. Once a correlation is found, the next step is to gain control over the synthesis of heterostructures with desired morphology or graphene quality.

Bibliography

[1] E. Fitzer, K.-H. Kochling, H. P. Boehm, and H. Marsh, *Recommended terminology for the description of carbon as a solid (IUPAC Recommendations 1995)*, Pure Appl. Chem. 473–506 (1995).

[2] A. K. Geim and K. S. Novoselov, *The rise of graphene*, Nat. Mater. **6**, 183–191 (2007).

[3] P. R. Wallace, *The Band Theory of Graphite*, Phys. Rev. **71**, 622–634 (1947).

[4] H. P. Boehm., A. Clauss, G. O. Fischer, and U. Hofmann, *Dünnste Kohlenstoff-Folien*, Zeitschrift für Naturforsch. B **17**, 150–153 (1962).

[5] J. C. Shelton, H. R. Patil, and J. M. Blakely, *Equilibrium segregation of carbon to a nickel (111) surface: A surface phase transition*, Surf. Sci. **43**, 493–520 (1974).

[6] A. J. Van Bommel, J. E. Crombeen, and A. Van Tooren, *LEED and Auger electron observations of the SiC(0001) surface*, Surf. Sci. **48**, 463–472 (1975).

[7] C. Oshima and A. Nagashima, *Ultra-thin epitaxial films of graphite and hexagonal boron nitride on solid surfaces*, J. Phys. Condens. Matter 1–20 (1997).

[8] K. S. Novoselov, A. K. Geim, S. V. Morozov, D. Jiang, Y. Zhang, S. V. Dubonos, I. V. Grigorieva, and A. A. Firsov, *Electric Field Effect in Atomically Thin Carbon Films*, Science **306**, 666–669 (2004).

[9] K. I. Bolotin, K. J. Sikes, Z. Jiang, M. Klima, G. Fudenberg, J. Hone, P. Kim, and H. L. Stormer, *Ultrahigh electron mobility in suspended graphene*, Solid State Commun. 351–355 (2008).

[10] S. V. Morozov, K. S. Novoselov, M. I. Katsnelson, F. Schedin, D. C. Elias, J. A. Jaszczak, and A. K. Geim, *Giant Intrinsic Carrier Mobilities in Graphene and Its Bilayer*, Phys. Rev. Lett. 016602 (2008).

[11] J. Moser, A. Barreiro, and A. Bachtold, *Current-induced cleaning of graphene*, Appl. Phys. Lett. 163513 (2007).

[12] C. Lee, X. Wei, J. W. Kysar, and J. Hone, *Measurement of the Elastic Properties and Intrinsic Strength of Monolayer Graphene*, Science **321**, 385–388 (2008).

[13] C. Lee, X. Wei, Q. Li, R. Carpick, J. W. Kysar, and J. Hone, *Elastic and frictional properties of graphene*, Phys. status solidi **246**, 2562–2567 (2009).

[14] J. H. Seol, I. Jo, A. L. Moore, L. Lindsay, Z. H. Aitken, M. T. Pettes, X. Li, Z. Yao, R. Huang, D. Broido, N. Mingo, R. S. Ruoff, and L. Shi, *Two-Dimensional Phonon Transport in Supported Graphene*, Science **328**, 213–216 (2010).

[15] A. A. Balandin, S. Ghosh, W. Bao, I. Calizo, D. Teweldebrhan, F. Miao, and C. N. Lau, *Superior Thermal Conductivity of Single-Layer Graphene*, Nano Lett. **8**, 902–907 (2008).

[16] R. R. Nair, P. Blake, A. N. Grigorenko, K. S. Novoselov, T. J. Booth, T. Stauber, N. M. R. Peres, and A. K. Geim, *Fine Structure Constant Defines Visual Transparency of Graphene*, Science **320**, 1308–1308 (2008).

[17] K. S. Novoselov, V. I. Fal'ko, L. Colombo, P. R. Gellert, M. G. Schwab, and K. Kim, *A roadmap for graphene*, Nature 192–200 (2012).

[18] V. Singh, D. Joung, L. Zhai, S. Das, S. I. Khondaker, and S. Seal, *Graphene based materials: Past, present and future*, Prog. Mater. Sci. 1178–1271 (2011).

[19] A. H. Castro Neto, F. Guinea, N. M. R. Peres, K. S. Novoselov, and A. K. Geim, *The electronic properties of graphene*, Rev. Mod. Phys. 109–162 (2009).

[20] S. Reich, J. Maultzsch, C. Thomsen, and P. Ordejón, *Tight-binding description of graphene*, Phys. Rev. B **66**, 035412 (2002).

[21] R. S. Deacon, K.-C. Chuang, R. J. Nicholas, K. S. Novoselov, and A. K. Geim, *Cyclotron resonance study of the electron and hole velocity in graphene monolayers*, Phys. Rev. B **76**, 081406 (2007).

[22] K. S. Novoselov, A. K. Geim, S. V. Morozov, D. Jiang, M. I. Katsnelson, I. V. Grigorieva, S. V. Dubonos, and A. A. Firsov, *Two-dimensional gas of massless Dirac fermions in graphene*, Nature **438**, 197–200 (2005).

[23] M. Eizenberg and J. M. Blakely, *Carbon monolayer phase condensation on Ni(111)*, Surf. Sci. **82**, 228–236 (1979).

[24] P. R. Somani, S. P. Somani, and M. Umeno, *Planer nano-graphenes from camphor by CVD*, Chem. Phys. Lett. **430**, 56–59 (2006).

[25] A. N. Obraztsov, E. A. Obraztsova, A. V. Tyurnina, and A. A. Zolotukhin, *Chemical vapor deposition of thin graphite films of nanometer thickness*, Carbon **45**, 2017–2021 (2007).

[26] A. Reina, X. Jia, J. Ho, D. Nezich, H. Son, V. Bulovic, M. S. Dresselhaus, and J. Kong, *Large Area, Few-Layer Graphene Films on Arbitrary Substrates by Chemical Vapor Deposition*, Nano Lett. **9**, 30–35 (2009).

[27] X. Li, W. Cai, J. An, S. Kim, J. Nah, D. Yang, R. Piner, A. Velamakanni, I. Jung, E. Tutuc, S. K. Banerjee, L. Colombo, and R. S. Ruoff, *Large-area synthesis of high-quality and uniform graphene films on copper foils*, Science **324**, 1312–1314 (2009).

[28] Y. Lee, S. Bae, H. Jang, S. Jang, S.-E. Zhu, S. H. Sim, Y. I. Song, B. H. Hong, and J.-H. Ahn, *Wafer-Scale Synthesis and Transfer of Graphene Films*, Nano Lett. 490–493 (2010).

[29] J. C. Hamilton and J. M. Blakely, *Carbon segregation to single crystal surfaces of Pt, Pd and Co*, Surf. Sci. **91**, 199–217 (1980).

[30] J. Coraux, A. T. N'Diaye, C. Busse, and T. Michely, *Structural Coherency of Graphene on Ir(111)*, Nano Lett. 565–570 (2008).

[31] H. Zi-Pu, D. F. Ogletree, M. A. Van Hove, and G. A. Somorjai, *Leed theory for incommensurate overlayers: Application to graphite on Pt(111)*, Surf. Sci. 433–459 (1987).

[32] T. A. Land, T. Michely, R. J. Behm, J. C. Hemminger, and G. Comsa, *STM investigation of single layer graphite structures produced on Pt(111) by hydrocarbon decomposition*, Surf. Sci. 261–270 (1992).

[33] G. Odahara, S. Otani, C. Oshima, M. Suzuki, T. Yasue, and T. Koshikawa, *In-situ observation of graphene growth on Ni(111)*, Surf. Sci. **605**, 1095–1098 (2011).

[34] X. Li, W. Cai, L. Colombo, and R. S. Ruoff, *Evolution of Graphene Growth on Ni and Cu by Carbon Isotope Labeling*, Nano Lett. **9**, 4268–4272 (2009).

[35] K. S. Kim, Y. Zhao, H. Jang, S. Y. Lee, J. M. Kim, K. S. Kim, J.-H. Ahn, P. Kim, J.-Y. Choi, and B. H. Hong, *Large-scale pattern growth of graphene films for stretchable transparent electrodes*, Nature **457**, 706–710 (2009).

[36] S. Bhaviripudi, X. Jia, M. S. Dresselhaus, and J. Kong, *Role of Kinetic Factors in Chemical Vapor Deposition Synthesis of Uniform Large Area Graphene Using Copper Catalyst*, Nano Lett. **10**, 4128–4133 (2010).

[37] C. Berger, Z. Song, T. Li, X. Li, A. Y. Ogbazghi, R. Feng, Z. Dai, A. N. Marchenkov, E. H. Conrad, P. N. First, and W. A. de Heer, *Ultrathin Epitaxial Graphite: 2D Electron Gas Properties and a Route toward Graphene-based Nanoelectronics*, J. Phys. Chem. B 19912–19916 (2004).

[38] K. V. Emtsev, A. Bostwick, K. Horn, J. Jobst, G. L. Kellogg, L. Ley, J. L. McChesney, T. Ohta, S. A. Reshanov, J. Röhrl, E. Rotenberg, A. K. Schmid, D. Waldmann, H. B. Weber, and T. Seyller, *Towards wafer-size graphene layers by atmospheric pressure graphitization of silicon carbide*, Nat. Mater. **8**, 203–207 (2009).

[39] J. M. Wofford, M. H. Oliveira, T. Schumann, B. Jenichen, M. Ramsteiner, U. Jahn, S. Fölsch, J. M. J. Lopes, and H. Riechert, *Molecular beam epitaxy of graphene on ultrasmooth nickel: growth mode and substrate interactions*, New J. Phys. **16**, 093055 (2014).

[40] T. Schumann, M. Dubslaff, M. H. Oliveira, M. Hanke, F. Fromm, T. Seyller, L. Nemec, V. Blum, M. Scheffler, J. M. J. Lopes, and H. Riechert, *Structural investigation of nanocrystalline graphene grown on ($6\sqrt{3} \times 6\sqrt{3}$) R 30°-reconstructed SiC surfaces by molecular beam epitaxy*, New J. Phys. **15**, 123034 (2013).

[41] G. Lippert, J. Dabrowski, T. Schroeder, M. A. Schubert, Y. Yamamoto, F. Herziger, J. Maultzsch, J. Baringhaus, C. Tegenkamp, M. C. Asensio, J. Avila, and G. Lupina, *Graphene grown on Ge(001) from atomic source*, Carbon **75**, 104–112 (2014).

[42] M. H. Oliveira, T. Schumann, R. Gargallo-Caballero, F. Fromm, T. Seyller, M. Ramsteiner, A. Trampert, L. Geelhaar, J. M. J. Lopes, and H. Riechert, *Mono- and few-layer nanocrystalline graphene grown on Al_2O_3(0001) by molecular beam epitaxy*, Carbon **56**, 339–350 (2013).

[43] P. B. Mirkarimi, K. F. McCarty, and D. L. Medlin, *Review of advances in cubic boron nitride film synthesis*, Mater. Sci. Eng. R Reports **21**, 47–100 (1997).

[44] R. S. Pease, *An X-ray study of boron nitride*, Acta Crystallogr. **5**, 356–361 (1952).

[45] A. Pakdel, Y. Bando, and D. Golberg, *Nano boron nitride flatland.*, Chem. Soc. Rev. **43**, 934–59 (2014).

[46] W. Paszkowicz, J. B. Pelka, M. Knapp, T. Szyszko, and S. Podsiadlo, *Lattice parameters and anisotropic thermal expansion of hexagonal boron nitride in the 10 – 297.5 K temperature range*, Appl. Phys. A Mater. Sci. Process. **75**, 431–435 (2002).

[47] C.-J. Kim, L. Brown, M. W. Graham, R. Hovden, R. W. Havener, P. L. McEuen, D. A. Muller, and J. Park, *Stacking order dependent second harmonic generation and topological defects in h-BN bilayers*, Nano Lett. **13**, 5660–5665 (2013).

[48] G. Constantinescu, A. Kuc, and T. Heine, *Stacking in Bulk and Bilayer Hexagonal Boron Nitride*, Phys. Rev. Lett. 036104 (2013).

[49] R. T. Paine and C. K. Narula, *Synthetic routes to boron nitride*, Chem. Rev. **90**, 73–91 (1990).

[50] L. H. Li, J. Cervenka, K. Watanabe, T. Taniguchi, and Y. Chen, *Strong Oxidation Resistance of Atomically Thin Boron Nitride Nanosheets*, ACS Nano **8**, 1457–1462 (2014).

[51] Z. Liu, Y. Gong, W. Zhou, L. Ma, J. Yu, J. C. Idrobo, J. Jung, A. H. MacDonald, R. Vajtai, J. Lou, and P. M. Ajayan, *Ultrathin high-temperature oxidation-resistant coatings of hexagonal boron nitride.*, Nat. Commun. **4**, 2541 (2013).

[52] I. Jo, M. T. Pettes, J. Kim, K. Watanabe, T. Taniguchi, Z. Yao, and L. Shi, *Thermal Conductivity and Phonon Transport in Suspended Few-Layer Hexagonal Boron Nitride*, Nano Lett. **13**, 550–554 (2013).

[53] G.-H. Lee, Y.-J. Yu, C. Lee, C. Dean, K. L. Shepard, P. Kim, and J. Hone, *Electron tunneling through atomically flat and ultrathin hexagonal boron nitride*, Appl. Phys. Lett. 243114 (2011).

[54] S. N. Mohammad, F. J. Kub, and C. R. Eddy, *Field-plate design for edge termination in silicon carbide high-power Schottky diodes*, J. Vac. Sci. Technol. B, Nanotechnol. Microelectron. Mater. Process. Meas. Phenom. **29**, 021021 (2011).

[55] L. Britnell, R. V. Gorbachev, R. Jalil, B. D. Belle, F. Schedin, A. Mishchenko, T. Georgiou, M. I. Katsnelson, L. Eaves, S. V. Morozov, N. M. R. Peres, J. Leist, A. K. Geim, K. S. Novoselov, and L. A. Ponomarenko, *Field-Effect Tunneling Transistor Based on Vertical Graphene Heterostructures*, Science **335**, 947–950 (2012).

[56] K. Watanabe, T. Taniguchi, and H. Kanda, *Direct-bandgap properties and evidence for ultraviolet lasing of hexagonal boron nitride single crystal*, Nat. Mater. **3**, 404–9 (2004).

[57] C. R. Dean, A. F. Young, I. Meric, C. Lee, L. Wang, S. Sorgenfrei, K. Watanabe, T. Taniguchi, P. Kim, K. L. Shepard, and J. Hone, *Boron nitride substrates for high-quality graphene electronics*, Nat. Nanotechnol. **5**, 722–726 (2010).

[58] L. F. Dobrzhinetskaya, R. Wirth, J. Yang, H. W. Green, I. D. Hutcheon, P. K. Weber, and E. S. Grew, *Qingsongite, natural cubic boron nitride: The first boron mineral from the Earth's mantle*, Am. Mineral. **99**, 764–772 (2014).

[59] W. H. Balmain, *Bemerkungen über die Bildung von Verbindungen des Bors und Siliciums mit Stickstoff und gewissen Metallen*, J. für Prakt. Chemie **27**, 422–430 (1842).

[60] A. Lipp, K. Schwetz, and K. Hunold, *Hexagonal boron nitride: Fabrication, properties and applications*, J. Eur. Ceram. Soc. **5**, 3–9 (1989).

[61] T. Taniguchi and K. Watanabe, *Synthesis of high-purity boron nitride single crystals under high pressure by using Ba–BN solvent*, J. Cryst. Growth **303**, 525–529 (2007).

[62] *Two-dimensional atomic crystals*, Proc. Natl. Acad. Sci. **102**, 10451–10453 (2005).

[63] M. T. Paffett, R. J. Simonson, P. Papin, and R. T. Paine, *Borazine adsorption and decomposition at Pt(111) and Ru(001) surfaces*, Surf. Sci. 286–296 (1990).

[64] A. Nagashima, N. Tejima, Y. Gamou, T. Kawai, and C. Oshima, *Electronic dispersion relations of monolayer hexagonal boron nitride formed on the Ni(111) surface*, Phys. Rev. B **51**, 4606–4613 (1995).

[65] K. K. Kim, A. Hsu, X. Jia, S. M. Kim, Y. Shi, M. Hofmann, D. Nezich, J. F. Rodriguez-Nieva, M. Dresselhaus, T. Palacios, and J. Kong, *Synthesis of Monolayer Hexagonal Boron Nitride on Cu Foil Using Chemical Vapor Deposition*, Nano Lett. **12**, 161–166 (2012).

[66] L. Song, L. Ci, H. Lu, P. B. Sorokin, C. Jin, J. Ni, A. G. Kvashnin, D. G. Kvashnin, J. Lou, B. I. Yakobson, and P. M. Ajayan, *Large scale growth and characterization of atomic hexagonal boron nitride layers*, Nano Lett. 3209–3215 (2010).

[67] W. Auwärter, H. U. Suter, H. Sachdev, and T. Greber, *Synthesis of One Monolayer of Hexagonal Boron Nitride on Ni(111) from B-Trichloroborazine (ClBNH) 3*, Chem. Mater. **16**, 343–345 (2004).

[68] A. Ismach, H. Chou, D. A. Ferrer, Y. Wu, S. McDonnell, H. C. Floresca, A. Covacevich, C. Pope, R. Piner, M. J. Kim, R. M. Wallace, L. Colombo, and R. S. Ruoff, *Toward the Controlled Synthesis of Hexagonal Boron Nitride Films*, ACS Nano **6**, 6378–6385 (2012).

[69] W. Auwärter, M. Muntwiler, J. Osterwalder, and T. Greber, *Defect lines and two-domain structure of hexagonal boron nitride films on Ni(111)*, Surf. Sci. **545**, L735–L740 (2003).

[70] J.-H. Park, J. C. Park, S. J. Yun, H. Kim, D. H. Luong, S. M. Kim, S. H. Choi, W. Yang, J. Kong, K. K. Kim, and Y. H. Lee, *Large-area monolayer hexagonal boron nitride on Pt foil*, ACS Nano **8**, 8520–8 (2014).

[71] P. Sutter, J. Lahiri, P. Albrecht, and E. Sutter, *Chemical Vapor Deposition and Etching of High-Quality Monolayer Hexagonal Boron Nitride Films*, ACS Nano **5**, 7303–7309 (2011).

[72] S. Caneva, R. S. Weatherup, B. C. Bayer, R. Blume, A. Cabrero-Vilatela, P. Braeuninger-Weimer, M.-B. Martin, R. Wang, C. Baehtz, R. Schloegl, J. C. Meyer, and S. Hofmann, *Controlling Catalyst Bulk Reservoir Effects for Monolayer Hexagonal Boron Nitride CVD*, Nano Lett. **16**, 1250–1261 (2016).

[73] N. R. Glavin, M. L. Jespersen, M. H. Check, J. Hu, A. M. Hilton, T. S. Fisher, and A. A. Voevodin, *Synthesis of few-layer, large area hexagonal-boron nitride by pulsed laser deposition*, Thin Solid Films 245–250 (2014).

[74] H. Wang, X. Zhang, J. Meng, Z. Yin, X. Liu, Y. Zhao, and L. Zhang, *Controlled Growth of Few-Layer Hexagonal Boron Nitride on Copper Foils Using Ion Beam Sputtering Deposition*, Small **11**, 1542–1547 (2015).

[75] P. Sutter, J. Lahiri, P. Zahl, B. Wang, and E. Sutter, *Scalable synthesis of uniform few-layer hexagonal boron nitride dielectric films*, Nano Lett. 276–281 (2013).

[76] S. Suzuki, R. M. Pallares, and H. Hibino, *Growth of atomically thin hexagonal boron nitride films by diffusion through a metal film and precipitation*, J. Phys. D. Appl. Phys. 385304 (2012).

[77] M. J. Paisley, Z. Sitar, B. Yan, and R. F. Davis, *Growth of boron nitride films by gas molecular-beam epitaxy*, J. Vac. Sci. Technol. B Microelectron. Nanom. Struct. 323 (1990).

[78] C. L. Tsai, Y. Kobayashi, T. Akasaka, and M. Kasu, *Molecular beam epitaxial growth of hexagonal boron nitride on Ni(111) substrate*, J. Cryst. Growth 3054–3057 (2009).

[79] A. K. Geim and I. V. Grigorieva, *Van der Waals heterostructures*, Nature 419–425 (2013).

[80] A. C. Ferrari, F. Bonaccorso, V. Fal'ko, K. S. Novoselov, S. Roche, P. Bøggild, S. Borini, F. H. L. Koppens, V. Palermo, N. Pugno, J. a. Garrido, R. Sordan, A. Bianco, L. Ballerini, M. Prato, E. Lidorikis, J. Kivioja, C. Marinelli, T. Ryhänen, A. Morpurgo, J. N. Coleman, V. Nicolosi, L. Colombo, A. Fert, M. Garcia-Hernandez, A. Bachtold, G. F. Schneider, F. Guinea, C. Dekker, M. Barbone, Z. Sun, C. Galiotis, A. N. Grigorenko, G. Konstantatos, A. Kis, M. Katsnelson, L. Vandersypen, A. Loiseau, V. Morandi, D. Neumaier, E. Treossi, V. Pellegrini, M. Polini, A. Tredicucci, G. M. Williams, B. Hee Hong, J.-H. Ahn, J. Min Kim, H. Zirath, B. J. van Wees, H. van der Zant, L. Occhipinti, A. Di Matteo, I. a. Kinloch, T. Seyller, E. Quesnel, X. Feng, K. Teo, N. Rupesinghe, P. Hakonen, S. R. T. Neil, Q. Tannock, T. Löfwander, and J. Kinaret, *Science and technology roadmap for graphene, related two-dimensional crystals, and hybrid systems*, Nanoscale 4598–4810 (2015).

[81] J. Xue, J. Sanchez-Yamagishi, D. Bulmash, P. Jacquod, A. Deshpande, K. Watanabe, T. Taniguchi, P. Jarillo-Herrero, and B. J. LeRoy, *Scanning tunnelling microscopy and spectroscopy of ultra-flat graphene on hexagonal boron nitride*, Nat. Mater. 282–285 (2011).

[82] W. Gannett, W. Regan, K. Watanabe, T. Taniguchi, M. F. Crommie, and A. Zettl, *Boron nitride substrates for high mobility chemical vapor deposited graphene*, Appl. Phys. Lett. 242105 (2011).

[83] L. Britnell, R. V. Gorbachev, R. Jalil, B. D. Belle, F. Schedin, M. I. Katsnelson, L. Eaves, S. V. Morozov, A. S. Mayorov, N. M. R. Peres, A. H. Castro Neto, J. Leist, A. K. Geim, L. A. Ponomarenko, and K. S. Novoselov, *Electron Tunneling through Ultrathin Boron Nitride Crystalline Barriers*, Nano Lett. 1707–1710 (2012).

[84] S. Hwan Lee, M. Sup Choi, J. Lee, C. Ho Ra, X. Liu, E. Hwang, J. Hee Choi, J. Zhong, W. Chen, and W. Jong Yoo, *High performance vertical tunneling diodes using graphene/hexagonal boron nitride/graphene hetero-structure*, Appl. Phys. Lett. 053103 (2014).

[85] H. Wang, T. Taychatanapat, A. Hsu, K. Watanabe, T. Taniguchi, P. Jarillo-Herrero, and T. Palacios, *BN/Graphene/BN Transistors for RF Applications*, IEEE Electron Device Lett. 1209–1211 (2011).

[86] Z. Zuo, Z. Xu, R. Zheng, A. Khanaki, J.-G. Zheng, and J. Liu, *In-situ epitaxial growth of graphene/h-BN van der Waals heterostructures by molecular beam epitaxy*, Sci. Rep. 14760 (2015).

[87] Z. Xu, A. Khanaki, H. Tian, R. Zheng, M. Suja, J.-G. Zheng, and J. Liu, *Direct growth of hexagonal boron nitride/graphene heterostructures on cobalt foil substrates by plasma-assisted molecular beam epitaxy*, Appl. Phys. Lett. 043110 (2016).

[88] R. Zheng, A. Khanaki, H. Tian, Y. He, Y. Cui, Z. Xu, and J. Liu, *Precipitation growth of graphene under exfoliated hexagonal boron nitride to form heterostructures on cobalt substrate by molecular beam epitaxy*, Appl. Phys. Lett. 011903 (2017).

[89] Z. Liu, L. Song, S. Zhao, J. Huang, L. Ma, J. Zhang, J. Lou, and P. M. Ajayan, *Direct growth of graphene/hexagonal boron nitride stacked layers*, Nano Letters **11**, 2032–2037 (2011).

[90] C. Zhang, S. Zhao, C. Jin, A. L. Koh, Y. Zhou, W. Xu, Q. Li, Q. Xiong, H. Peng, and Z. Liu, *Direct growth of large-area graphene and boron nitride heterostructures by a co-segregation method*, Nat. Commun. 6519 (2015).

[91] S. Roth, F. Matsui, T. Greber, and J. Osterwalder, *Chemical Vapor Deposition and Characterization of Aligned and Incommensurate Graphene/Hexagonal Boron Nitride Heterostack on Cu(111)*, Nano Lett. 2668–2675 (2013).

[92] W. Yang, G. Chen, Z. Shi, C.-C. Liu, L. Zhang, G. Xie, M. Cheng, D. Wang, R. Yang, D. Shi, K. Watanabe, T. Taniguchi, Y. Yao, Y. Zhang, and G. Zhang, *Epitaxial growth of single-domain graphene on hexagonal boron nitride*, Nat. Mater. 792–797 (2013).

[93] D. Usachov, V. K. Adamchuk, D. Haberer, A. Grüneis, H. Sachdev, A. B. Preobrajenski, C. Laubschat, and D. V. Vyalikh, *Quasifreestanding single-layer hexagonal boron nitride as a substrate for graphene synthesis*, Phys. Rev. B 075415 (2010).

[94] Y.-C. Lin, N. Lu, N. Perea-Lopez, J. Li, Z. Lin, X. Peng, C. H. Lee, C. Sun, L. Calderin, P. N. Browning, M. S. Bresnehan, M. J. Kim, T. S. Mayer, M. Terrones, and J. A. Robinson, *Direct Synthesis of van der Waals Solids*, ACS Nano 3715–3723 (2014).

[95] D. P. Gopalan, P. C. Mende, S. C. de la Barrera, S. Dhingra, J. Li, K. Zhang, N. A. Simonson, J. A. Robinson, N. Lu, Q. Wang, M. J. Kim, B. D'Urso, and R. M. Feenstra, *Formation of hexagonal boron nitride on graphene-covered copper surfaces*, J. Mater. Res. 945–958 (2016).

[96] M. A. Herman and H. Sitter, *Molecular beam epitaxy: fundamentals and current status*, Vol. 7, Springer Science & Business Media (2012), ISBN 9783642800627.

[97] W. S. Knodle and R. Chow, *Molecular beam epitaxy: Equipment and practice. Handbook of Thin Film Deposition Processes and Techniques*, Elsevier (2012), ISBN 9780815517788.

[98] W. H. Weber and R. Merlin, *Raman Scattering in Materials Science*, Vol. 42, Springer Science & Business Media (2013), ISBN 9783662042212.

[99] A. C. Ferrari and D. M. Basko, *Raman spectroscopy as a versatile tool for studying the properties of graphene*, Nat. Nanotechnol. **8**, 235–246 (2013).

[100] C. Casiraghi, S. Pisana, K. S. Novoselov, A. K. Geim, and A. C. Ferrari, *Raman fingerprint of charged impurities in graphene*, Appl. Phys. Lett. 233108 (2007).

[101] L. G. Cançado, A. Jorio, E. H. M. Ferreira, F. Stavale, C. A. Achete, R. B. Capaz, M. V. O. Moutinho, A. Lombardo, T. S. Kulmala, and A. C. Ferrari, *Quantifying Defects in Graphene via Raman Spectroscopy at Different Excitation Energies*, Nano Letters **11**, 3190–3196 (2011).

[102] A. Eckmann, A. Felten, A. Mishchenko, L. Britnell, R. Krupke, K. S. Novoselov, and C. Casiraghi, *Probing the Nature of Defects in Graphene by Raman Spectroscopy*, Nano Lett. 3925–3930 (2012).

[103] A. Eckmann, A. Felten, I. Verzhbitskiy, R. Davey, and C. Casiraghi, *Raman study on defective graphene: Effect of the excitation energy, type, and amount of defects*, Phys. Rev. B 035426 (2013).

[104] T. M. G. Mohiuddin, A. Lombardo, R. R. Nair, A. Bonetti, G. Savini, R. Jalil, N. Bonini, D. M. Basko, C. Galiotis, N. Marzari, K. S. Novoselov, A. K. Geim, and A. C. Ferrari, *Uniaxial strain in graphene by Raman spectroscopy: G peak splitting, Grüneisen parameters, and sample orientation*, Phys. Rev. B 205433 (2009).

[105] C. Thomsen and S. Reich, *Double Resonant Raman Scattering in Graphite*, Phys. Rev. Lett. 5214–5217 (2000).

[106] I. Pócsik, M. Hundhausen, M. Koós, and L. Ley, *Origin of the D peak in the Raman spectrum of microcrystalline graphite*, Journal of Non-Crystalline Solids **227**, 1083 – 1086 (1998).

[107] L. M. Malard, M. A. Pimenta, G. Dresselhaus, and M. S. Dresselhaus, *Raman spectroscopy in graphene*, Phys. Rep. 51–87 (2009).

[108] W. C. Kuo, M. Briceno, and D. Ozkaya, *Final analysis: Characterisation of catalysts using secondary and backscattered electron in-lens detectors*, Platinum Metals Review **58**, 106–110 (2014).

[109] Y. Homma, S. Suzuki, Y. Kobayashi, M. Nagase, and D. Takagi, *Mechanism of bright selective imaging of single-walled carbon nanotubes on insulators by scanning electron microscopy*, Appl. Phys. Lett. **84**, 1750–1752 (2004).

[110] J. Thornton, *Scanning Probe Microscopy Training Notebook, 004-130-100 (cleanroom issue)*, Digital Instruments – Veeco Metrology Group.

[111] P. Eaton and P. West, *Atomic Force Microscopy*, Oxford University Press (2010), ISBN 9780199570454.

[112] K. Babcock and C. B. Prater, *Phase Imaging, Beyond Topography*, Veeco Instruments Inc.

[113] T. C. Huang and P. K. Predecki, Grazing-incidence x-ray technique for surface, interface and thin-film analysis, In *Denver X-ray conference on Applications of X-ray Analysis*, number C, 1–12 (1997).

[114] H. Kiessig, *Interferenz von Röntgenstrahlen an dünnen Schichten*, Ann. Phys. **402**, 769–788 (1931).

[115] J. Daillant and A. Gibaud, *X-ray and Neutron Reflectivity: Principles and Applications*, Lecture Notes in Physics. Springer Berlin Heidelberg (2008), ISBN 9783540885887.

[116] K. Stoev and K. Sakurai, *Recent theoretical models in grazing incidence X-ray reflectometry*, Rigaku J 22–37 (1997).

[117] C. R. Brundle and A. D. Baker, *Electron Spectroscopy: Theory, Techniques and Applications*, Vol. 2, Academic Press (1977).

[118] S. Hüfner, *Photoelectron Spectroscopy: Principles and Applications*, Springer (1995), ISBN 9783662092804.

[119] S. Nakhaie, J. M. Wofford, T. Schumann, U. Jahn, M. Ramsteiner, M. Hanke, J. M. J. Lopes, and H. Riechert, *Synthesis of atomically thin hexagonal boron nitride films on nickel foils by molecular beam epitaxy*, Appl. Phys. Lett. **106**, 213108 (2015).

[120] A. Nagashima, N. Tejima, Y. Gamou, T. Kawai, and C. Oshima, *Electronic structure of monolayer hexagonal boron nitride physisorbed on metal surfaces*, Phys. Rev. Lett. 3918–3921 (1995).

[121] Q. Yu, J. Lian, S. Siriponglert, H. Li, Y. P. Chen, and S.-S. Pei, *Graphene segregated on Ni surfaces and transferred to insulators*, Appl. Phys. Lett. **93**, 113103 (2008).

[122] Y. Yang, Q. Fu, W. Wei, and X. Bao, *Segregation growth of epitaxial graphene overlayers on Ni(111)*, Sci. Bull. **61**, 1536–1542 (2016).

[123] J. Hoard, D. B. Sullenger, C. H. L. Kennard, and R. E. Hughes, *The structure analysis of β-rhombohedral boron*, J. Solid State Chem. **1**, 268–277 (1970).

[124] S. Reich, A. C. Ferrari, R. Arenal, A. Loiseau, I. Bello, and J. Robertson, *Resonant Raman scattering in cubic and hexagonal boron nitride*, Phys. Rev. B **71**, 205201 (2005).

[125] T. G. Kollie, *Measurement of the thermal-expansion coeficient of nickel from 300 to 1000 K and determination of the power-law constants near the Curie temperatures*, Phys. Rev. B **16**, 4872–4882 (1977).

[126] H. Cho, S. Park, D.-I. Won, S. O. Kang, S.-S. Pyo, D.-I. Kim, S. M. Kim, H. C. Kim, and M. J. Kim, *Growth kinetics of white graphene (h-BN) on a planarised Ni foil surface*, Sci. Rep. **5**, 11985 (2015).

[127] R. V. Gorbachev, I. Riaz, R. R. Nair, R. Jalil, L. Britnell, B. D. Belle, E. W. Hill, K. S. Novoselov, K. Watanabe, T. Taniguchi, A. K. Geim, and P. Blake, *Hunting for Monolayer Boron Nitride: Optical and Raman Signatures*, Small **7**, 465–468 (2011).

[128] Q. Cai, D. Scullion, A. Falin, K. Watanabe, T. Taniguchi, Y. Chen, E. J. G. Santos, and L. H. Li, *Raman signature and phonon dispersion of atomically thin boron nitride*, Nanoscale **9**, 3059–3067 (2017).

[129] J. M. Wofford, S. Nie, K. F. McCarty, N. C. Bartelt, and O. D. Dubon, *Graphene Islands on Cu foils: the interplay between shape, orientation, and defects.*, Nano Lett. **10**, 4890–6 (2010).

[130] Y.-H. Lee, K.-K. Liu, A.-Y. Lu, C.-Y. Wu, C.-T. Lin, W. Zhang, C.-Y. Su, C.-L. Hsu, T.-W. Lin, K.-H. Wei, Y. Shi, and L.-J. Li, *Growth selectivity of hexagonal-boron nitride layers on Ni with various crystal orientations*, RSC Adv. **2**, 111 (2012).

[131] Y. Liu, S. Bhowmick, and B. I. Yakobson, *BN white graphene with "colorful" edges: the energies and morphology.*, Nano Lett. **11**, 3113–6 (2011).

[132] P. Sutter and E. Sutter, *Thickness determination of few-layer hexagonal boron nitride films by scanning electron microscopy and Auger electron spectroscopy*, APL Mater. **2**, 092502 (2014).

[133] T. Iwasaki, H. J. Park, M. Konuma, D. S. Lee, J. H. Smet, and U. Starke, *Long-range ordered single-crystal graphene on high-quality heteroepitaxial Ni thin films grown on MgO(111)*, Nano Lett. **11**, 79–84 (2011).

[134] H. Tanaka and M. Taniguchi, *Atomically flat nickel film grown on synthetic mica*, Jpn. J. Appl. Phys. **55**, 078003 (2016).

[135] T. Schumann, M. Dubslaff, M. H. Oliveira, M. Hanke, J. M. J. Lopes, and H. Riechert, *Effect of buffer layer coupling on the lattice parameter of epitaxial graphene on SiC(0001)*, Phys. Rev. B **90**, 041403 (2014).

[136] A. B. Preobrajenski, A. S. Vinogradov, and N. Mårtensson, *Ni 3d–BN π at the h-BN/Ni(111) interface observed with core-level spectroscopies*, Phys. Rev. B **70**, 165404 (2004).

[137] A. A. Tonkikh, E. N. Voloshina, P. Werner, H. Blumtritt, B. Senkovskiy, G. Güntherodt, S. S. P. Parkin, and Y. S. Dedkov, *Structural and electronic properties of epitaxial multilayer h-BN on Ni(111) for spintronics applications*, Sci. Rep. **6**, 23547 (2016).

[138] A. M. Shikin, G. V. Prudnikova, V. K. Adamchuk, F. Moresco, and K.-H. Rieder, *Surface intercalation of gold underneath a graphite monolayer on Ni(111) studied by angle-resolved photoemission and high-resolution electron-energy-loss spectroscopy*, Phys. Rev. B **62**, 13202–13208 (2000).

[139] E. Rokuta, Y. Hasegawa, K. Suzuki, Y. Gamou, C. Oshima, and A. Nagashima, *Phonon Dispersion of an Epitaxial Monolayer Film of Hexagonal Boron Nitride on Ni(111)*, Phys. Rev. Lett. **79**, 4609–4612 (1997).

[140] A. B. Preobrajenski, S. A. Krasnikov, A. S. Vinogradov, M. L. Ng, T. Käämbre, A. A. Cafolla, and N. Mårtensson, *Adsorption-induced gap states of h-BN on metal surfaces metal surfaces*, Phys. Rev. B 085421 (2008).

[141] M. S. Bresnehan, G. R. Bhimanapati, K. Wang, D. W. Snyder, and J. A. Robinson, *Impact of Copper Overpressure on the Synthesis of Hexagonal Boron Nitride Atomic Layers*, ACS Appl. Mater. Interfaces **6**, 16755–16762 (2014).

[142] H. Wang, X. Zhang, H. Liu, Z. Yin, J. Meng, J. Xia, X.-M. Meng, J. Wu, and J. You, *Synthesis of Large-Sized Single-Crystal Hexagonal Boron Nitride Domains on Nickel Foils by Ion Beam Sputtering Deposition*, Adv. Mater. **27**, 8109–8115 (2015).

[143] L. Schué, I. Stenger, F. Fossard, A. Loiseau, and J. Barjon, *Characterization methods dedicated to nanometer-thick hBN layers*, 2D Mater. **4**, 015028 (2016).

[144] *The Raman spectrum of gaseous oxygen*, J. Mol. Spectrosc. **4**, 195–200 (1960).

[145] K. K. Chow, M. Short, S. Lam, A. McWilliams, and H. Zeng, *A Raman cell based on hollow core photonic crystal fiber for human breath analysis*, Medical Physics **41**, 092701 (2014), 092701.

[146] V. Kochat, A. Nath Pal, E. S. Sneha, A. Sampathkumar, A. Gairola, S. A. Shivashankar, S. Raghavan, and A. Ghosh, *High contrast imaging and thickness determination of graphene with in-column secondary electron microscopy*, J. Appl. Phys. **110**, 014315 (2011).

[147] B. Sharma, T. Schumann, M. H. de Oliveira, and J. M. J. Lopes, *Controlled synthesis and characterization of multilayer graphene films on the C-face of silicon carbide*, Phys. status solidi **214**, 1600721 (2017).

[148] M. L. Bolen, S. E. Harrison, L. B. Biedermann, and M. A. Capano, *Graphene formation mechanisms on 4 H-SiC (0001)*, Phys. Rev. B **80**, 115433 (2009).

[149] M. H. Oliveira, Jr., J. M. J. Lopes, T. Schumann, L. A. Galves, M. Ramsteiner, K. Berlin, A. Trampert, and H. Riechert, *Synthesis of quasi-free-standing bilayer graphene nanoribbons on SiC surfaces*, Nat. Commun. **6**, 7632 (2015).

[150] A. S. Plaut, U. Wurstbauer, S. Wang, A. L. Levy, L. Fernandes dos Santos, L. Wang, L. N. Pfeiffer, K. Watanabe, T. Taniguchi, C. R. Dean, J. Hone, A. Pinczuk, and J. M. Garcia, *Exceptionally large migration length of carbon and topographically-facilitated self-limiting molecular beam epitaxial growth of graphene on hexagonal boron nitride*, Carbon **114**, 579–584 (2017).

[151] R. Y. Tay, M. H. Griep, G. Mallick, S. H. Tsang, R. S. Singh, T. Tumlin, E. H. T. Teo, and S. P. Karna, *Growth of Large Single-Crystalline Two-Dimensional Boron Nitride Hexagons on Electropolished Copper*, Nano Lett. **14**, 839–846 (2014).

[152] Z. Xu, H. Tian, A. Khanaki, R. Zheng, M. Suja, and J. Liu, *Large-area growth of multilayer hexagonal boron nitride on polished cobalt foils by plasma-assisted molecular beam epitaxy*, Sci. Rep. **7**, 43100 (2017).

[153] J. Dabrowski, G. Lippert, T. Schroeder, and G. Lupina, *Role of defects in the process of graphene growth on hexagonal boron nitride from atomic carbon*, Appl. Phys. Lett. **105**, 191610 (2014).

[154] F. Maeda and H. Hibino, *Thin Graphitic Structure Formation on Various Substrates by Gas-Source Molecular Beam Epitaxy Using Cracked Ethanol*, Jpn. J. Appl. Phys. **49**, 04DH13 (2010).

[155] Z. Xu, R. Zheng, A. Khanaki, Z. Zuo, and J. Liu, *Direct growth of graphene on in situ epitaxial hexagonal boron nitride flakes by plasma-assisted molecular beam epitaxy*, Appl. Phys. Lett. **107**, 213103 (2015).

[156] F. Müller, K. Stöwe, and H. Sachdev, *Symmetry versus Commensurability: Epitaxial Growth of Hexagonal Boron Nitride on Pt(111) From B-Trichloroborazine (ClBNH) 3*, Chem. Mater. **17**, 3464–3467 (2005).

[157] P. W. Sutter, J.-I. Flege, and E. Sutter, *Epitaxial graphene on ruthenium*, Nat. Mater. **7**, 406–411 (2008).

[158] S. Chen, H. Ji, H. Chou, Q. Li, H. Li, J. W. Suk, R. Piner, L. Liao, W. Cai, and R. S. Ruoff, *Millimeter-Size Single-Crystal Graphene by Suppressing Evaporative Loss of Cu During Low Pressure Chemical Vapor Deposition*, Adv. Mater. **25**, 2062–2065 (2013).

[159] R. Y. Tay, S. H. Tsang, M. Loeblein, W. L. Chow, G. C. Loh, J. W. Toh, S. L. Ang, and E. H. T. Teo, *Direct growth of nanocrystalline hexagonal boron nitride films on dielectric substrates*, Appl. Phys. Lett. **106**, 101901 (2015).

[160] M. Eizenberg and J. M. Blakely, *Carbon interaction with nickel surfaces: Monolayer formation and structural stability*, J. Chem. Phys. **71**, 3467 (1979).

[161] P. May, M. Lazzeri, P. Venezuela, F. Herziger, G. Callsen, J. S. Reparaz, A. Hoffmann, F. Mauri, and J. Maultzsch, *Signature of the two-dimensional phonon dispersion in graphene probed by double-resonant Raman scattering*, Phys. Rev. B **87**, 075402 (2013).

[162] H.-L. Liu, S. Siregar, E. H. Hasdeo, Y. Kumamoto, C.-C. Shen, C.-C. Cheng, L.-J. Li, R. Saito, and S. Kawata, *Deep-ultraviolet Raman scattering studies of monolayer graphene thin films*, Carbon **81**, 807–813 (2015).

[163] I. Calizo, I. Bejenari, M. Rahman, G. Liu, and A. A. Balandin, *Ultraviolet Raman microscopy of single and multilayer graphene*, Journal of Applied Physics **106**, 043509 (2009).

[164] C. Tyborski, F. Herziger, R. Gillen, and J. Maultzsch, *Beyond double-resonant Raman scattering: Ultraviolet Raman spectroscopy on graphene, graphite, and carbon nanotubes*, Phys. Rev. B **92**, 041401 (2015).

[165] K. Kisoda, S. Kamoi, N. Hasuike, H. Harima, K. Morita, S. Tanaka, and A. Hashimoto, *Few-layer epitaxial graphene grown on vicinal 6H–SiC studied by deep ultraviolet Raman spectroscopy*, Appl. Phys. Lett. **97**, 033108 (2010).

[166] J. W. Suk, A. Kitt, C. W. Magnuson, Y. Hao, S. Ahmed, J. An, A. K. Swan, B. B. Goldberg, and R. S. Ruoff, *Transfer of CVD-grown monolayer graphene onto arbitrary substrates*, ACS Nano **5**, 6916–6924 (2011).

[167] J. M. Garcia, U. Wurstbauer, A. Levy, L. N. Pfeiffer, A. Pinczuk, A. S. Plaut, L. Wang, C. R. Dean, R. Buizza, A. M. Van Der Zande, J. Hone, K. Watanabe, and T. Taniguchi, *Graphene growth on h-BN by molecular beam epitaxy*, Solid State Commun. **152**, 975–978 (2012).

[168] Z. Zafar, Z. H. Ni, X. Wu, Z. X. Shi, H. Y. Nan, J. Bai, and L. T. Sun, *Evolution of Raman spectra in nitrogen doped graphene*, Carbon **61**, 57–62 (2013).

[169] A. C. Ferrari, J. C. Meyer, V. Scardaci, C. Casiraghi, M. Lazzeri, F. Mauri, S. Piscanec, D. Jiang, K. S. Novoselov, S. Roth, and A. K. Geim, *Raman Spectrum of Graphene and Graphene Layers*, Phys. Rev. Lett. **97**, 187401 (2006).

[170] L. S. Panchakarla, K. S. Subrahmanyam, S. K. Saha, A. Govindaraj, H. R. Krishnamurthy, U. V. Waghmare, and C. N. R. Rao, *Synthesis, Structure, and Properties of Boron- and Nitrogen-Doped Graphene*, Adv. Mater. **21**, 4726–4730 (2009).

[171] L. Zhao, R. He, K. T. Rim, T. Schiros, K. S. Kim, H. Zhou, C. Gutiérrez, S. P. Chockalingam, C. J. Arguello, L. Pálová, D. Nordlund, M. S. Hybertsen, D. R. Reichman, T. F. Heinz, P. Kim, A. Pinczuk, G. W. Flynn, and A. N. Pasupathy, *Visualizing individual nitrogen dopants in monolayer graphene*, Science **333**, 999–1003 (2011).

[172] M. Bruna and S. Borini, *Observation of Raman G-band splitting in top-doped few-layer graphene*, Phys. Rev. B **81**, 125421 (2010).

[173] J. Yan, T. Villarson, E. a. Henriksen, P. Kim, and A. Pinczuk, *Optical phonon mixing in bilayer graphene with a broken inversion symmetry*, Phys. Rev. B **80**, 241417 (2009).

[174] Y. Gong, G. Shi, Z. Zhang, W. Zhou, J. Jung, W. Gao, L. Ma, Y. Yang, S. Yang, G. You, R. Vajtai, Q. Xu, A. H. MacDonald, B. I. Yakobson, J. Lou, Z. Liu, and P. M. Ajayan, *Direct chemical conversion of graphene to boron- and nitrogen- and carbon-containing atomic layers*, Nat. Commun. **5**, 3193 (2014).

[175] L. Ci, L. Song, C. Jin, D. Jariwala, D. Wu, Y. Li, A. Srivastava, Z. F. Wang, K. Storr, L. Balicas, F. Liu, and P. M. Ajayan, *Atomic layers of hybridized boron nitride and graphene domains*, Nat. Mater. **9**, 430–435 (2010).

[176] M. R. Uddin, J. Li, J. Y. Lin, and H. X. Jiang, *Carbon-rich hexagonal (BN)C alloys*, J. Appl. Phys. **117**, 215703 (2015).

[177] J. H. Meng, X. W. Zhang, H. Liu, Z. G. Yin, D. G. Wang, Y. Wang, J. B. You, and J. L. Wu, *Synthesis of atomic layers of hybridized h-BNC by depositing h-BN on graphene via ion beam sputtering*, Appl. Phys. Lett. **109**, 173106 (2016).

[178] Y. Yang, Q. Fu, H. Li, M. Wei, J. Xiao, W. Wei, and X. Bao, *Creating a Nanospace under an h-BN Cover for Adlayer Growth on Nickel(111)*, ACS Nano **9**, 11589–11598 (2015).

[179] A. B. Preobrajenski, M. A. Nesterov, M. L. Ng, A. S. Vinogradov, and N. Mårtensson, *Monolayer h-BN on lattice-mismatched metal surfaces: On the formation of the nanomesh*, Chem. Phys. Lett. **446**, 119–123 (2007).

[180] Y. Zhang, X. Weng, H. Li, H. Li, M. Wei, J. Xiao, Z. Liu, M. Chen, Q. Fu, and X. Bao, *Hexagonal Boron Nitride Cover on Pt(111): A New Route to Tune Molecule–Metal Interaction and Metal-Catalyzed Reactions*, Nano Lett. **15**, 3616–3623 (2015).

[181] Y. Yang, Q. Fu, M. Wei, H. Bluhm, and X. Bao, *Stability of BN/metal interfaces in gaseous atmosphere*, Nano Res. **8**, 227–237 (2015).

[182] F. Orlando, R. Larciprete, P. Lacovig, I. Boscarato, A. Baraldi, and S. Lizzit, *Epitaxial Growth of Hexagonal Boron Nitride on Ir(111)*, J. Phys. Chem. C **116**, 157–164 (2012).

[183] A. Ebnonnasir, S. Kodambaka, and C. V. Ciobanu, *Strongly and weakly interacting configurations of hexagonal boron nitride on nickel*, Surf. Rev. Lett. **22**, 1550078 (2015).

[184] A. B. Preobrajenski, A. S. Vinogradov, and N. Mårtensson, *Monolayer of h-BN chemisorbed on Cu(111) and Ni(111): The role of the transition metal 3d states*, Surf. Sci. **582**, 21–30 (2005).

[185] E. Rokuta, Y. Hasegawa, A. Itoh, K. Yamashita, T. Tanaka, S. Otani, and C. Oshima, *Vibrational spectra of the monolayer films of hexagonal boron nitride and graphite on faceted Ni(755)*, Surf. Sci. **427-428**, 97–101 (1999).

[186] R. J. Koch, M. Weser, W. Zhao, F. Viñes, K. Gotterbarm, S. M. Kozlov, O. Höfert, M. Ostler, C. Papp, J. Gebhardt, H.-P. Steinrück, A. Görling, and T. Seyller, *Growth and electronic structure of nitrogen-doped graphene on Ni(111)*, Phys. Rev. B **86**, 075401 (2012).

[187] J. Gebhardt, R. J. Koch, W. Zhao, O. Höfert, K. Gotterbarm, S. Mammadov, C. Papp, A. Görling, H.-P. Steinrück, and T. Seyller, *Growth and electronic structure of boron-doped graphene*, Phys. Rev. B **87**, 155437 (2013).

[188] D. R. Wheeler and W. A. Brainard, *Composition of rf-sputtered refractory compounds determined by x-ray photoelectron spectroscopy*, Journal of Vacuum Science and Technology **15**, 24–30 (1978).

[189] A. Nagashima, N. Tejima, and C. Oshima, *Electronic states of the pristine and alkali-metal-intercalated monolayer graphite/Ni(111) systems*, Phys. Rev. B **50**, 17487–17495 (1994).

[190] D. Wei, Y. Liu, Y. Wang, H. Zhang, L. Huang, and G. Yu, *Synthesis of n-doped graphene by chemical vapor deposition and its electrical properties*, Nano Letters **9**, 1752 – 1758 (2009).

[191] C. Zhang, L. Fu, N. Liu, M. Liu, Y. Wang, and Z. Liu, *Synthesis of nitrogen-doped graphene using embedded carbon and nitrogen sources*, Advanced Materials **23**, 1020–1024 (2011).

[192] Y.-C. Lin, C.-Y. Lin, and P.-W. Chiu, *Controllable graphene n-doping with ammonia plasma*, Applied Physics Letters **96**, 133110 (2010).

[193] C. Oshima, N. Tanaka, A. Itoh, E. Rokuta, K. Yamashita, and T. Sakurai, *A heteroepitaxial multi-atomic-layer system of graphene and h-BN*, Surf. Rev. Lett. **07**, 521–525 (2000).

[194] J. A. Venables, *Atomic processes in crystal growth*, Surface Science **299**, 798 – 817 (1994).

[195] Y. Miyamoto, A. Rubio, M. L. Cohen, and S. G. Louie, *Chiral tubules of hexagonal BC_2N*, Phys. Rev. B **50**, 4976–4979 (1994).

[196] A. Dahal, R. Addou, P. Sutter, and M. Batzill, *Graphene monolayer rotation on Ni(111) facilitates bilayer graphene growth*, Appl. Phys. Lett. **100**, 241602 (2012).

[197] T. S. Cheng, A. Davies, A. Summerfield, Y. Cho, I. Cebula, R. J. A. Hill, C. J. Mellor, A. N. Khlobystov, T. Taniguchi, K. Watanabe, P. H. Beton, C. T. Foxon, L. Eaves, and S. V. Novikov, *High temperature MBE of graphene on sapphire and hexagonal boron nitride flakes on sapphire*, J. Vac. Sci. Technol. B, Nanotechnol. Microelectron. Mater. Process. Meas. Phenom. **34**, 02L101 (2016).

[198] C.-Y. Kang, J. Tang, Z.-L. Liu, L.-M. Li, W.-S. Yan, S.-Q. Wei, and P.-S. Xu, *Growth of Few-Layer Graphene on Sapphire Substrates by Directly Depositing Carbon Atoms*, Chinese Phys. Lett. **28**, 118101 (2011).

[199] Z. Liu, J. Tang, C. Kang, C. Zou, W. Yan, and P. Xu, *Effect of substrate temperature on few-layer graphene grown on Al2O3 (0001) via direct carbon atoms deposition*, Solid State Commun. **152**, 960–963 (2012).

[200] S. Wang, L. Fernandes dos Santos, U. Wurstbauer, L. Wang, L. N. Pfeiffer, J. Hone, J. M. Garcia, and A. Pinczuk, *Single- and bi-layer graphene grown on sapphire by molecular beam epitaxy*, Solid State Commun. **189**, 15–20 (2014).

[201] J. M. Wofford, F. Speck, T. Seyller, J. M. J. Lopes, and H. Riechert, *Nickel enhanced graphene growth directly on dielectric substrates by molecular beam epitaxy*, J. Appl. Phys. **120**, 045309 (2016).

[202] G. Lippert, J. Dabrowski, M. Lemme, C. Marcus, O. Seifarth, and G. Lupina, *Direct graphene growth on insulator*, Phys. status solidi **248**, 2619–2622 (2011).

[203] G. Lippert, J. Dabrowski, Y. Yamamoto, F. Herziger, J. Maultzsch, M. C. Lemme, W. Mehr, and G. Lupina, *Molecular beam growth of micrometer-size graphene on mica*, Carbon **52**, 40–48 (2013).

[204] U. Wurstbauer, T. Schiros, C. Jaye, A. S. Plaut, R. He, A. Rigosi, C. Gutiérrez, D. Fischer, L. N. Pfeiffer, A. N. Pasupathy, A. Pinczuk, and J. M. Garcia, *Molecular beam growth of graphene nanocrystals on dielectric substrates*, Carbon **50**, 4822–4829 (2012).

[205] A. Summerfield, A. Davies, T. S. Cheng, V. V. Korolkov, Y. Cho, C. J. Mellor, C. T. Foxon, A. N. Khlobystov, K. Watanabe, T. Taniguchi, L. Eaves, S. V. Novikov, and P. H. Beton, *Strain-Engineered Graphene Grown on Hexagonal Boron Nitride by Molecular Beam Epitaxy*, Sci. Rep. **6**, 22440 (2016).

[206] M. Batzill, *Surface Science Reports The surface science of graphene : Metal interfaces , CVD synthesis , nanoribbons , chemical modifications , and defects*, Surf. Sci. Rep. **67**, 83–115 (2012).

[207] A. Nagashima, H. Itoh, T. Ichinokawa, C. Oshima, and S. Otani, *Change in the electronic states of graphite overlayers depending on thickness*, Phys. Rev. B **50**, 4756–4763 (1994).

[208] A. C. Ferrari and J. Robertson, *Interpretation of Raman spectra of disordered and amorphous carbon*, Phys. Rev. B **61**, 14095–14107 (2000).

[209] L. G. Cançado, K. Takai, T. Enoki, M. Endo, Y. A. Kim, H. Mizusaki, A. Jorio, L. N. Coelho, R. Magalhães-Paniago, and M. A. Pimenta, *General equation for the determination of the crystallite size la of nanographite by Raman spectroscopy*, Appl. Phys. Lett. 1998–2001 (2006).

[210] L. G. Cançado, A. Jorio, and M. A. Pimenta, *Measuring the absolute Raman cross section of nanographites as a function of laser energy and crystallite size*, Phys. Rev. B 064304 (2007).

[211] R. Tromp, G. W. Rubloff, P. Balk, F. K. LeGoues, and E. J. van Loenen, *High-Temperature $Si O_2$ Decomposition at the $Si O_2$/Si Interface*, Phys. Rev. Lett. 2332–2335 (1985).

[212] M. A. Fanton, J. A. Robinson, C. Puls, Y. Liu, M. J. Hollander, B. E. Weiland, M. Labella, K. Trumbull, R. Kasarda, C. Howsare, J. Stitt, and D. W. Snyder, *Characterization of Graphene Films and Transistors Grown on Sapphire by Metal-Free Chemical Vapor Deposition*, ACS Nano 8062–8069 (2011).

[213] I. Vlassiouk, M. Regmi, P. Fulvio, S. Dai, P. Datskos, G. Eres, and S. Smirnov, *Role of Hydrogen in Chemical Vapor Deposition Growth of Large Single-Crystal Graphene*, ACS Nano **5**, 6069–6076 (2011).

[214] M. Heilmann et al., private communication (2017).

List of Figures

Acknowledgements

I would like to express my gratitude to all the people who have supported me on a scientific, technical, personal or any other level to accomplish the present work. In particular, I wish to thank the following people.

First of all, I would like to thank Prof. Dr. Henning Riechert for giving me the opportunity to carry out this Ph.D. project at the Paul-Drude-Institut. I would like to extend my gratitude to the committee members, Prof. Dr. W. Ted Masselink and Prof. Dr. Sergei Novikov for refereeing my thesis.

I am deeply grateful to Dr. J. Marcelo J. Lopes for accepting me in his group, the tremendous support and invaluable guidance I received for my research, and for critical reading of the thesis draft. The inspiring and encouraging atmosphere he created in the group was essential for the achievements of this project.

My sincere thanks also go to my colleagues in the graphene group; Dr. Joseph M. Wofford and Dr. Timo Schumann for introducing me to the world of MBE growth, answering my countless questions, and for the work we did together; Dr. Martin Heilmann for our fruitful discussions and his support with the German translation of the thesis abstract; Ms. Lauren A. Galves for the constructive consultations and encouragement.

I wish to thank Dr. Lutz Geelhaar for welcoming me in the department of epitaxy and for the helpful advice and suggestions I received.

I would like to thank my colleagues at the institute; Dr. Manfred Ramsteiner for assisting with Raman experiments and insightful discussions; Dr. Uwe Jahn for his continuous support with SEM imaging; Dr. Michael Hanke and Mr. Thilo Krause for the GID and XRR measurements and patiently explaining me the results. My appreciation is also extended to Dr. Xianjie Liu, from Linköping University, for conducting XPS measurements.

I am very grateful to Mr. Hans-Peter Schönherr, Ms. Claudia Herrmann, and Mr. Michael Höricke for the technical support in the MBE and chemistry labs. I also want to thank Dr. Abbes Tahraoui, Mr. Bernd Drescher, and Mr. Sander Rauwerdink for providing the Ni/MgO substrates and the technical support for processing the samples.

I wish to thank Mr. Andreas Hartung who helped me deal with all the complicated bureaucracy.

I thank all my fellow students, colleagues and friends for all the scientific and non-scientific discussions, and for making this time memorable for me.

Last but not least, I am very thankful to my family for their love, patience and support.

Selbständigkeitserklärung

Ich erkläre, dass ich die vorliegende Arbeit selbständig und nur unter Verwendung der angegebenen Literatur und Hilfsmittel angefertigt habe.

Berlin, den 01.09.2017 Siamak Nakhaie